©Copyright 2025
Alyssa Poletti

Extreme Climates and How to Avoid Them

Alyssa Poletti

A dissertation submitted in partial fulfillment of the
requirements for the degree of

Doctor of Philosophy

University of Washington

2025

Reading Committee:

Dargan Frierson, Chair

Robert Wood

Abby Swann

Program Authorized to Offer Degree:
Atmospheric and Climate Science

University of Washington

Abstract

Extreme Climates and How to Avoid Them

Alyssa Poletti

Chair of the Supervisory Committee:
Professor Dargan Frierson
Department of Atmospheric and Climate Science

Climate change poses an existential threat. In this dissertation, I explore the uncertainties within, atmospheric changes due to, adaptations for, and mitigation pathways to avoid catastrophic warming. I begin with an analysis of extreme warming in Global Climate Model simulations into 2300, continue to an analysis of Washington State energy assistance policy in a warming world, and end with a coupled economic-climate model to bridge the topics of atmospheric science and climate policy. I find that prioritizing the reduction of fossil fuel emissions rather than scaling carbon capture technologies provides the best chance of avoiding local- to global-scale climatological changes. Ultimately, future research must prioritize equity in climate modeling to better guide us to a greener future.

TABLE OF CONTENTS

Page

List of Figures ii

List of Tables vii

Chapter 1: Introduction 1
1.1 Understanding Future Warming and Carbon Budgets 1
1.2 Uncertainties in Climate Feedbacks 2
1.3 Shared Socio-Economic Pathways 6
1.4 Negative Emission Technologies and Deemphasizing Economic Growth . . . 6

Chapter 2: Atmosphere and Ocean Energy Transport in Extreme Warming Scenarios 8
2.1 Introduction 8
2.2 Methods & Models 10
2.3 Results 12
2.4 Discussion & Conclusions 45

Chapter 3: Equitably Adapting to Extreme Heat in Washington State 48
3.1 Introduction 48
3.2 Identifying Underserved Communities of Color 54
3.3 Demographic Reporting Requirements for Consumer-Owned Utilities 55
3.4 Publicly Available LIHEAP Data through the WA Department of Commerce 60
3.5 Conclusions 64

Chapter 4: Evaluating Low Energy Demand Scenarios in FaIR 69
4.1 Introduction 69
4.2 Methods & Model 72
4.3 Results & Discussion 89
4.4 Conclusions 100

Chapter 5: Conclusions 104

LIST OF FIGURES

Figure Number Page

1.1 *From Poletti et al. (2024b).* (a) Surface temperature anomaly against time, (b) the net TOA radiative flux against surface temperature anomaly (see equation 1.2). (c) The AMOC strength anomaly against time. The abrupt-4xCO_2 data is normalized in (a-b) using the effective radiative forcing 5

2.1 SSP5-8.5ext Greenhouse Gas Concentrations and Forcings. (a) The effective radiative forcing of CO_2, CH_4, N_2O, aerosols, and total against time for SSP5-8.5ext simulations (solid) and the global CO_2 concentration (dashed) against time for SSP5-8.5ext simulations. (b) The global mean temperature anomaly for CanESM5, IPSL-CM6A-LR, and MRI-ESM2-0 (solid) against time for historical (1850-2015) and SSP5-8.5ext (2015-2300), and the global CO_2 concentration (dashed) against time for SSP5-8.5ext. 13

2.2 Maps of the Near Surface Air Temperature. (a, b, c) Near-surface temperature averaged over the hot period, (d, e, f) the hot period temperature anomalies relative to pre-Industrial, and (g, h, i) the percent change in surface temperature by the intermediate period, calculated as the ratio of the intermediate period temperature anomalies divided by the hot period temperature anomalies relative to pre-Industrial. 16

2.3 Maps of the Specific Humidity Anomaly (a, b, c) Anomalies of surface specific humidity relative to pre-Industrial, and (d, e, f) the percent change from the intermediate period to the hot period, calculated as the ratio of the surface specific humidity anomaly in the intermediate period and the anomaly in the hot period. 19

2.4 Maps of the Relative Humidity Anomaly. (a, b, c) Anomalies of surface relative humidity in the hot period relative pre-Industrial, (d, e, f) anomalies of surface specific humidity in the intermediate relative pre-Industrial, and (g, h, i) the relative humidity change from 2075-2100, calculated as the hot period relative humidity minus the intermediate period relative humidity. 20

2.5 Zonally Averaged Specific and Relative Humidity. (a) The specific humidity (labeled "huss") and (b) relative humidity (labeled "hurs") zonal means, for the hot period (solid) and pre-Industrial (dashed). 21

2.6 Maps of the total Precipitation Anomaly. (a, b, c) The net precipitation (precipitation minus evaporation) anomaly for the hot period from pre-Industrial, (d, e, f) the intermediate period from pre-Industrial, and (g, h, i) the hot period anomaly from intermediate period anomaly. These maps are centered at 180 degrees longitudinally so as to better see the ITCZ. 23

2.7 Streamfunction and the Zonal Wind Anomaly The color contours represent (a, b, c) the streamfunction anomaly (10^{10} kg/s) and (d, e, f) the zonal wind anomaly (m/s) of CanESM5, IPSL-CM6A-LR, and MRI-ESM2-0. The black contours represent the pre-Industrial. The pre-Industrial streamfunction ranges from -9 to 9x10^{10} kg/s with a contour interval of 3x10^{10} kg/s. The pre-Industrial zonal wind ranges from 0 to 30 m/s with a contour interval of 6 m/s. 26

2.8 Time Evolution of the 500hPa Streamfunction. The streamfunction (10^{10} kg/s) at 500hPa for CanESM5 (a, red), IPSL-CM6A (b, green) and MRI-ESM2-0 (c, blue). The solid lines represent the hot period, the dashed lines represent the intermediate period, and the dotted lines represent the pre-Industrial period. 27

2.9 Time Evolution of the Hadley-Ferrel boundaries and ITCZ locations. (a, b, c) The 30-year running mean NH and SH Hadley-Ferrel Boundary location and ITCZ location versus time, and (d, e, f) global mean temperature anomaly from 1850 to 2300. The time and zonally averaged pre-Industrial values are denoted by an X. In the time series figures (top row), the historical data (1850-2015) are denoted by the dashed lines, while the SSP-Ext runs (2015-2300) are denoted by the solid lines. In the temperature anomaly figures (bottom row), the time-mean historical data is denoted by a circle. 28

2.10 Time Evolution of the Polar-Ferrel boundaries and SH Stormtrack locations. The 30-year running mean of (a, d) the NH Polar-Ferrel Cell boundary, (b, e) the SH Polar-Ferrel Cell boundary (c, f) and the SH storm track location versus time (top row), and versus the global mean temperature anomaly (bottom row) from 1850 to 2300 . The time and zonally averaged pre-Industrial values are denoted by an X. In the time series figures (top row), the historical data (1850-2015) are denoted by the dashed lines, while the SSP-Ext runs (2015-2300) are denoted by the solid lines. In the temperature anomaly figures (bottom row), the time and time-mean historical data is denoted by a circle. The piControl stormtrack latitudes for CanESM5, IPSL-CM6A-LR, and MRI-ESM2-0 are 48.7S, 48.8S, and 47.9S respectively. 29

2.11 Northward Energy Transport. Northward transport of energy from (a) latent, (b) moist static energy, and (c) dry static energy and (d) the Atlantic Ocean. Pre-Industrial transports are dotted and hot period transports are solid. The CanESM5 ocean heat transport data for the hot period is averaged between 2156 and 2180, due to data availability, so it is denoted with a dashed line to indicate the different averaging period. 33

2.12 Northward Energy Transport Anomaly. The change in northward transport of energy (hot period minus pre-Industrial) from (a) latent (dashed) and DSE (solid), as well as from (b) ocean transport (dashed) and MSE (solid). 34

2.13 Maps of the Cloud Radiative Effect Anomaly The anomalies in (a, b, c) longwave cloud radiative effect, (d, e, f) shortwave cloud radiative effect as calculated using APRP, and (g, h, i) the sum of the longwave and shortwave cloud radiative effects. 40

2.14 Maps of Varibility in Sea Level Pressure. (a, b, c) The standard deviation of daily sea level pressure fields (hPa) in the hot period, and (d, e, f) the percentage change since pre-Industrial. 41

2.15 Maps of the Lapse Rate. The lapse rate in (a, b, c) the hot period, and (e, e, f) the change since pre-Industrial, calculated as the difference between the temperature at the surface and 300 hPa, divided by the difference in geopotential height at the same levels. 42

2.16 Maps of Moist Static Energy. The surface moist static energy (J/kg) in (a, b, c) the hot period, and (d, e, f) the changes since pre-Industrial. 43

2.17 The Zonal Diffusivity of Moist Static Energy. The diffusivity of moist static energy (m^2/s), defined as the vertically integrated MSE flux divided by the surface MSE gradient at each latitude for pre-Industrial (dashed) and the hot period (solid) for (a) CanESM5, (b) IPSL-CM6A-LR, and (c) MRI-ESM2-0. 44

3.1 Demographics compared to energy assistance access and eligibility (a) The percentage of the population below 200% of the federal poverty level (FPL) per census tract, and (b) the percent of the population that is non-White. The LIHEAP office locations are in green. Data from Washington Geospatial Open Data from February 2022. 65

3.2 LIHEAP Application Guide. A sample LIHEAP application guide, including a clear, accessible list of required documents. The guide is customizable, so LIHEAP sub-grantees can add their own contact information. 66

3.3 LIHEAP Outreach Material. Sample social media posts aimed toward households with (a-b) undocumented members, in English and Spanish, and (c) indigenous households 67

4.1 SSP GDP Projections. (a) The GDP and (b) GDP per capita of the SSP 1 through 5 baselines (as in, no carbon price) in units of billions of 2005 US dollars per year. Generated from SSP Public Database Version 2. 73

4.2 SSP Per Capita Energy Projections. The final energy per capita across Asia (purple), Latin America (orange), the Middle East and Africa (green), OECD (dark red), and Reforming Economies (blue) for SSP1 (solid lines) and SSP2 (dotted line) in units of millions of EJ per year. Data from the SSP Public Database Version 2. Damerau et al. (2016) shows the population projections for each region to 2050. The regions with the largest to smallest populations are Asia, the Middle East and Africa, OECD, Latin America, and finally the Reforming Economies. Asia has a population approximately 3.6 times as large as OECD, while the Middle East and Africa have the largest rate of population increase. 74

4.3 SSP Carbon Capture Projections. The carbon capture and storage in SSPs 1 through 5, in units of $GtCO_2$ per year. The dashed line represents 2025. Data from the SSP Public Database Version 2. 75

4.4 The Energy Usage and Emissions Across Scenarios. (*i*, left panel) The final (light purple, dashed) and primary (orange, dashed) energy per year, how much is satisfied by each fuel source: biofuels (green), coal (black), crude oil (dark gray), natural gas (light gray), nuclear (purple), hydroelectricity (blue), solar photovoltaic (yellow), wind (light blue), and other renewables (orange). (*ii*, right panel) The total emissions (light purple, dashed) from each source: land use (orange), coal (black), oil (dark gray) natural gas (light gray), biofuel (green), cement and flaring (blue), methane (yellow). This figure includes the following scenarios: (a) Degrowth, (d) Degrowth-fullNETs, (g) Degrowth-NoNNE, (b) Moderate, (e) Moderate-FullNETs, (f) Moderate-NoNNE, (c) Strong, (f) Extreme, and (j) Utopian. 80

4.5 The Energy Usage and Emissions Across Scenarios, *continued*. As Figure 4.4 for the following scenarios: (a) IPCC, (d) IPCC-FullNETs, (g) IPCC-NoNNE, (b) Dec-Moderate, (e) Dec-Strong, (h) DLE, (c) Dec-Extreme, (f) Dec-Extreme-FullNETs, and (j) Dec-Extreme-NoNNEs. 81

4.6 The Total Energy, Emissions, and Cumulative Emissions across Scenarios. Energy, emissions, cumulative emissions and temperature time series for the original K&L scenarios with a methane pathway. (a) The final energy production in EJ, (b) the emissions in $GtCO_2$ (c) the cumulative CO_2 emissions in $GtCO_2$ and (d) the near-surface temperature anomaly in K for (a-d) each scenario from 2020 to 2100. (e) The 1 σ physical variability of the final temperature (5-year average) each scenario from the FaiR ensemble (in color), the 1 σ variability of the scenario mean final temperatures (gray), and the total variability across scenario and ensemble space (black). 82

4.7 A Comparison of CO_2 and CH_4 Pathways to SSPs 1 and 2. The (a) fossil CO_2 and (b) CH_4 emissions for Degrowth (blue), Dec-Extreme (green), IPCC (yellow), Moderate (red), SSP1-1.9 (black, solid), and SSP1-2.6 (black, dashed), and SSP2-4.5 (black, dotted). 84

4.8 Total, CO_2, and CH_4 Radiative Forcings. Timeseries of radiative forcing [W/m^2] of CO_2, CH_4, the sum of CO_2 and CH_4, and the total radiative forcing from all 30 of the modeled gasses in FaIR for Moderate-FullNETs. 85

4.9 Historical and Projected Fossil Fuel Use. Time series of fossil fuel usage from 1990 to 2100 for K&L 2018 parameters (historical until 2018, projections after 2018; shaded), the IEA historical data (up to 2023; solid), and projections using updated initial conditions (Table 4.2) and growth parameters (Table 4.3) from 2023 forward (dashed). 88

4.10 Correlation Between Final Temperature and Cumulative Emissions. A linear regression of the 17 K&L scenario final temperatures against (a) final and (b) maximum cumulative CO_2. 91

4.11 The High, Low, and Overshoot Scenarios. (a-c) The (a) emissions, (b) cumulative emissions, and (c) temperature of the High (dotted), Low (dashed), and Overshoot (solid) experiments for Degrowth (blue), Dec-Extreme (green), IPCC (yellow), and Moderate (red). (d) The temperature variability across the ensemble members for the High (ˆ), Low (o), and Overshoot (x) experiments and all four scenarios. 97

4.12 Timeseries and Frequency of Negative Emissions Technology Efficiency. E_1, as defined by equation 4.8, plotted against absolutely time (2020 to 2100). (b) E_2, as defined by equation 4.9, plotted against time since net zero. The shaded regions represent 1 σ from the ensemble mean (solid). (c) Equation 4.10 plotted against absolute time. The probability distribution function of (d) E_1 and (e) E_2 at 2100. (f) A table of the cumulative carbon capture and storage and the maximum rate of CCS for the four scenarios: Degrowth, Dec-Extreme, IPCC, and Moderate. The gray dashed lines indicate the 1.5°warming target and the 580 $GtCO_2$ carbon budget. 98

4.13 The Transient Climate Response to Emissions. The temperature anomaly [K] plotted against cumulative CO_2 emissions in GtC (upper axis) and $GtCO_2$ (lower axis) for Degrowth (blue, upper left), Moderate (red, upper right), IPCC (yellow, lower left), and Dec-Extreme (green, lower right). The low cumulative emissions (solid), overshoot (dashed), and high cumulative emissions (dotted) are plotted for each scenario. The maximum temperature and 1 σ variability are marked for low (black) and overshoot (gray). 99

LIST OF TABLES

Table Number Page

2.1 Globally Mean Temperature Anomaly. The temperature anomaly [K] in the intermediate period, hot period, and the percentage of warming that has occurred by the intermediate period. 15

2.2 Latitudinal Changes in the Hadley-Walker Circulation. The Latitudinal change in the Hadley-Ferrel Boundary, Ferrel Cell Boundary, ITCZ, and jetstream location in degrees per century. The first value is for the NH and the second value is for the SH (except for the ITCZ which has one location in the NH). The Hadley-Ferrel and ITCZ locations were found by interpolating for subgrid zeros in the 500hPa streamfunction. The outer Ferrel Cell boundary was found by interpolating for subgrid zeros in the zonally averaged zonal wind. The stormtrack was found by interpolating for subgrid zeros in the numerical derivative of surface zonal wind with respect to latitude. Values which do not have a p-value less than 0.05 are *italicized*. All of the regressions are over on yearly averages. 25

2.3 Latitudinal Changes in the Hadley-Walker Circulation against Warming. The Latitudinal change in the Hadley-Ferrel Boundary, Ferrel Cell Boundary, ITCZ, and jetstream location against global mean temperature anomaly (degrees/K). The first value is for the NH and the second value is for the SH (except for the ITCZ which has one location in the NH). See table 2 for methods. All values included have a p-value of less than 0.05. All of the regressions are over yearly averages. 27

3.1 Adapted from the PSE 2022 CETA Energy Assistance Report: A comparison of the difference between the percentage of their customer base and the percentage of energy assistance recipients who reside in highly impacted communities in the PSE service area. See the Chapter 3 data availability section to access Washington State Department of Commerce Utility Reports. 68

4.1 Summary of Scenarios. The names and description of each scenario, the maximum cumulative CO_2 and final cumulative CO_2 above the 580 $GtCO_2$ budget (with and without non-CO_2 gases), the year of net-zero emissions, and the the final temperature (averaged over the last five years) with 1 σ variability from the 6,729-member FaIR ensemble. Scenarios ending in "FullNETs" include point source carbon capture and storage as well as bioenergy carbon capture and storage. Scenarios ending in "NoNNE" includes neither negative emissions technologies nor reforestation. Scenarios ending in "peakCO2" are described in Section 4.3.2 and are not constrained to a 580 $GtCO_2$ budget. All other scenarios have reforestation but no other negative emissions technology. New experiments (as in, those not from K&L) are italicized and not included in Figures 4.4-4.5 or in the range of values stated in the final row. 79

4.2 Fossil Fuel Initial Conditions. The initial demand in each fossil fuel source and total final energy for K&L and ANP. The K&L model begins in 2018, therefore the initial energy demand stems from 2018. The initial conditions for ANP are for 2023. The change in initial fuel demand (difference between ANP and K&L) is in the third column. 88

4.3 Fossil Fuel Growth Parameters. The γ (%/year) and δ (%/%/year) parameters from K&L and updated fossil fuel parameters (labeled ANP) from 2023 IEA data (See the Data Availability section below). 89

4.4 Comparison of Efficiency at 2100 and 30-35 years after net-zero. The final temperature, the year of net-zero (in the overshoot run), magnitude of overshoot (or the maximum cumulative CO_2 in the overshoot and high emissions runs), the efficiency parameter with ZEC and TCRE corrections for 2100 or 30-35 years after Net Zero, and the time to reach 100% efficiency in absolute time and time since net-zero. New experiments are italicized. The highest efficiency and earliest time of 100% efficiency are bolded. (*) Denotes the range of values across scenarios rather than the confidence interval. 103

Chapter 1
INTRODUCTION

As we exceed 1.2°C warming since pre-Industrial, stopping future warming requires almost complete cessation of emissions (Forster et al., 2024). In this dissertation, I explore the uncertainties within (Poletti et al., 2024b), atmospheric changes due to (Poletti et al. (2024a), Chapter 2), adaptations for (Chapter 3), and mitigation pathways to avoid (Chapter 4) catastrophic warming. I begin with an analysis of extreme warming in Global Climate Model (GCM) simulations into 2300, continue to an analysis of Washington State energy assistance policy in a warming world, and end with a coupled economic-climate model to bridge the topics of atmospheric science and climate policy. Ultimately, my graduate research has led me to a variety of topics: the physical climate system and the carbon cycle, complex GCMs and simple globally averaged models, traditional atmospheric science and state-level policy research. Within the surface-level dissonance of these topics lies a through line: a deeper understanding of our climate futures and what we must do to equitably transition into a green future.

1.1 Understanding Future Warming and Carbon Budgets

The Intergovernmental Panel on Climate Change (IPCC), the leading body on climate change research, gives us a 50% (66%) chance of avoiding 1.5°C warming by 2100 if cumulative CO_2 emissions are held below 580 (420) $GtCO_2$ (Rogelj et al., 2018). Recent studies have found that the remaining carbon budget as of 2023 is 250 $GtCO_2$ for a 50% chance of avoiding 1.5°C warming (Lamboll et al., 2023).

Estimating the carbon budget is essential for strategic climate policy to avoid exceedance. The transient climate response to emissions (TCRE) is used to estimate the carbon budget (Matthews et al., 2009):

$$TCRE = \frac{\Delta T}{E_{CO_2}} \quad (1.1)$$

where $TCRE$ warming per unit of cumulative carbon emissions, ΔT is the temperature anomaly and E_{CO_2} is the cumulative carbon emissions. Uncertainties in the carbon budget are primarily caused by uncertainties in TCRE (Rogelj et al., 2018) which are primarily due to the contribution of non-CO_2 emissions (Williams et al., 2020; Jenkins et al., 2021), equilibrium climate feedbacks (the amount of excess radiation absorbed per degree of warming; Williams et al. (2020)), and the carbon cycle (Friedlingstein et al., 2006; Mengis et al., 2018). Therefore, constraining estimates of climate feedbacks is essential to precisely estimate the remaining carbon budget.

1.2 Uncertainties in Climate Feedbacks

One tool to between understand the climate system and its uncertainties are model intercomparison projects, in which several different climate models are run using the same experiments. The Coupled Model Intercomparison Project Phase 6 (CMIP6) includes over 100 models which couple atmosphere, ocean, land, and ice interactions (Eyring et al., 2016). These general circulation or global climate models (GCMs) are highly sophisticated and run using supercomputers at over 50 modeling centers. Experiments such as abruptly increasing CO_2 concentrations from Pre-industral, increasing CO_2 concentrations by 1% each year, or experiments which hold surface ocean temperature constant are used to calculate different statistics about our Earth system, such as equilibrium climate sensitivity, transient climate sensitivity, and the effective radiative forcing.

The climate feedback parameter, a measure of absorbed excess radiation per degree warming, is typically estimated using abrupt-CO_2 change experiments, wherein CO_2 concentrations are abruptly increased from pre-Industrial levels of approximately 280 ppm (and remain stable for 150 years). Using abrupt-CO_2 simulations, we can regress the globally averaged top-of-atmosphere (TOA) radiation (R_{TOA}) against the near surface temperature (Gregory et al., 2004):

$$R_{TOA}(t) = F + \lambda T(t) \quad (1.2)$$

where R_{TOA} is the top-of-atmosphere radiative anomaly, T is the near-surface air temperature anomaly, F is the effective radiative forcing (abbreviated as ERF), and λ is the climate feedback parameter. To estimate equilibrium warming, we can calculate the effective climate sensitivity (EffCS) as the temperature when excess TOA radiation reaches zero:

$$EffCS = T(R = 0) = \frac{-F}{\lambda} \quad (1.3)$$

In contrast to the transient climate response, EffCS is the measure of warming only once the planet has equilibrated, which occurs on the centennial to millennial scale. However, the effective climate sensitivity across GCMs is largely correlated with transient warming (Grose et al., 2018) as well as warming by 2100 (Sherwood et al., 2020), and thus is another important statistic in constraining the carbon budget. Additionally, uncertainty in both EffCS and TCRE is caused by the climate feedback parameter (Zelinka et al., 2020; Williams et al., 2020).

In Poletti et al. (2024b), we compare the climate feedback parameter and EffCS calculated from abrupt-CO_2 quadrupling experiments (approximately 1120 ppm; abrupt-4xCO_2) to those calculated from abrupt-CO_2 doubling experiments (approximately 560 ppm; abrupt-2xCO_2) using data from the Coupled Model Intercomparison Project Phase 6 (CMIP6). Though abrupt-4xCO_2 simulations are typically used to calculate EffCS, abrupt-2xCO_2 simulations more closely align with new future warming: in 2022, the global atmospheric CO_2 concentration was approximately 418 ppm which is 50% higher than pre-Industrial (Friedlingstein et al., 2022).

Additionally, it is known that the EffCS estimated using abrupt-4xCO_2 experiments (EffCS4x) is larger than that estimated using abrupt-2xCO_2 experiments (EffCS2x) even when dividing EffCS4x by a factor of two to account for its forcing being approximately twice that of abrupt-2xCO_2 (Meraner et al., 2013; Good et al., 2015; Gregory et al., 2015; Mitevski et al., 2021; Bloch-Johnson et al., 2021). This fractionally-larger warming at higher forcing levels can arise from higher EffCS due to more-positive cloud (Bloch-Johnson et al., 2021) or

water-vapor feedbacks (Meraner et al., 2013), and/or the ERF scaling non-logarithmically with CO_2 concentration (Byrne and Goldblatt, 2013; Etminan et al., 2016; Mitevski et al., 2022). In contrast, the TCRE is thought to be path-independent (Zickfeld et al., 2012). However, recent literature has questioned the path-independence of TCRE due to a lag in the sequestration of CO_2 by the ocean and land (Winkler et al., 2024). Similarly, Poletti et al. (2024b) finds that differences in EffCS_{4x} and EffCS_{2x} are in part due to ocean heat uptake.

In Poletti et al. (2024b), we normalized the EffCS_{4x} by the model-specific ERF and found two GCMs(CESM2 and MRI-ESM2-0) out of a 10-model ensemble remained significantly colder at abrupt-2xCO_2 than abrupt-4xCO_2 (both in terms of transient warming and EffCS; Figure 1.1a). The difference in EffCS_{4x} and EffCS_{2x} in these models could not be explained by the mechanisms above. Using a linear energy balance model,

$$\frac{d}{dt}(C(t) \times T(t)) = F + \lambda T(t) = R_{TOA}(t) \quad (1.4)$$

where C is the effective heat capacity of the Earth and t is time, we calculated what percentage of the difference in EffCS_{4x} and EffCS_{2x} corresponded with the climate feedback parameter or with the effective heat capacity. We found that in models where experienced disproportionate Atlantic Meridional Overturning Circulation (AMOC) in abrupt-2xCO_2 (which was the case in CESM2 and MRI-ESM2-0) declined by more than 50% of the decline in abrupt-4xCO_2 models, the effective heat capacity was a significant factor in warming differences (Fig 1.1d-f). AMOC decline impacted both the climate feedback and the heat capacity in these models, through an increase in low clouds and depth of heat storage in the Atlantic Ocean. Poletti et al. (2024b) provides insight into uncertainties in the climate feedback parameter from cloud effects (which are the largest source of uncertainty in estimates of the climate feedback parameter; e.g., Zelinka et al. (2020)) and justification for the use of abrupt-2xCO_2 simulations in projecting warming by 2100. However, uncertainties in the climate system are outweighed by uncertainties in how economic choices will impact 2100 warming.

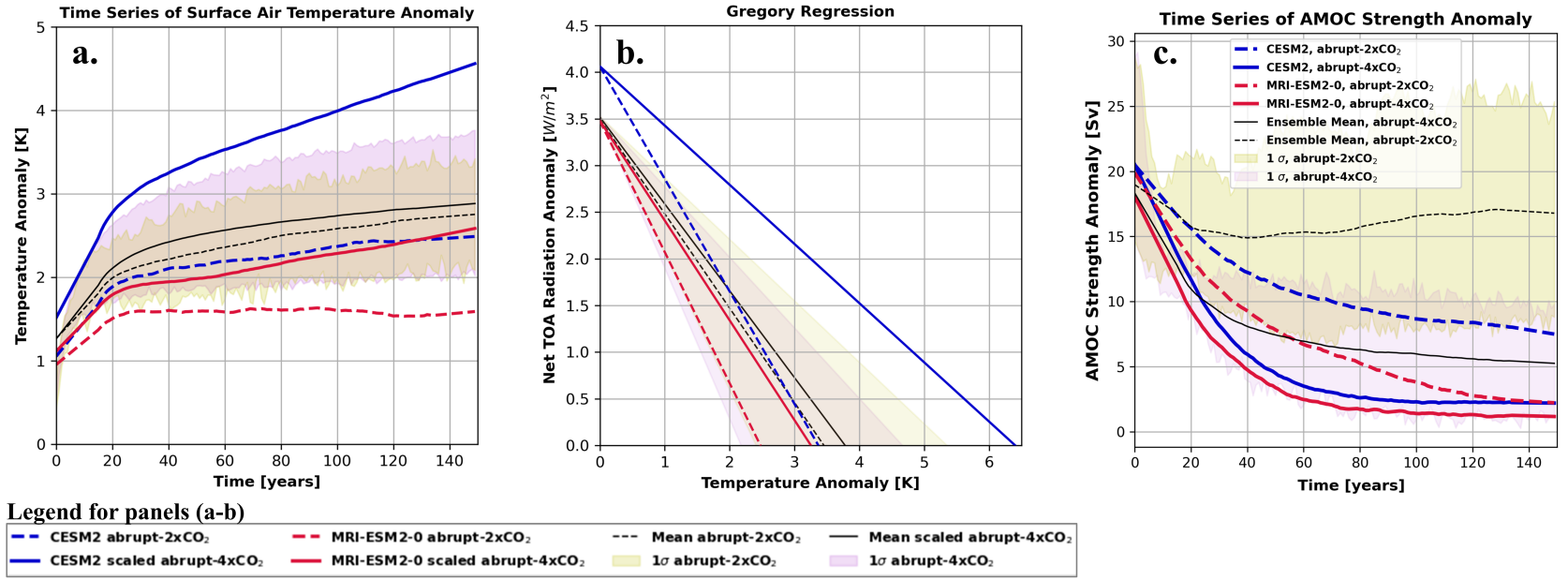

Figure 1.1: *From Poletti et al. (2024b).* (a) Surface temperature anomaly against time, (b) the net TOA radiative flux against surface temperature anomaly (see equation 1.2). (c) The AMOC strength anomaly against time. The abrupt-4xCO_2 data is normalized in (a-b) using the effective radiative forcing

1.3 Shared Socio-Economic Pathways

CMIP6 sought to constrain scenario uncertainty through the Shared Socio-Economic Pathway (SSPs) experiments. The SSPs are defined by their socio-economic storylines (labeled 1 through 5 with increasing climate mitigation and adaptation challenges) and the increase in radiative forcing compared to pre-Industrial (from 1.9 W/m^2 to 8.5 W/m^2; O'Neill et al. (2016)). SSP1 is a "green growth paradigm" in which net-zero targets are prioritized and international cooperation occurs whereas SSP5 (called "fossil-fueled development") in which emissions are not mitigated despite economic development.

These socio-economic storylines are modeled using Integrated Assessment Modeling (IAMs). Parameters on climate mitigation and adaptation challenges as well as economic parameters such as an increasing gross domestic product are input into the IAM, which outputs the subsequent emissions. The concentrations resulting from those emissions are input into GCMs which output climatological fields such as temperature. CMIP6 simulations typically run to 2100, however there are a set of extended SSP runs (which continue to 2300) are are examined in Chapter 2. While there are scenarios such as SSP1-4.5 which presume low challenges to climate mitigation but high warming (or SSP5-1.9, which presumes high challenges to climate mitigation but low warming), CMIP6 chose a subset of SSP scenarios which are called "standard pathways." The standard pathway scenarios include SSP1-1.9 and SSP5-8.5; the emissions pathways in SSP1-1.9 are used throughout Chapter 4 while Chapter 2 analyzes the SSP5-8.5 extension run.

1.4 Negative Emission Technologies and Deemphasizing Economic Growth

Certain SSP scenarios seem implausible; as in, how can a world with major challenges to climate mitigation maintain excess radiative forcing to 1.9 W/m^2 (SSP5-1.9)? Negative emissions technologies (NETs) are technologies which reduce CO_2 emissions from the atmosphere and subsequently sequester the CO_2 or reuse it as an energy source. SSP scenarios depend on NETs to reach warming targets. In fact, even the coldest SSP scenario, SSP1-1.9, takes up more than 15 $GtCO_2$ year using NETs in 2100. IAMs reconcile indefinite economic growth (seen though monotonically increasing gross domestic product, GDP) with net-zero emis-

sions targets by employing negative emissions technologies. Ultimately, NETs are necessary because the SSPs don't consider climate futures which are agnostic to increasing economic consumption.

However, not only is GDP a poor indicator of human wellbeing, there are massive inequalities in consumption across the globe which are not rectified in SSP scenarios. Energy inequality exists in every SSP scenario across regions (Rao et al. (2019), Cuaresma (2017), Figure 4.1) and within regions (Chapter 3 discusses the unequal impacts of energy insecurity in Washington State under climate change). The average American uses 3 to 4 times more energy than the global average person and approximately 15 times more than the decent living standard (Milward-Hopkins et al., 2020). Increases in consumption in high GDP nations lead to increasingly marginal increases in wellbeing; in contrast, low GDP nations see huge gains in wellbeing from small increases in energy access (Rao and Min, 2018; Milward-Hopkins et al., 2020; Vogel et al., 2021). Therefore, there may exist climate futures where the redistribution of current energy usage maximizes wellbeing, without depending in indefinite economic growth. In fact, less than half of our current energy demand is necessary to provide a decent standard of living for everyone by 2050 (Rao and Min, 2018). These scenarios are called agrowth, degrowth, or low energy demand scenarios.

This dissertation will discuss the climatological impacts of extreme warming (Chapter 2), the inequities in energy assistance within Washington state as heat wave risk increases (Chapter 3), and finally the temperature projections of low energy demand scenarios in comparison to scenarios dependent on negative emissions technologies (Chapter 4).

Chapter 2

ATMOSPHERE AND OCEAN ENERGY TRANSPORT IN EXTREME WARMING SCENARIOS

Adapted from: Poletti, A., Frierson, D., Aerenson, T., Nikumbh, A., Carroll, R., Henshaw, W., and Scheff, J. (2024a). Atmosphere and Ocean Energy Transport in Extreme Warming Scenarios. *PLOS Climate*

2.1 Introduction

CO_2 concentrations are higher than in 10 million years (Tripati et al., 2009). Industry-induced changes to atmospheric compositions have already drastically changed our climate through extreme weather events (Baker et al., 2018; Clarke et al., 2022), such as heat extremes (Bartusek et al., 2021; Tripathy et al., 2023), severe droughts, and heavy precipitation (Karmalkar and Bradley, 2017; Haile et al., 2020). Further, the CO_2 which has already been emitted will remain in the atmosphere for millennia (Archer, 2016; Clark et al., 2016; Lyon et al., 2021). Long-term consequences of high CO_2 concentrations include ice sheet melt and sea level rise, which will continue to increase for many centuries (Fox-Kemper et al., 2021), while temperatures stay high and other climate impacts persist (Lee et al., 2023). Yet, global climate model (GCM)-based investigations into future climate change typically stop at the end of the 21st century.

CMIP5 (Coupled Model Intercomparison Project Version 5) (Vuuren et al., 2011; Meinshausen et al., 2011) had the first scenarios with emissions and concentrations extended to 2300, known as the Extended Concentration Pathways (ECPs). The ECPs were used in Chapter 12 of the Working Group 1 contribution to the IPCC 5th Assessment report (AR5) (Collins et al., 2013), most prominently in a section on climate change beyond 2100. Most of the ECP8.5 experiments analyzed in AR5 were run using Earth-System Models of Intermediate Complexity (EMICs) (Zickfeld et al., 2013; Jahn and Holland, 2013; Meehl et al.,

2012). Global-mean temperature and Atlantic Meridional Overturning Circulation (AMOC) at 30°N were analyzed for the few fully-coupled GCMs as well as the ECPs. Within GCMs, the global temperature increases by 4 to 15 K and the AMOC at 30°N decreases by a factor of 2 to 6 in RCP8.5 extension experiments in Collins et al. (2013), in 2300 as compared with the pre-Industrial climate.

Other work using the high radiative forcing ECPs has highlighted some unique aspects of the very high temperature climates. For studies of sea ice, this includes annually ice-free conditions in the Arctic (Hezel et al., 2014; Drijfhout et al., 2015); and mechanisms of abrupt Arctic winter sea ice loss (Bathiany et al., 2016; Hankel and Tziperman, 2001). Another focus of prior work was the lack of abrupt changes in the AMOC, despite a diversity of changes in strength across models (Weaver et al., 2012). For the CMIP6 data solicitation the Scenario Model Intercomparison Project (ScenarioMIP) requested fully coupled runs of a new high-emissions scenario called the shared socio-economic pathway 5 with 8.5 W/m^2 at 2100 (SSP5-8.5) to be simulated to the year 2300 (hereafter referred to as SSP5-8.5ext)(O'Neill et al., 2016). In Section 4.7.1.2 of the Working Group 1 contribution to the IPCC 6th Assessment Report (AR6), the SSP5-85ext simulations are studied, showing global temperature ranging from 9-17°C above pre-Industrial, global land precipitation increasing by 0.3-0.6 mm/day, and no September Arctic sea ice (Fox-Kemper et al., 2021).

This study examines the SSP5-8.5ext extreme warming scenario from three different CMIP6 climate models, with simulations integrated until 2300. In particular, we focus on the poleward transport of heat in the much warmer climate and on related variables such as temperature, humidity, precipitation, radiation, and circulation in the atmosphere and ocean. Since water vapor increases rapidly with temperature, we hypothesize large increases in the poleward transport of latent energy within midlatitudes, and equatorward transport within the tropics (Pierrehumbert, 2002; Held and Soden, 2006). Increased latent energy flux may result in weakened equator-to-pole temperature gradients, which would decrease the poleward transport of dry static energy and potentially weaken eddies (Frierson, 2007). Many previous studies have suggested the usefulness of diffusion of moist static energy to understand changes in atmospheric heat transport in different climate regimes (Frierson,

2007; Flannery, 1984; Hwang and Frierson, 2010; Roe et al., 2015; Siler et al., 2018; Armour et al., 2019). Large weakening of eddies would likely imply large decreases in diffusivity, which is not always included in energy balance models.

An additional factor of importance is the response of the ocean circulation to increasing temperature. Since the AMOC plays an important role in determining temperature gradients at a global scale (Kang et al., 2015; Lin et al., 2019), there will likely be interactions among the AMOC, temperature gradients, and dynamics. Wind-driven ocean circulation responds to changes in tropical and midlatitude surface winds associated with processes such as the poleward expansion of the tropics (Seidel et al., 2008), the poleward shift of midlatitude eddies (Staten and Reichler, 2014), and changes in strength of the Hadley cell (Hu et al., 2018; Vecchi and Soden, 2007), among other phenomena.

This paper is organized as follows: Section 2.2 describes the model simulations used in this study. In Section 2.3 we begin by showing, first, changes in temperature, humidity and net precipitation, along with the atmospheric circulation, which helps to explain aspects of the precipitation changes in both the tropics and the extratropics, and second, an analysis of how the poleward transport of energy changes in the warmed climate, including moist and dry static energy, and ocean heat transport. We additionally examine the role of cloud-radiative effects and midlatitude eddy intensity, arguing that both cloud effects and eddy intensity are important for determining how energy is transported. In Section 2.4 we further discuss our results and state conclusions.

2.2 Methods & Models

The SSP5 set of scenarios represents intense development across the world, powered by fossil fuels (O'Neill et al., 2016). The SSP5-8.5 scenario in particular reaches very large radiative forcing of approximately 8.5 W/m^2 by 2100 (Figure 2.1a), higher than any other scenario. By 2100 in SSP5-8.5, CO_2 concentrations are 1135 ppm, and CO_2 makes up 82% of the radiative forcing in SSP5-8.5 at 2100 (Figure 2.1b) (Meinshausen et al., 2011). It is generally thought that the emissions in the RCP8.5 scenario were unrealistically large given the recent trajectory of energy across the world (Hausfather and Peters, 2020), and

the SSP5-8.5 scenario is probably similarly unlikely during the 21st century. It should be noted however that all SSP and RCP scenarios (extension or not) are concentration-forced, not emissions-forced. This means that each concentration pathway could be generated with a different emissions pathway, and a larger or smaller than expected carbon cycle response.

In SSP5-8.5ext, emissions ramp downwards from 2100 levels to zero in 2250, for fossil CO_2 and non-CO_2 emissions. Land-use related non-CO_2 emissions are held steady at 2100 values, and land-use CO_2 emissions are ramped up to zero by 2150. The other two extension scenarios in CMIP6, SSP1-2.6 and SSP5-3.4-OS, involve large mitigation efforts, so the SSP5-8.5ext scenario is the only high radiative forcing scenario run past 2100 in ScenarioMIP.

The SSP5-8.5ext scenario in 2300 has 2162 ppm CO_2 ($\approx$ 12.5 W/m^2 radiative forcing), 1112 ppb CH_4 (0.2 W/m^2 radiative forcing), and 410 ppb N_2O (0.4 W/m^2) (Figure 2.1a). Land-use forcing is -0.2 W/m^2 and other forcing agents, including aerosols, F-gases, and tropospheric ozone have absolute value less than 0.1 W/m^2. The total radiative forcing of 13.0 W/m^2 in 2300 is thus almost exclusively due to CO_2. The ECP8.5 scenario from CMIP5 had a slightly larger total forcing in 2300, with more forcing from methane, and a different time dependence. In this study, we focus on the SSP5-8.5 simulations only.

There are three models that have run the SSP5-8.5ext simulations: CanESM5, from the Canadian Centre for Climate Modeling and Analysis (Swart et al., 2019), MRI-ESM2-0 (Yukimoto et al., 2019), from the Meteorological Research Institute, and IPSL-CM6A-LR (Boucher et al., 2020), from the Institut Pierre-Simon Laplace. Fan et al. (2020) compares an ensemble of 16 GCMs to three periods of observed historical warming trends (°C/decade) from 1901 to 2014. This analysis found that CanESM5 and IPSL-CM6A-LR overestimate warming trends from 1941 to 2014, which could indicate an overly large sensitivity to radiative forcing in these two models. MRI-ESM2-0 underestimates warming trends from 1941 to 1970 and overestimates warming trends from 1971 to 2014. All three models approximately reproduce historical warming trends from 1901 to 1940. Much of our analysis consists of comparison among three climate states. The first time period is the simulated pre-Industrial climate (piControl), where the atmospheric constituents are set to 1850 levels. We average over the final 100 years of the piControl simulation to avoid simulation drift during earlier

portions while the model is equilibrating. The second time period is the average of the years 2076-2100 in the SSP5-8.5 simulations, henceforth referred to as the "intermediate period," and the third time period is from 2276-2300 of the SSP5-8.5ext, which we call the "hot period." The intermediate period of SSP5-8.5 has been widely studied both in comparison with the piControl climate, and with the other members of the ScenarioMIP suite of simulations (Tebaldi et al., 2020; Narsey et al., 2022), hence the intermediate period is a useful comparison point for the "hot period," which experiences extreme warming.

2.3 Results

2.3.1 Basic Climatological Fields

a. Surface Temperature

Global averaged 2-meter surface air temperature change is plotted for each model in Figure 2.1b. The globally-averaged temperature change in these three models in the intermediate and hot period, as well as the percentage of total warming that occurs by the intermediate period is shown in Table 2.1 and Figure 2.1b. Roughly half of the total warming occurs by the intermediate period, and models with more warming experience a smaller fractional change pre-2100.

The equilibrium climate sensitivities to doubling CO_2 of CanESM5, IPSL-CM6A-LR, and MRI-ESM2-0, calculated using the method derived by Gregory et al. (2004), and compiled for CMIP6 by Meehl et al. (2020), are 5.6°C, 4.6°C, and 3.2°C, respectively. The transient climate responses for CanESM5, IPSL-CM6A-LR, and MRI-ESM2-0 are 2.8°C (Swart et al., 2019), 1.96°C (Boucher et al., 2020), and 1.64°C (Meehl et al., 2020), respectively. The ratio between the hot period anomalous temperature change and the equilibrium climate sensitivity are close to 3 for each model; the TCR has a less consistent relationship with the hot period warming, which is expected since the models have been at a stable forcing for more than a century by the end of the run (Figure 2.1a). The ratio of radiative forcing in the hot period (13.0 W/m^2) to the forcing of doubling CO_2 (3.7 W/m^2) is 3.5, which suggests that the hot period warming is slightly less than would be expected from a linear, equilibrium response to the radiative forcing. From Figure 2.1b, it is clear that all three models are still

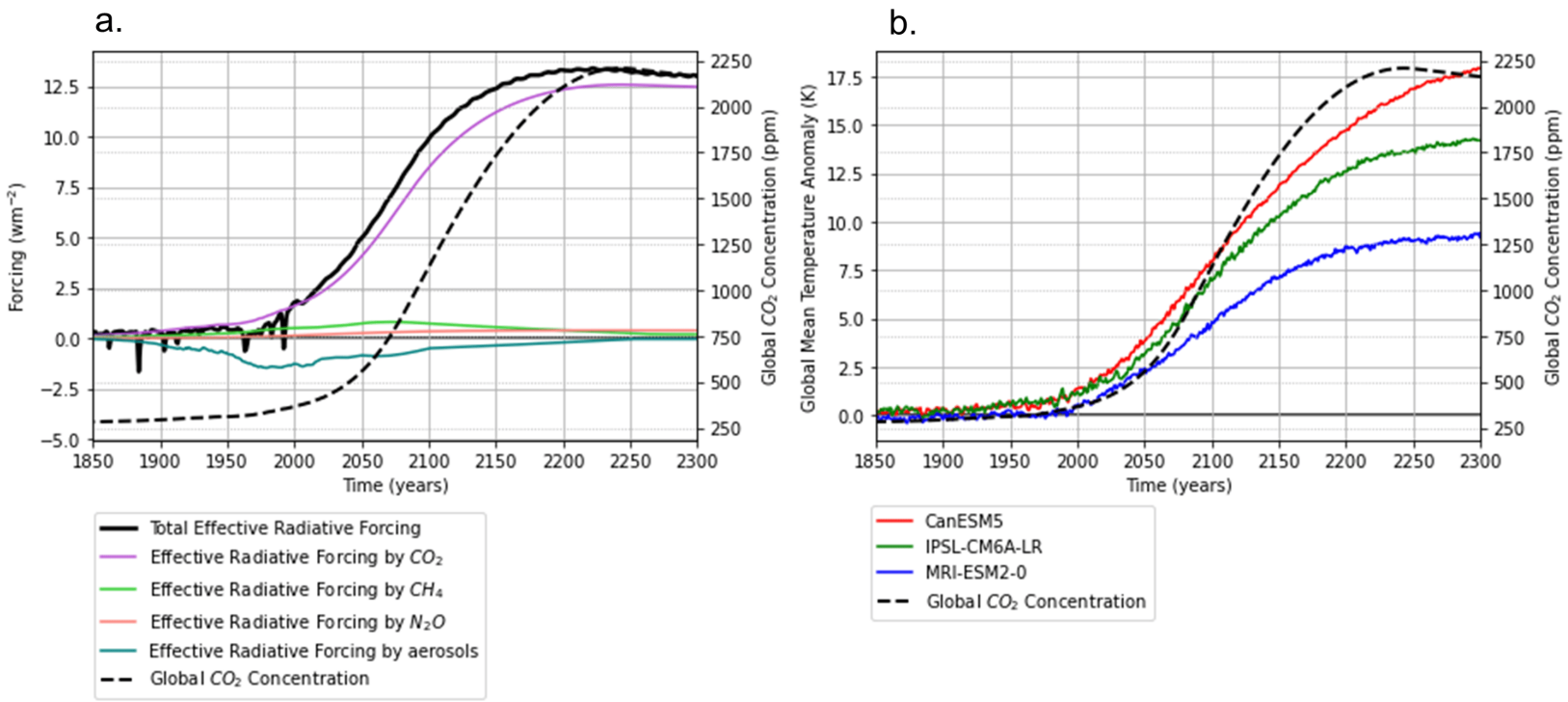

Figure 2.1: SSP5-8.5ext Greenhouse Gas Concentrations and Forcings. (a) The effective radiative forcing of CO_2, CH_4, N_2O, aerosols, and total against time for SSP5-8.5ext simulations (solid) and the global CO_2 concentration (dashed) against time for SSP5-8.5ext simulations. (b) The global mean temperature anomaly for CanESM5, IPSL-CM6A-LR, and MRI-ESM2-0 (solid) against time for historical (1850-2015) and SSP5-8.5ext (2015-2300), and the global CO_2 concentration (dashed) against time for SSP5-8.5ext.

warming in 2300, despite the near-constant forcing over the previous century.

The 2-meter surface air temperatures averaged over the hot period are shown in Fig 2 alongside their anomalies from pre-Industrial and the percentage of the total change that occurs during the simulation happens during the 21st century,

$$= \frac{\Delta T_{intermediate}}{\Delta T_{hot}} \times 100\% \quad (2.1)$$

In the right-hand column of Figure 2.2, blue coloration indicates regions where there is more warming between the intermediate period and the hot period than occurs between the pre-Industrial and intermediate periods (and vice-versa for red coloration). The plots are presented in descending order of climate sensitivity: CanESM5, IPSL-CM6A-LR, and MRI-ESM2-0. In each model there are regions where the annual mean temperature over tropical continents exceeds 40°C in the hot period, and in CanESM5, nearly the entire tropics exceeds 40°C in the annual mean. In CanESM5, tropical warming happens more between the intermediate period and the hot period, as indicated by the blue colors in Figure 2.2g. In IPSL-CM6A-LR, tropical heating occurs approximately equally before and after 2100 (Figure 2.2h). Whereas, in MRI-ESM2-0, tropical heating occurs primarily before the intermediate period, as shown by the red coloring in Figure 2.2i. In the hot period in CanESM5 and IPSL-CM6A-LR, the 0°C annual average contour only exists over Antarctic and Greenland ice sheets (the topography of which is prescribed). MRI-ESM2-0 also has a small region below freezing in the Himalayas.

The middle column of 2.2 shows the temperature anomaly during the hot period, compared to the piControl climatology. The changes are greatest for each model in the Arctic, which is consistent with the polar amplification that has been widely studied (Washington and Meehl, 1996; Holland and Bitz, 2003; Serreze et al., 2009). In CanESM5 and IPSL-CM6A-LR the Arctic warming exceeds 30°C, and in MRI-ESM2-0 it gets as high as 25°C. In each model the average warming north of 60°N is 26.5°C, 23.7°C, and 16.2°C for CanESM5, IPSL-CM6A-LR, and MRI-ESM2-0 respectively. The Arctic warming of each model is between a factor of 1.5 and 1.75 greater than the global average, with MRI-ESM2-0 having the strongest Arctic amplification ratio of 1.74, then IPSL-CM6A-LR with 1.69, and CanESM5

Global Mean Temperature Anomaly			
Model	Intermediate Period [K]	Hot Period [K]	Percentage [%]
CanESM5	8.13	17.5	46.5
IPSL-CM6A-LR	7.10	14.0	50.7
MRI-ESM2-0	4.95	9.3	53.2

Table 2.1: Globally Mean Temperature Anomaly. The temperature anomaly [K] in the intermediate period, hot period, and the percentage of warming that has occurred by the intermediate period.

has the lowest amplification ratio of 1.51. In each model, more than half of the Arctic warming occurs by 2100 (Figure 2.2g-i). Namely, the impact of Arctic amplification is most prominent before 2100, likely due to substantial sea ice loss by 2100 (Washington and Meehl, 1996; Holland and Bitz, 2003; Serreze et al., 2009). Ono et al. (2022) showed that the rate of sea-ice loss with increasing temperature is non-monotonic in SSP5-8.5 because once the sea-ice extent is sufficiently small, the loss rate is lower than occurs in a cooler climate (even with greater amounts of warming).

Outside of the Arctic, the greatest warming is seen over subtropical land areas, with temperature changes that are often 50% higher than the global average warming in each model. CanESM5 shows particularly large warming over Southern Africa, Australia, and equatorial South America, with temperature changes that are 70% larger than the global mean. Equatorial South America has a rather different temperature change across the three models. There is variability across these models regarding when land warming occurs. In CanESM5, the pronounced warming over Southern Africa and Australia occurs primarily between the intermediate and hot periods. In IPSL-CM6A-LR, the warming over Southern Africa, Australia, and equatorial South America occurs nearly equally before and after the intermediate period. Finally, in MRI-ESM2-0, warming over those three regions occurs primarily before the intermediate period.

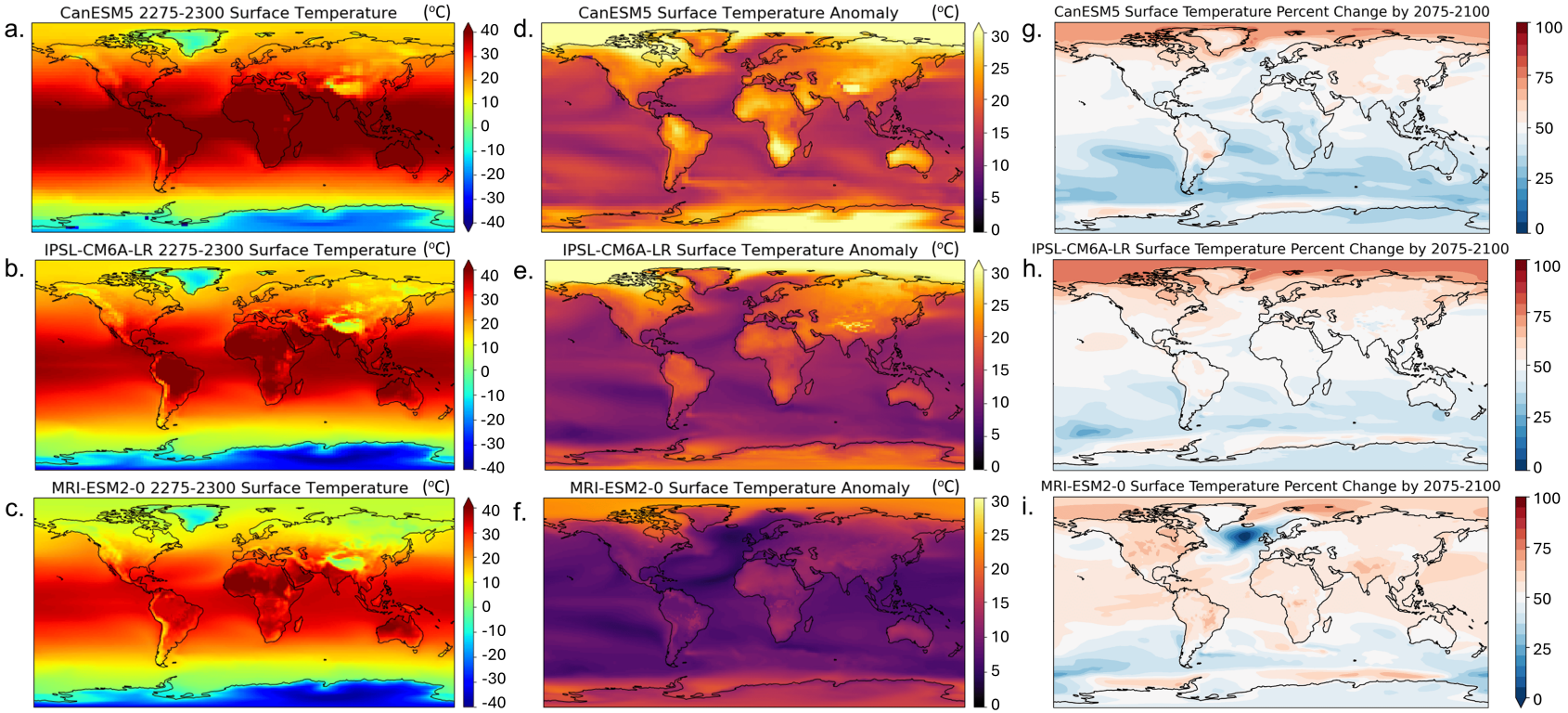

Figure 2.2: Maps of the Near Surface Air Temperature. (a, b, c) Near-surface temperature averaged over the hot period, (d, e, f) the hot period temperature anomalies relative to pre-Industrial, and (g, h, i) the percent change in surface temperature by the intermediate period, calculated as the ratio of the intermediate period temperature anomalies divided by the hot period temperature anomalies relative to pre-Industrial.

b. Surface Humidity

Figure 2.3 shows the surface specific humidity anomalies for the hot period and the percentage of the total change that occurs by the intermediate period. The specific humidity is shown in units of Kelvin (which is converted by multiplying by the ratio of latent heat of vaporization of water and the specific heat at constant pressure of air). This convention has greater utility for use in interpreting moist static energy (MSE) which we examine later in the paper.

The tropical specific humidity more than doubles in CanESM5 and IPSL-CM6A-LR and increases by a factor of 1.6 in MRI-ESM2-0. In CanESM5 and IPSL-CM6A-LR, globally the majority of specific humidity changes occur after 2100 (Figure 2.3d-f), in part due to nonlinearity in the Clausius-Clapeyron relation. Exceptions to this include the Atlantic Ocean east of Greenland in CanESM5 and IPSL-CM6A-LR, parts of west and central Africa in CanESM5, and parts of the tropics and Northern Hemisphere (NH) land in MRI-ESM2-0, in which there are larger changes in the intermediate period.

In all three models, the spatial pattern of the percentage change in specific humidity that occurs prior to 2100 is similar in structure to that of surface temperature in regions outside of the Arctic. In CanESM5 and IPSL-CM6A-LR, the Southern Hemisphere sees more warming in the hot period than the intermediate period (blue coloration in Figure 2.2g-i), which contributes to larger increases in specific humidity in the Southern Hemisphere in the hot period. While the Arctic warms more in the intermediate period than the hot period (red coloration in Figure 2.2g-i), the specific humidity changes occur mostly in the hot period (in CanESM5) or equally in either period (IPSL-CM6A-LR); this is due to the nonlinearity of the Clausius-Clapeyron equation under the very large Arctic temperature changes.

Figure 2.4 shows the relative humidity anomalies of the hot period and intermediate periods relative humidity anomalies from pre-Industrial for the hot period, the intermediate periods, and as well as the difference between the hot and intermediate period. The surface relative humidity change is characterized by small increases over most ocean areas in each model (Figure 2.4). Exceptions to this are in the Arctic, where relative humidity decreases in each model.

The relative humidity changes above land masses are very different from model to model. The IPSL-CM6A-LR model shows substantial drying over nearly all continental regions by 2300. This drying occurs primarily before the intermediate period, especially in the Arctic and the Amazon. CanESM5 has even larger relative humidity changes over some land locations like the Amazon and the Congo Rainforest but has increasing humidity over Arctic and some tropical locations. The drying in the Amazon occurs primarily before the intermediate period, while the majority of drying in the Congo Rainforest occurs after 2100. The relative humidity change in the MRI-ESM2-0 model is qualitatively similar to that of CanESM5 with significantly less amplitude change. It is expected that global warming causes declines in relative humidity over land (Sherwood and Fu, 2014; Byrne and O'Gorman, 2016, 2018; Lee et al., 2023). Specific humidity over land tends to increase proportionately to specific humidity over ocean; thus, the percent increase in specific humidity with climate change is controlled by ocean warming, which is smaller than land warming (Sherwood and Fu, 2014; Byrne and O'Gorman, 2016).

Figure 2.5 displays the zonal mean of specific and relative humidity, comparing the hot period to pre-Industrial. Specific humidity in the Arctic increases by a much larger fraction than in the tropics. In latitudes greater than 60°N, average moisture increases by factors of 5.1, 4.4, and 2.9 for CanESM5, IPSL-CM6A-LR, and MRI-ESM2-0 respectively. The large increase in Arctic moisture content can be explained by the large Arctic warming observed in all three models, since the relative humidity in Figures 2.4 and 2.5 show a slight decrease.

c. Precipitation

Precipitation minus evaporation (net precipitation) patterns are shown in Figure 2.6. The three columns display net precipitation anomalies for the hot period from pre-Industrial, the intermediate period from pre-Industrial, and the hot period from the intermediate period (left to right). Precipitation changes are characterized by a wet-get-wetter pattern that is familiar in global warming scenarios, in which precipitation increases in ascent regions such as the deep tropics, and along the Kuroshio, Gulf Stream, and decreases in subtropical descent regions (Held and Soden, 2006). Nearly all locations in the polar regions of both

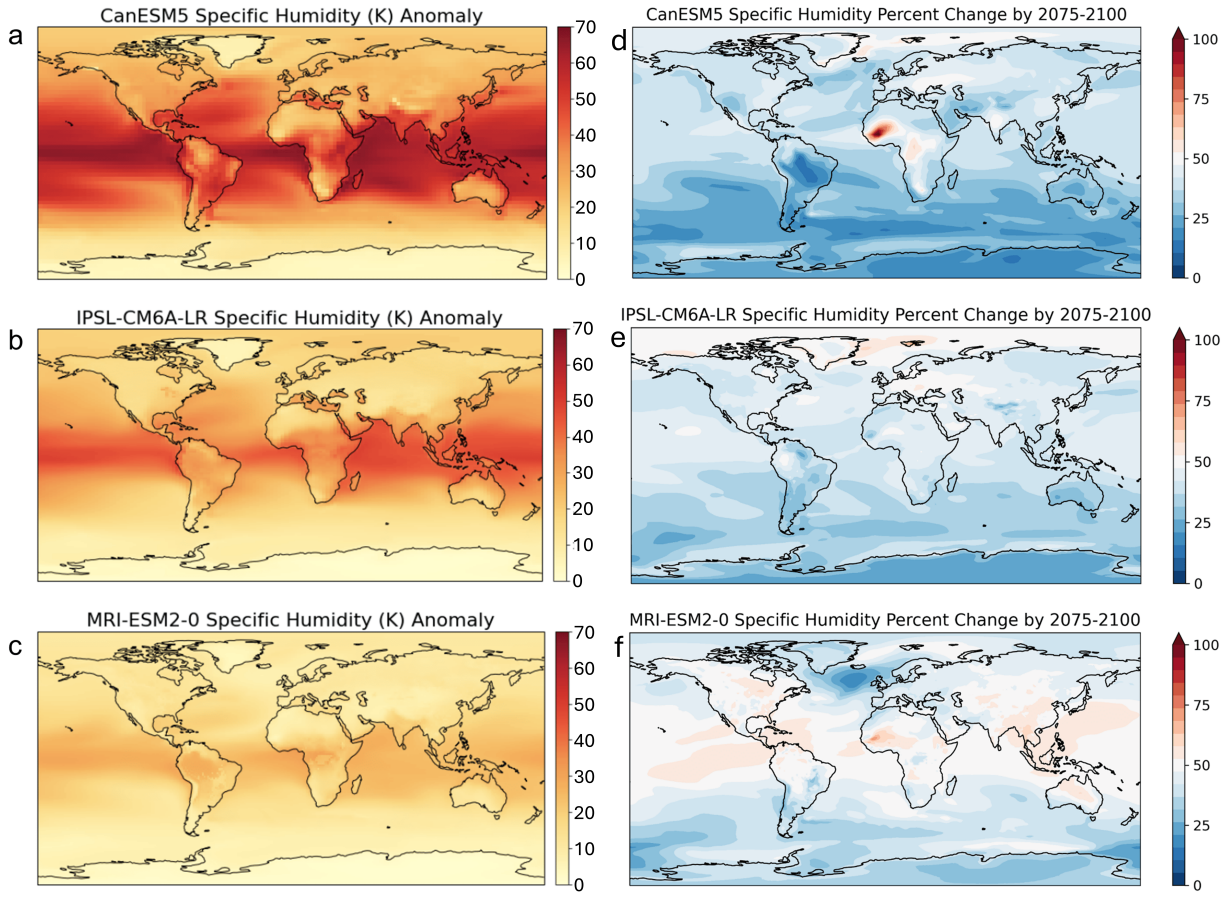

Figure 2.3: Maps of the Specific Humidity Anomaly (a, b, c) Anomalies of surface specific humidity relative to pre-Industrial, and (d, e, f) the percent change from the intermediate period to the hot period, calculated as the ratio of the surface specific humidity anomaly in the intermediate period and the anomaly in the hot period.

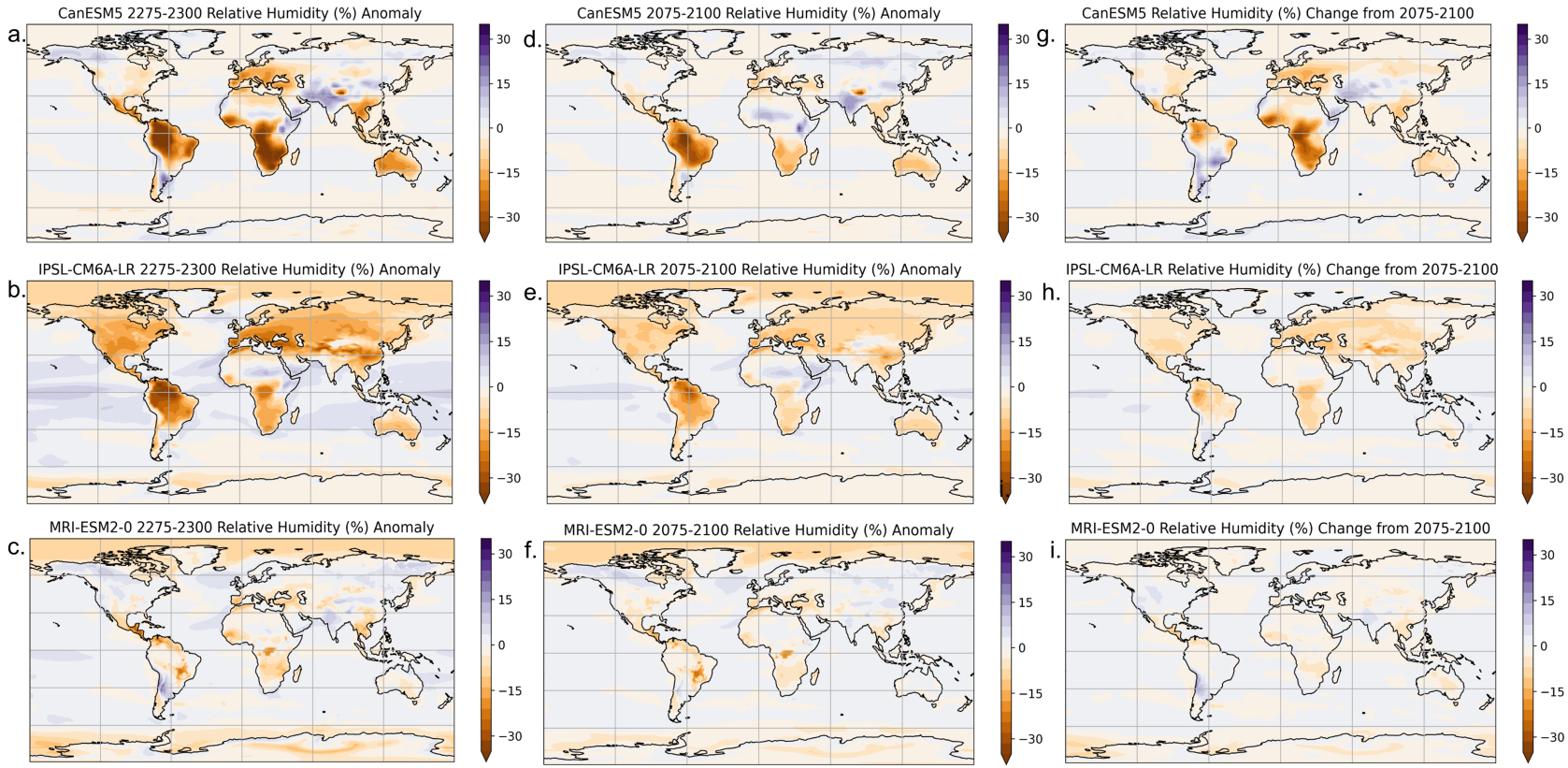

Figure 2.4: Maps of the Relative Humidity Anomaly. (a, b, c) Anomalies of surface relative humidity in the hot period relative pre-Industrial, (d, e, f) anomalies of surface specific humidity in the intermediate relative pre-Industrial, and (g, h, i) the relative humidity change from 2075-2100, calculated as the hot period relative humidity minus the intermediate period relative humidity.

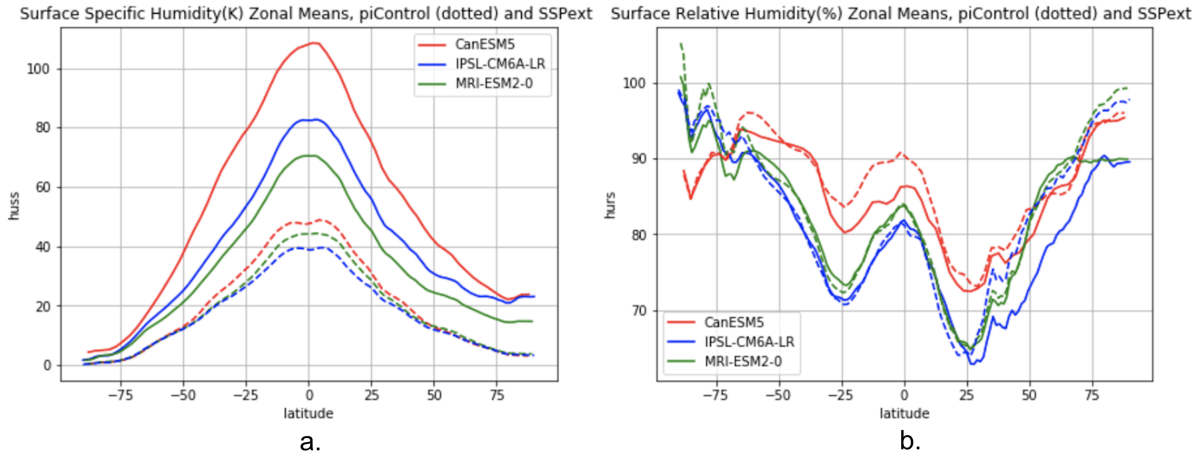

Figure 2.5: Zonally Averaged Specific and Relative Humidity. (a) The specific humidity (labeled "huss") and (b) relative humidity (labeled "hurs") zonal means, for the hot period (solid) and pre-Industrial (dashed).

hemispheres show increases in precipitation. Many subtropical areas experience drying, as do locations on the equatorward edge of the midlatitude storm track, which is in line with the multi-model-mean precipitation patterns taken during the first century of the ScenarioMIP runs (Fan et al., 2020). Poleward shifts of circulation, which are analyzed in the next subsection, in part determine the subtropical drying. Drying in sub-Saharan Africa occurs preferentially between the intermediate and hot periods for all models (Figure 2.6). In particular, the drying in tropical Africa between the intermediate and hot periods suggests that the more familiar CMIP wetting response in this region (e.g. between the pre-Industrial and intermediate periods in Figure 2.6) is not fundamental, corroborating the general lack of confidence in this wetting (Yang et al., 2014; Giannini et al., 2018).

There are several areas with significant model-to-model differences in the pattern of precipitation. Equatorial Africa moistens in IPSL-CM6A-LR while it dries or exhibits more complex patterns in the other two. These precipitation changes over land explain some of the differences in the surface relative humidity changes. The Atlantic Inter-Tropical Convergence Zone (ITCZ) also exhibits a southward shift in the MRI-ESM2-0 model. While the magnitude of net precipitation changes are roughly equal before and after the intermediate period,

changes near the ITCZ occur differently across the models. In CanESM5, north of the Pacific ITCZ has a positive net precipitation anomaly in the intermediate period, but a negative anomaly between the intermediate period and the hot period. Similar areas of drying north of the ITCZ in the later period can be seen in the other two models as well.

d. Atmospheric Circulation

The zonally-averaged streamfunction in pre-Industrial (black contours) and the hot period anomaly from pre-Industrial (colors) is plotted in Figure 2.7a-c. The zonally-averaged streamfunction at 500hPa for the pre-Industrial (dotted), the intermediate period (dashed), and the hot period (solid) is plotted in Figure 2.8. The change in the zonally-averaged streamfunction has a complex structure, due to distinct physical processes occurring at different heights and latitudes. In each of the three models, there are streamfunction changes associated with the increase in tropopause height (Hu and Vallis, 2019), the weakening of the Hadley cells (Vecchi and Soden, 2007), and the widening of the Hadley Cells (Lu et al., 2007).

The increased depth of the Hadley cells can be identified by the positive anomaly above the NH Hadley cell, and the negative anomaly above the Southern Hemisphere (SH) Hadley cell (these anomalies occur between approximately 300 and 100 hPa and between 30°S and 30°N; 2.7a-c). The maximum Hadley circulation strength in the hot period is 55%, 57%, and 85% in the NH compared to the maximum in pre-Industrial, and 73%, 84% and 82% in the SH compared to pre-Industrial, in CanESM5, IPSL-CM6A-LR, and MRI-ESM2-0, respectively. However, the changes to the NH and SH Hadley cells occur at different times. The decrease in SH Hadley cell (and the SH Ferrel cell) strength occurs predominantly between the intermediate and hot period for all models, while the decrease in the NH Hadley cells occurs both before and after the intermediate period (Figure 2.8).

We measure the Hadley cell width as the boundary between the Hadley and Ferrel cells at 500 hPa, which is calculated as the latitude at which the 500 hPa meridional streamfunction crosses zero for the first time between the equator and the pole. Time series of the Hadley cell boundaries in the NH and SH are shown in Figure 2.9, both as a function of year and of global

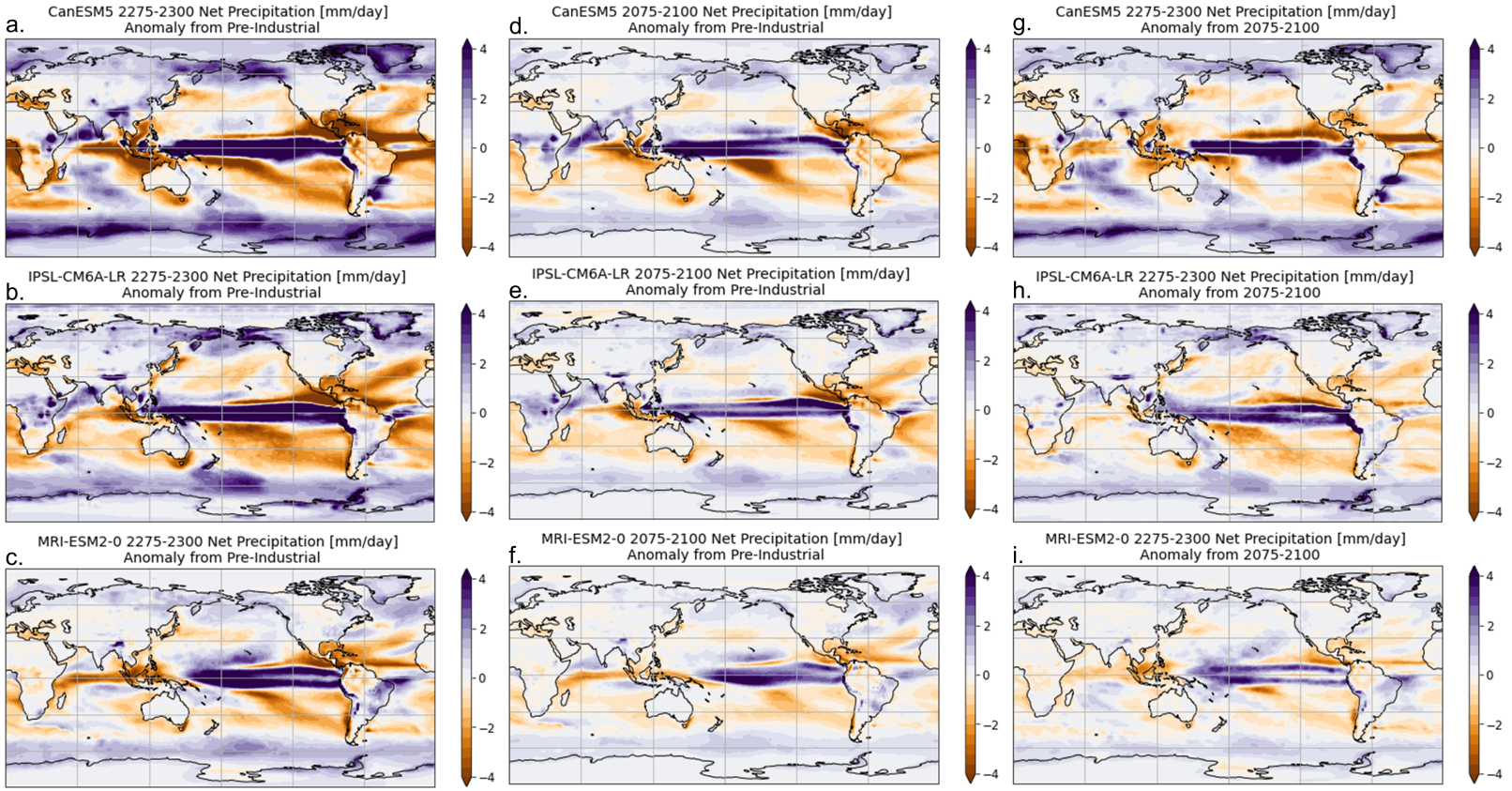

Figure 2.6: Maps of the total Precipitation Anomaly. (a, b, c) The net precipitation (precipitation minus evaporation) anomaly for the hot period from pre-Industrial, (d, e, f) the intermediate period from pre-Industrial, and (g, h, i) the hot period anomaly from intermediate period anomaly. These maps are centered at 180 degrees longitudinally so as to better see the ITCZ.

temperature change. The SH tropical expansion is as large as 5.4 degrees in the CanESM5 model, and is relatively similar as a function of global warming across the three models (Figure 2.9). The NH Hadley Cell extent, on the other hand, shows significant variability across models, and even within a single time series. In CanESM5, the NH Hadley cell extent vacillates between the years 2100 and 2200 (Figure 2.9), before contracting to below pre-Industrial values. From Figure 2.8, it is clear that the zero crossing of the streamfunction in CanESM5 is less well-determined in the hot period, in that there is a range of latitudes near 30 degrees that are close to zero streamfunction. This ambiguity in the Hadley Cell's northern extent in CanESM5 may be a factor in the variability in the NH Hadley Cell boundary after 2100 in Figure 2.9. Other studies have proposed possible mechanisms for an insignificant NH Hadley cell width change, including enhanced equatorial warming reversing seasonal Hadley Cell expansion (Zhou et al., 2019), dynamic processes due to sea ice loss and ocean heat transport (Chemke et al., 2019), or a large change in natural variability (Grise et al., 2019). A more detailed analysis of the large-scale circulation in CanESM5 and other extreme warming scenarios is required to fully understand the mechanisms involved in NH Hadley Cell contraction. IPSL-CM6A-LR, by contrast, exhibits large NH tropical widening, even more than its SH tropical widening (in final extent and in rate of expansion; Tables 2.2-2.3). The larger SH Hadley Cell expansion in CanESM5 and MRI-ESM2-0 (when compared to the NH) is consistent with previous literature (Watt-Meyer et al., 2019).

Time series of the Ferrel Cell boundary in the NH and SH as well as the SH stormtrack latitude are shown in Figure 2.10, both as a function of year and of global temperature change. The boundary between the Ferrel Cell and the Polar Cell also expands with warming in each model (Figure 2.10). In every model there is greater expansion of the NH Ferrel Cell than the NH Hadley cell, which is especially pertinent in CanESM5, where the NH Hadley cell boundary shrinks equatorward, while the NH Ferrel cell boundary expands poleward. The absolute location of the SH Polar-Ferrel boundary, however, is always at higher latitude than the NH boundary; however, both the SH and NH Polar-Ferrel boundaries approach a limit in their poleward extent. Barnes and Hartmann (2012) postulate that there is a poleward limit to cyclonic wave breaking in midlatitude jets and that the SH jets have already reached

	Hadley-Ferrel Boundary	Polar-Ferrel Boundary	ITCZ	Stormtrack
CanESM5	*-0.14 ± 0.08* / -2.0 ± 0.05	1.6 ± 0.1 / -0.71 ± 0.02	-1.6 ± 0.07	3.0 ± 0.16 / -2.6 ± 0.05
IPSL-CM6A-LR	1.7 ± 0.05 / -1.0 ± 0.03	2.9 ± 0.5 / -0.55 ± 0.04	-0.77 ± 0.07	3.1 ± 0.20 / -1.3 ± 0.06
MRI-ESM2-0	0.37 ± 0.05 / -0.90 ± 0.03	0.87 ± 0.19 / -0.38 ± 0.13	-0.87 ± 0.11	*0.16 ± 0.08* / -0.78 ± 0.06

Table 2.2: Latitudinal Changes in the Hadley-Walker Circulation. The Latitudinal change in the Hadley-Ferrel Boundary, Ferrel Cell Boundary, ITCZ, and jetstream location in degrees per century. The first value is for the NH and the second value is for the SH (except for the ITCZ which has one location in the NH). The Hadley-Ferrel and ITCZ locations were found by interpolating for subgrid zeros in the 500hPa streamfunction. The outer Ferrel Cell boundary was found by interpolating for subgrid zeros in the zonally averaged zonal wind. The stormtrack was found by interpolating for subgrid zeros in the numerical derivative of surface zonal wind with respect to latitude. Values which do not have a p-value less than 0.05 are *italicized*. All of the regressions are over on yearly averages.

this extent. This is consistent with the lesser poleward motion we see in the SH Polar-Ferrel boundary compared to that in the NH.The bottom row of Figure 2.7d-f shows the zonally averaged zonal wind anomalies. The jet stream, defined by the maximum in zonal wind, rises along with the tropopause, decreasing in pressure by 50 to 100 hPa, with a larger rise in the models that warm more. Changes in zonal wind below the tropopause are on the order of several m/s, representing large fractional changes in wind strength especially near the surface. The large poleward shift of the SH jet streams are consistent with the time series of the SH stormtrack, measured as the maximum surface zonal wind, which shows a decrease in latitude between approximately 3.0 and 7.5°(Figure 2.10).

All three models produce an equatorward shift of the ITCZ in the warm period. Based on surface wind convergence in the piControl runs, the ITCZ is at 2.8-4.5°N. By 2300, the convergence shifts to approximately 1.2-2.6°N. The vast majority of the equatorward shift of the ITCZ occurs after 2100, especially in CanESM5 where the ITCZ shifts more than 3 degrees northward by 2100 and 4° southward after. The changes in ITCZ location are consistent with the changes in tropical precipitation seen in Figure 2.6 and described above.

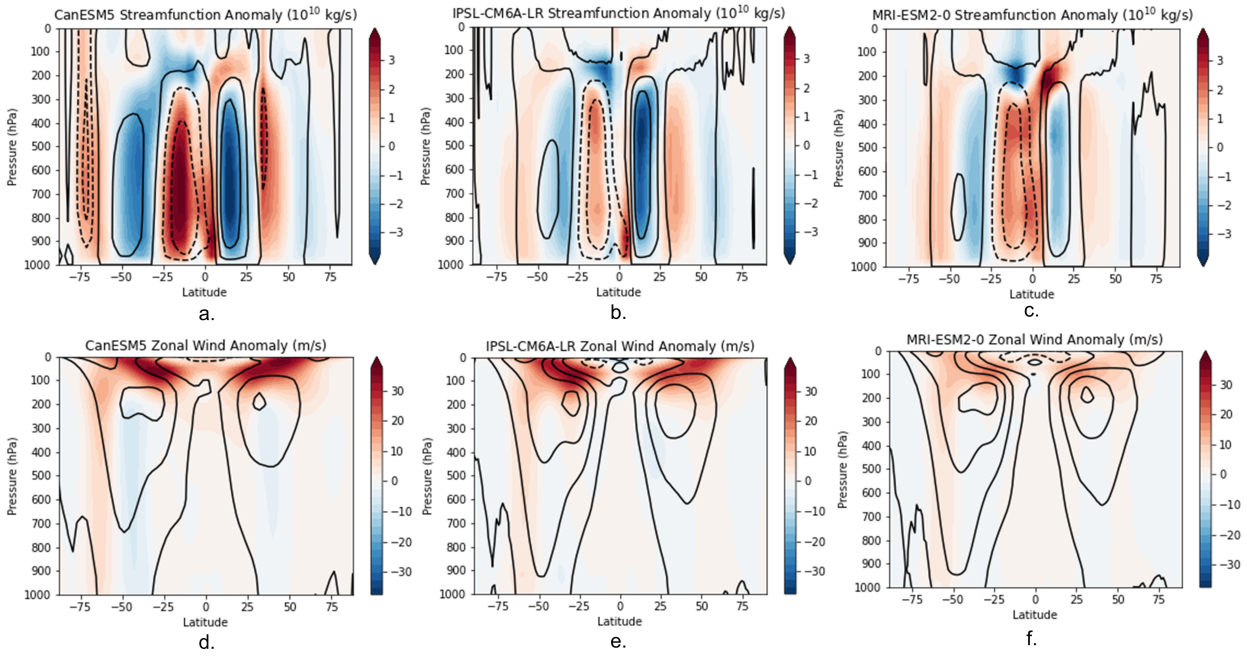

Figure 2.7: Streamfunction and the Zonal Wind Anomaly The color contours represent (a, b, c) the streamfunction anomaly (10^{10} kg/s) and (d, e, f) the zonal wind anomaly (m/s) of CanESM5, IPSL-CM6A-LR, and MRI-ESM2-0. The black contours represent the pre-Industrial. The pre-Industrial streamfunction ranges from -9 to 9x10^{10} kg/s with a contour interval of 3x10^{10} kg/s. The pre-Industrial zonal wind ranges from 0 to 30 m/s with a contour interval of 6 m/s.

	Hadley-Ferrel Boundary	Polar-Ferrel Boundary	ITCZ	Stormtrack
CanESM5	-0.01 ± 0.01 / -0.32 ± 0.01	0.27 ± 0.02 / -0.12 ± 0.003	-0.23 ± 0.01	0.50 ± 0.02 / -0.41 ± 0.01
IPSL-CM6A-LR	0.34 ± 0.01 / -0.20 ± 0.01	0.58 ± 0.03 / -0.11 ± 0.01	-0.14 ± 0.01	0.63 ± 0.04 / -0.26 ± 0.01
MRI-ESM2-0	0.12 ± 0.01 / -0.27 ± 0.01	0.29 ± 0.06 / -0.11 ± 0.04	-0.24 ± 0.04	0.05 ± 0.02 / -0.23 ± 0.02

Table 2.3: Latitudinal Changes in the Hadley-Walker Circulation against Warming. The Latitudinal change in the Hadley-Ferrel Boundary, Ferrel Cell Boundary, ITCZ, and jet-stream location against global mean temperature anomaly (degrees/K). The first value is for the NH and the second value is for the SH (except for the ITCZ which has one location in the NH). See table 2 for methods. All values included have a p-value of less than 0.05. All of the regressions are over yearly averages.

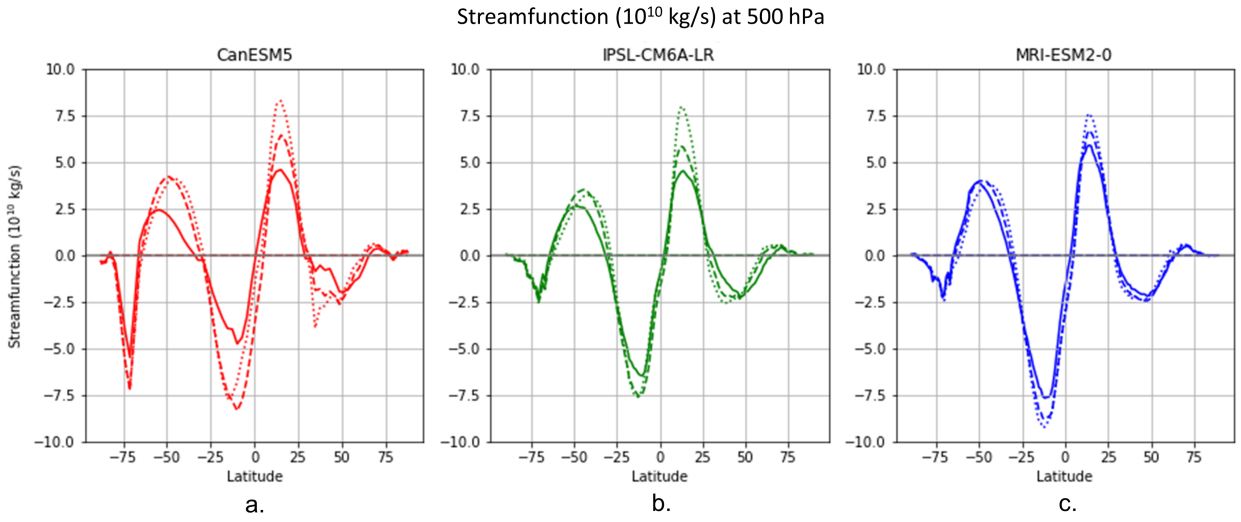

Figure 2.8: Time Evolution of the 500hPa Streamfunction. The streamfunction (10^{10} kg/s) at 500hPa for CanESM5 (a, red), IPSL-CM6A (b, green) and MRI-ESM2-0 (c, blue). The solid lines represent the hot period, the dashed lines represent the intermediate period, and the dotted lines represent the pre-Industrial period.

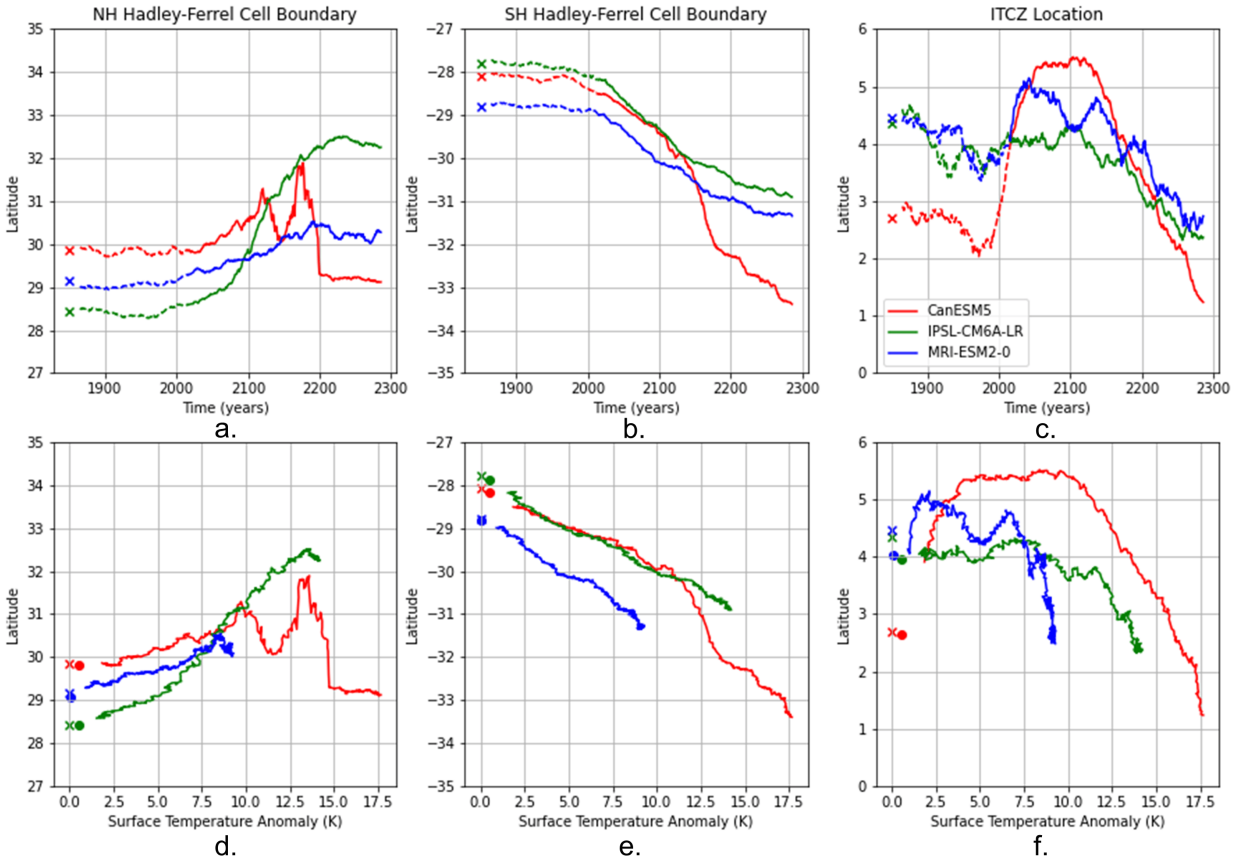

Figure 2.9: Time Evolution of the Hadley-Ferrel boundaries and ITCZ locations. (a, b, c) The 30-year running mean NH and SH Hadley-Ferrel Boundary location and ITCZ location versus time, and (d, e, f) global mean temperature anomaly from 1850 to 2300. The time and zonally averaged pre-Industrial values are denoted by an X. In the time series figures (top row), the historical data (1850-2015) are denoted by the dashed lines, while the SSP-Ext runs (2015-2300) are denoted by the solid lines. In the temperature anomaly figures (bottom row), the time-mean historical data is denoted by a circle.

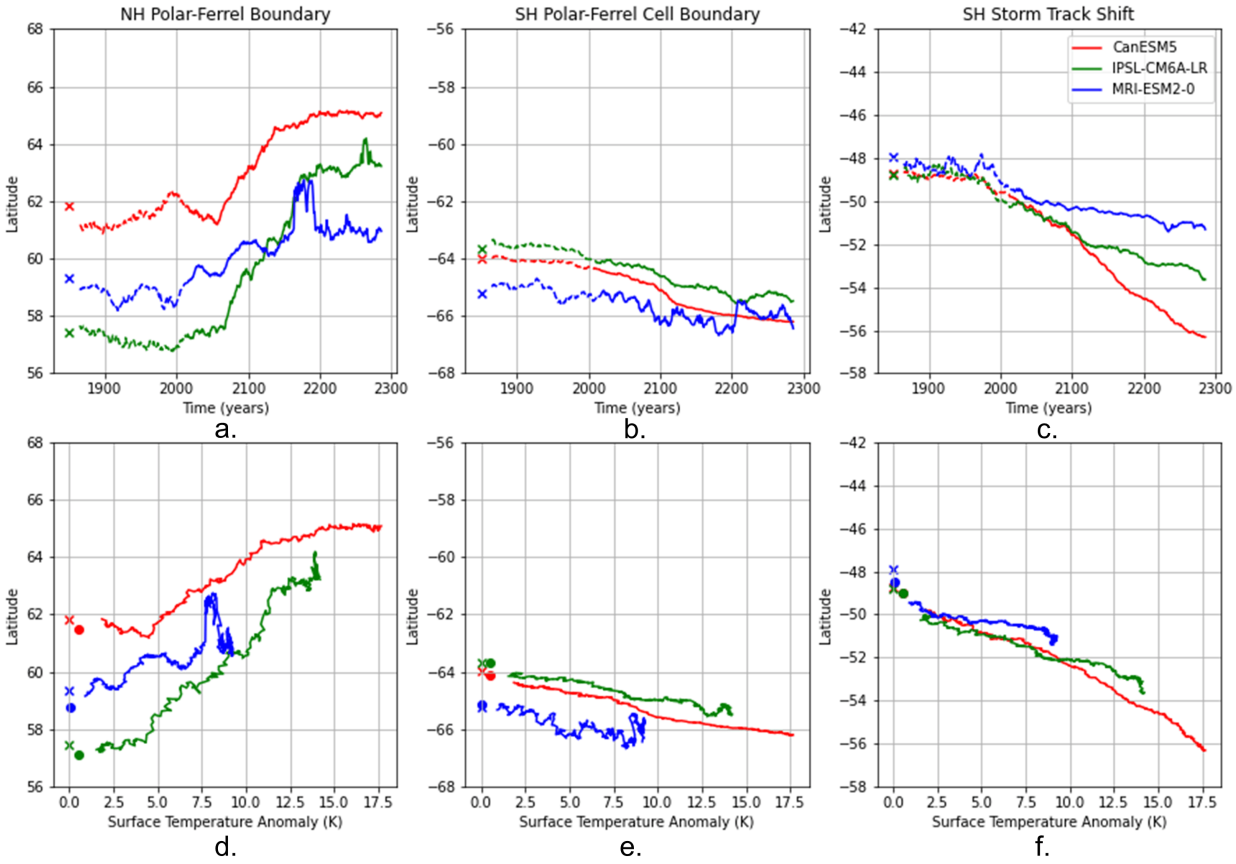

Figure 2.10: Time Evolution of the Polar-Ferrel boundaries and SH Stormtrack locations. The 30-year running mean of (a, d) the NH Polar-Ferrel Cell boundary, (b, e) the SH Polar-Ferrel Cell boundary (c, f) and the SH storm track location versus time (top row), and versus the global mean temperature anomaly (bottom row) from 1850 to 2300 . The time and zonally averaged pre-Industrial values are denoted by an X. In the time series figures (top row), the historical data (1850-2015) are denoted by the dashed lines, while the SSP-Ext runs (2015-2300) are denoted by the solid lines. In the temperature anomaly figures (bottom row), the time and time-mean historical data is denoted by a circle. The piControl stormtrack latitudes for CanESM5, IPSL-CM6A-LR, and MRI-ESM2-0 are 48.7S, 48.8S, and 47.9S respectively.

2.3.2 Poleward Energy Transport

a. Latent Energy, DSE, and MSE Transport

The northward transport of latent energy is plotted for both pre-Industrial control and the end of SSP5-8.5ext in Figure 2.11a. Since the moisture content increases by such a large amount with warming, it is not surprising that the latent energy transport also amplifies quite a bit. In the SH extratropics, for instance, the maximum southward flux increases from less than 3 PW to over 4 PW in each model, with larger increases in models with more temperature change.

The CanESM5 model has a 3 PW increase in southward latent energy transport at 55° S (Figure 2.12a). In the NH extratropics, the maximum northward latent heat transport increases by 1-1.8 PW, depending on the model. At 45°N, poleward of its initial extratropical maximum, the northward latent energy flux in the CanESM5 model increases by 2 PW. In both the NH and SH extratropics, the latent heat transport increases more on the poleward side of the maximum than the equatorward side. The latitude of maximum poleward flux shifts poleward in both hemispheres in each model, and the fractional increase in flux reaches a factor of 3-4 in regions poleward of the flux maximum, as compared with 40-100% increase of the maximum value itself. These moisture transport changes are consistent with the large increases in precipitation at high latitudes in each model.

The equatorward latent energy transport within the tropics in the pre-Industrial control is driven by the Hadley circulation. Despite large increases in humidity in the deep tropics, the equatorward transport in the NH tropics does not increase much, meaning the decrease in Hadley cell strength (Figure 2.7) nearly compensates. The SH tropical transport increases more, especially in the IPSL-CM6A-LR model, but the reduction in Hadley circulation strength also reduces the magnitude of the equatorward moisture flux change.

The northward transport of MSE is plotted in Figure 2.11b, and its change in Figure 2.12b. The structure of the transport is similar in pre-Industrial and warmed climate, with poleward transport in both hemispheres. The poleward transport increases in all models, but with varying magnitudes. The increase in poleward flux is especially large in CanESM5 (maximum change of 1.7 PW), and small in MRI-ESM2-0 (maximum change 0.6 PW). IPSL-

CM6A-LR shows the most asymmetric increase between NH and SH, with an average of twice the increase of poleward MSE flux in the SH as in the NH. The average fractional increase in poleward MSE transport in the SH extratropics is 35% in CanESM5, 25% in IPSL-CM6A, and 10% in MRI-ESM2-0.

In each model, there is a part of the high northern latitudes where the poleward MSE transport decreases. This feature is most prominent in MRI-ESM2-0. Hwang et al. (2011) argued that models with lesser flux increase into the Arctic were more likely to have stronger polar amplification, due to a diffusive response to high latitude warming causing a diminished energy flux into the Arctic. We return to this Arctic feature later in the paper.

In the NH, the CanESM5 model experiences a large equatorward shift of the maximum MSE flux, of approximately 10 degrees latitude, while the other two models keep the same latitude of maximum northward flux. The maximum in the SH in the CanESM5 model also shifts equatorward by a slightly smaller amount, while the MRI-ESM2-0 and IPSL-CM6A-LR models have a slight poleward shift. The equatorward shifts in maximum MSE flux in the CanESM5 indicates especially large increases of MSE flux in the subtropics. We provide a more detailed explanation for the unique behavior of the CanESM5 model's MSE flux maxima in the following subsections, based on the tropical cloud radiative effect changes.

The northward transport of DSE is plotted in Figure 2.11c and is the difference between Figures 2.11b and 2.11a. The large decrease in poleward transport in the extratropics and increase in poleward transport in the tropics is clear in all models. These oppose the latent energy transport, and thus create a smaller change in MSE transport than in either DSE or latent energy flux individually. Opposition of the latent energy transport by DSE transport occurs at nearly every latitude in each model, and the changes are plotted together in Figure 2.12a to facilitate comparison. The most prominent exception is in the subtropics (especially visible in the CanESM5 model), where the poleward flux of both the DSE and latent energy increases in both hemispheres. The CanESM5 model has a particularly large decrease in southward DSE transport in the SH extratropics, where it decreases by over 50% in some places. In all models, the poleward DSE flux decreases particularly strongly in the regions between 35 and 60°. The resulting DSE flux exhibits a poleward shift in the maximum

extratropical flux, or the establishment of a new local maximum at high latitudes.

We next consider the compensation percentage, defined as:

$$C = \frac{-\Delta F_{DSE}}{\Delta F_{Latent}} \times 100\% \quad (2.2)$$

where C is the compensation percentage, F_{DSE} is the dry static energy flux, and F_{latent} is the latent heat flux. The compensation percentage C represents the effectiveness of the DSE transport in compensating for the increased latent energy transport, with 100% meaning there is no change in the MSE flux. Compensation percentages within the tropics are larger than 100%, reflecting the fact that the DSE transport increases faster than the latent energy transport. In the Northern Hemisphere between 40 and 60 degrees, compensation percentages are around 75% for each model. In the Southern Hemisphere, percentages are much lower: 65% in MRI-ESM2-0, and 50% in IPSL-CM6A-LR and CanESM5.

How is the compensation percentage in the CanESM5 model in the SH so small, despite the large change in DSE flux? Examining the moisture flux change, one can see that the poleward latent energy transport increases by up to 3 PW, a number that is larger than the poleward transport of DSE in the pre-Industrial period. Thus 100% compensation is impossible within the SH midlatitudes, assuming the DSE transport remains poleward. The picture that emerges is of a SH storm track in which the latent energy transport increases substantially, working off of large humidity gradients (Figures 2.3-2.4) despite decreases in DSE transport, driven by some combination of weaker temperature gradients and weaker eddies. We examine these factors later in the paper.

b. Ocean Heat Transport

The ocean component of the anomalous northward energy transport is plotted in Figure 2.12b. This is calculated by integrating the anomalous surface flux after subtracting out the global mean, so includes the effect of both changes in ocean heat transport and differential storage. Since no model is in energy balance by 2300, the differential ocean heat storage is non-negligible. When heat storage is occurring more at the higher latitudes, e.g., in the Southern Ocean, there is an anomalous equatorward energy transport in this metric.

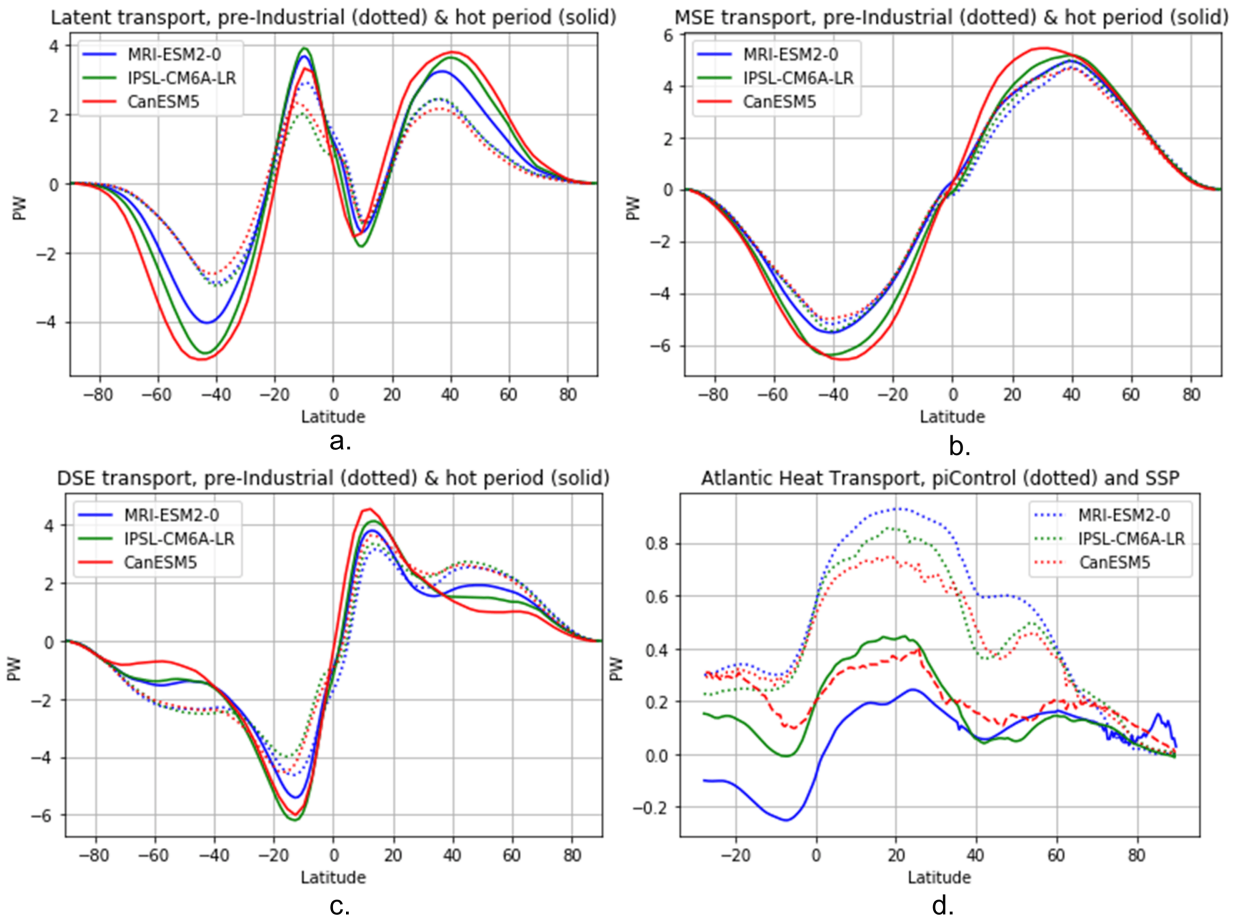

Figure 2.11: Northward Energy Transport. Northward transport of energy from (a) latent, (b) moist static energy, and (c) dry static energy and (d) the Atlantic Ocean. Pre-Industrial transports are dotted and hot period transports are solid. The CanESM5 ocean heat transport data for the hot period is averaged between 2156 and 2180, due to data availability, so it is denoted with a dashed line to indicate the different averaging period.

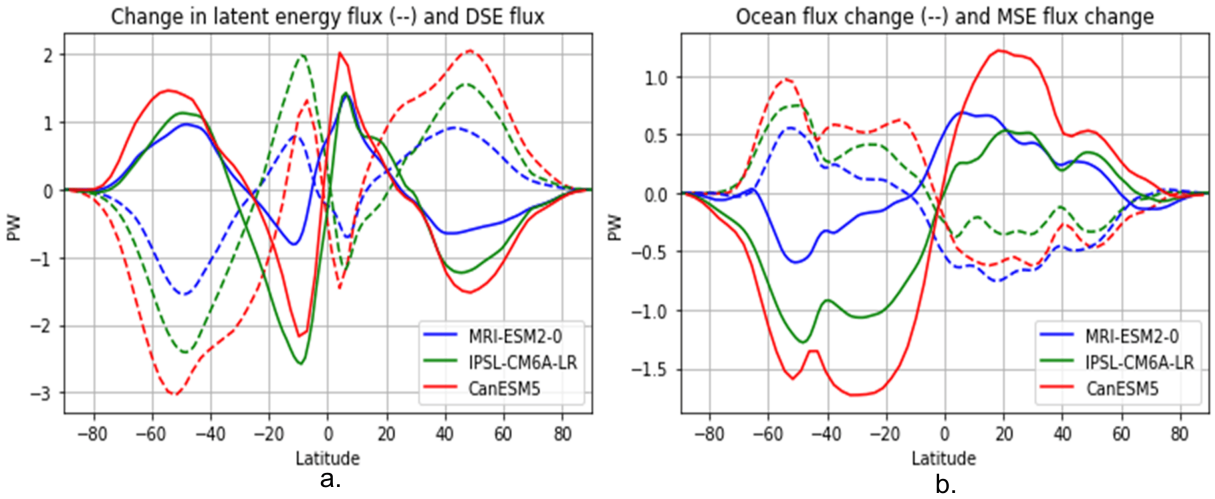

Figure 2.12: Northward Energy Transport Anomaly. The change in northward transport of energy (hot period minus pre-Industrial) from (a) latent (dashed) and DSE (solid), as well as from (b) ocean transport (dashed) and MSE (solid).

In all three models, the ocean component opposes the MSE transport change. The change in ocean transport is especially close to being equal and opposite to the MSE transport change in the MRI-ESM2-0 model on a latitude-by-latitude basis, while in the CanESM5 model, the ocean transport averages around half of the poleward MSE transport change. The anomalous cross-equatorial transport is strongly negative in the MRI-ESM2-0 model, with a value of -0.5 PW, and is approximately half this value in other two models. An examination of the anomalous northward transport of energy in the Atlantic Ocean, plotted in the pre-Industrial and warmed climate in Figure 2.11d, shows that the cross-equatorial anomalies in Figure 2.12b are primarily due to reductions in strength of the AMOC. In Figure 2.11d, the x-axis only goes as far south as 30°S, due to the end of the ocean basin. CanESM5 only outputs data on ocean heat transport to the year 2180, so in that model we use an average of years 2156 to 2180 to represent the warmed period. In all models, the pre-Industrial ocean circulation transports a large amount of heat northward across the equator, with a similar value of 0.55-0.6 PW, while north of the equator there is substantial model spread in the poleward ocean heat flux. The MRI-ESM2-0 model has 50% larger flux in the pre-Industrial

period than the other two models at 45°N.

Warming causes a large decrease in the northward transport of energy in the Atlantic in all three models. AMOC damping is a result of large buoyancy fluxes that help to inhibit deep overturning circulation (Putrasahan et al., 2019). While buoyancy changes are primarily driven by surface fluxes (Kostov et al., 2019), this buoyancy flux can also come in the form of melting sea ice, as melt water can cause abrupt changes in the salinity of surface waters (Weijer et al., 2012; Li et al., 2021). The MRI-ESM2-0 model has a slightly negative Atlantic cross-equatorial transport in the warmed climate, indicating a complete collapse of the AMOC; this collapse is consistent with the model's behavior under abrupt-doubling and -quadrupling experiments (Poletti et al., 2024b). The AMOC collapse in MRI-ESM2-0 is consistent with the warming pattern in the intermediate period which shows decreased warming south of Greenland, also called the North Atlantic Warming Hole (NAWH; Figure 2.2i) (Zhang et al., 2010; Jackson et al., 2015). The AMOC collapse is likely also the primary cause of the southward ITCZ shift in the Atlantic identified in Figure 2.6i, as the reduction in oceanic heat transport must be met by an northward transport of MSE, which contributes to the convergence of winds occurring farther south (Zhang and Delworth, 2005; Yu and Pritchard, 2019). The slowdown in circulation and the accompanying ocean heat flux decrease can help explain the equatorward shift in the ITCZ shown in each model.

Another consistent feature in the ocean heat flux change in Figure 2.12 is the decrease in strength of the ocean heat divergence within the equatorial region. The subtropical cells are wind-driven, and along with the decrease in strength of the surface winds throughout the tropics, visible both in the change in zonal winds in Figure 2.7 and in surface wind change plots as a function of latitude and longitude (not shown), the upwelling and overturning circulation must weaken. In turn, the MSE fluxes increase in each model to compensate for the decrease in ocean heat transport.

c. Cloud Radiative Effect

Clouds can have large contributions to the local and global energy budget, and hence are useful in understanding how energy moves in an extremely warmed climate. The radiative

impact of clouds is presented as longwave and shortwave components as well as the net radiative effect in Figure 2.13. The longwave CRE is simply the difference between the longwave top of atmosphere radiation in clear sky and in all sky conditions. The SW cloud term is found using the Approximate Partial Radiative Perturbation (APRP) method to decompose the shortwave radiation budget into its contributing mechanisms (in this case clouds) (Taylor et al., 2007). APRP allows us to remove surface effects (such as ice melt) to the shortwave budget from the shortwave cloud effect (Zelinka et al., 2014). The net radiative anomaly is defined as the sum of the longwave CRE and the shortwave APRP cloud effect. Figure 2.13 shows fields of each metric for cloud radiation as the hot period anomalies from the pre-Industrial average values.The two models have global mean longwave CREs of -4.9 and -2.6 W/m^2 respectively. The longwave CRE in CanESM5 behaves very differently, and accounts for a total increase in downward longwave radiation. The average longwave CRE anomaly in CanESM5 is 7.0 W/m^2.

Although the global mean values differ, the broad patterns of the changes in longwave CRE are fairly consistent among models, with decreases over regions of marine stratocumulus and strong increases in the tropics. The much larger region of positive longwave CRE anomaly around the equator in CanESM5 is in part due to the large increase in tropical temperature, which increases the depth of deep convective clouds. This is an expected positive feedback to global warming that is well supported by theory, and is on the cusp of being constrained observationally, with rising high clouds currently being observable in the Northern Hemisphere (Hartmann and Larson, 2002; Zelinka and Hartmann, 2010; Aerenson et al., 2022). Upward movement of clouds is also associated with increases in tropopause height, visible in both the streamfunction and zonal wind panels (Figure 2.7). The particularly large meridional extent of the positive longwave CRE region in CanESM5 suggests an expansion of high clouds throughout the poleward branches of the Hadley circulation. The lack of shortwave cloud cooling in that region points to a potential role of cirrus clouds, which have a large impact on longwave radiation, but are optically thin to solar wavelengths (Lynch, 1996), but we are limited by data availability in our ability to understand this feature.

In the shortwave cloud term, there is increased radiation absorbed over much of the sub-

tropics, indicating a reduction of stratocumulus and cumulus clouds, and decreased radiation over parts of the deep tropics and high latitudes. Without cloud fields at varying heights and optical depths, such as is provided by the COSP cloud simulator package (Bodas-Salcedo et al., 2011), we cannot determine what cloud types are contributing to these radiative anomalies.

The differences in the longwave and shortwave cloud radiation result in global net radiative effects of 9.5 W/m^2 for CanESM5, 0.1 W/m^2 for IPSL-CM6A-LR, and MRI-ESM2-0 has a net radiative effect that is balanced to order one thousandth of a W/m^2. Cloud feedbacks are considered the largest source of variability in climate sensitivity (Dufresne and Bony, 2008; Held and Soden, 2006; Sherwood et al., 2020; Zelinka et al., 2020), and Virgin et al. (2021) found that equatorial low cloud and non-low cloud reduction is the primary cause of the high climate sensitivity of CanESM5 compared with the previous generation of that model. The cloud feedbacks are likely an important cause of the particularly large MSE transport increase away from the equator in the CanESM5 model, with MSE transport away from the cloud-induced heating. We return to this feature in the Discussion section.

d. Eddies, Lapse Rate, and Diffusivity

We next examine factors that characterize and affect extratropical eddies to better understand the energy transports presented in Section 2.3.2.a. The average standard deviation of daily sea-level pressure is used to estimate the eddy intensity in each model. The standard deviation is calculated from daily fields of sea-level pressure, where the seasonal cycle is removed and the pre-Industrial mean is subtracted out. Standard deviation of sea-level pressure calculated in this way indicates the strength of synoptic scale systems and eddies.

The eddy strength is shown in Figure 2.14 as an average over the last 25 years of the simulation and a percent change compared with pre-Industrial. At the end of the run each model shows a large area of low eddy intensity in the tropics, with high intensity in the midlatitudes and polar regions. There is some positive change in eddy strength in the tropics, but since the pre-Industrial value in those regions is near zero, the large fractional changes are not indicative of large absolute changes. All three models exhibit a weakening

of midlatitude surface eddies, each model showing the largest fractional change off the west coast of continents. CanESM5 has the strongest reduction, with many midlatitude regions experiencing a decrease of more than 40%. IPSL-CM6A-LR has fewer regions that decrease by more than 40% and follows a very similar spatial pattern to CanESM5. MRI-ESM2-0 has a much weaker response, especially in the Northern Hemisphere, where very few regions decrease by more than 10%.

One potential cause of the widespread eddy weakening, the lapse rate, is shown in Figure 2.15. The lapse rate in the hot period and its anomaly from pre-Industrial are plotted, with lapse rate defined as the difference between the temperature at 300 hPa and the surface divided by the difference in geopotential height at 300 hPa and surface. The change in lapse rate in all models is dominated by an increase in the poles, and a decrease in the tropics and subtropics. The lapse rate in the tropics/subtropics decreases due to the decrease in the saturated adiabatic lapse rate at higher temperatures and humidity (Wetherald and Manabe, 1988). Polar amplification of surface warming, on the other hand, is surface-trapped, and causes an increase in the lapse rate (Pithan and Mauritsen, 2014).

CanESM5 has the largest global-averaged reduction of lapse rate, with a change of -1.24 K/km, then IPSL-CM6A-LR has a change of -1.17 K/km, MRI-ESM2-0 has the smallest net change of -0.66 K/km. Throughout the subtropics and midlatitudes, the models show a decrease in lapse rate (as seen in CMIP3 models in Frierson (2006)), with an especially prominent decrease in the CanESM5 model. When the lapse rate decreases, the static stability of the atmosphere increases, so that the eddy kinetic energy is lower, resulting in a decrease in surface eddies (Yuval and Kaspi, 2020). Even though increased moisture content can offset this (and indeed is the original cause of the lapse rate change), the dry static stability is thought to be most relevant because baroclinic instability always has some unsaturated component (Emanuel et al., 1987; Zurita-Gotor, 2006). It is also possible for the static stability decrease in high latitudes to cause an increase in eddy intensity over the poles.

To investigate how the energy transport is influenced by changes in eddy intensity, we first examine the surface MSE in Figure 2.16. Since the surface geopotential is the same in

both time periods, MSE is equal to

$$MSE = C_p \Delta T + L_v q \quad (2.3)$$

Where C_p is the specific heat under constant pressure, T is temperature, L_v is the latent heat of vaporization, and q is the specific humidity. The MSE increases substantially due to temperature and humidity increases. The increase is largest in the tropics in each model due to the increase in humidity. This results in an increase in the equator-to-pole MSE difference in each model. The increase in MSE gradient likely explains some of the tendency of the flux to increase, but does the weakening of eddies also play a role?

The surface diffusivity, calculated as the vertically integrated MSE flux divided by the meridional gradient in MSE is plotted in Figure 2.17 to answer this question. Although both the flux and the gradient of MSE increase with warming, the flux increases more in the SH in all models, leading to a decrease in the diffusivity. In the NH, changes in diffusivity are smaller, and not consistent among the three models. The CanESM5 and IPSL-CM6A-LR models each show a small decrease in diffusivity when averaged between 25 and 50°N, while MRI-ESM2-0 shows approximately zero change over the same latitude band. This is consistent with the NH eddy changes in the MRI-ESM2-0, which show slight increases in that model as compared to the pre-Industrial level.

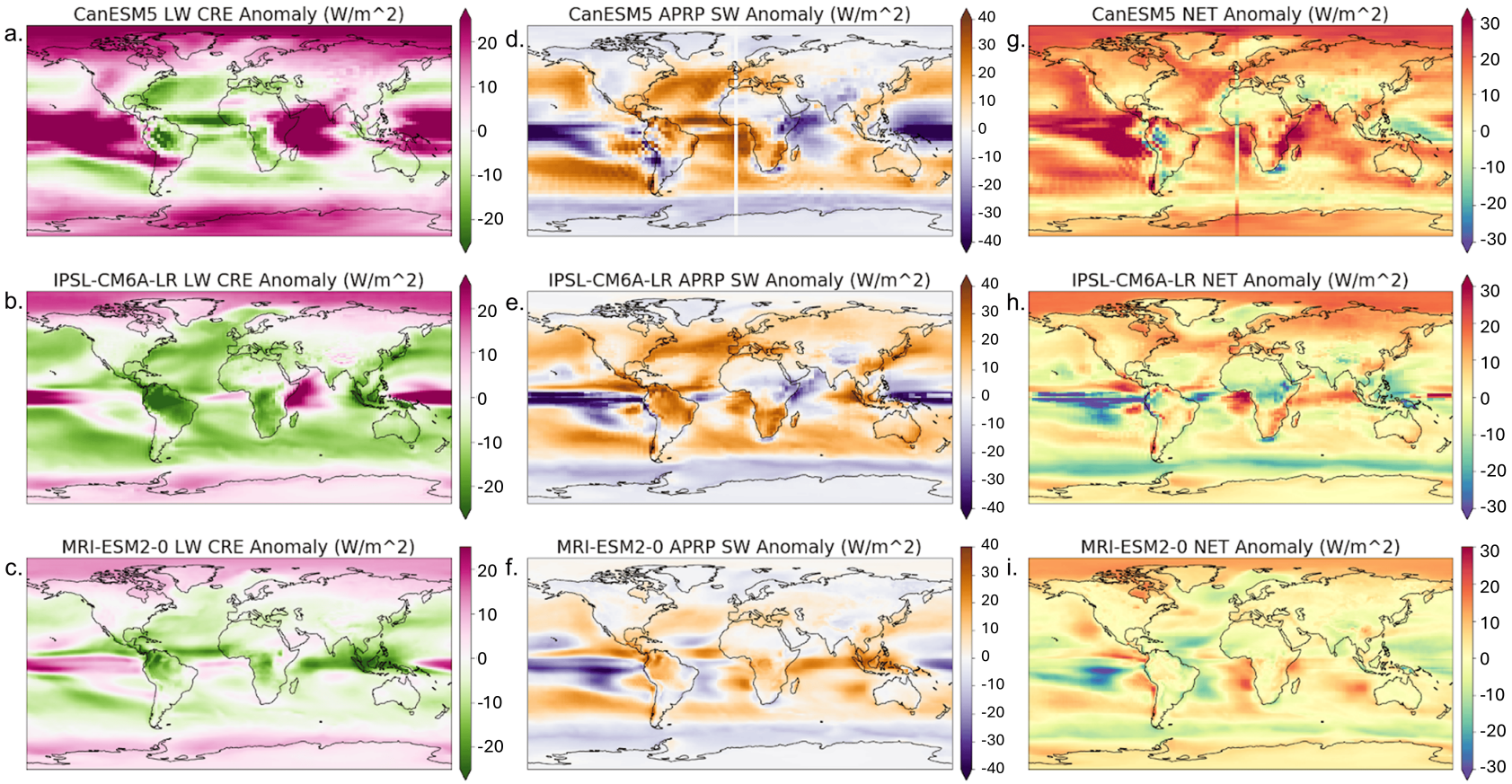

Figure 2.13: Maps of the Cloud Radiative Effect Anomaly The anomalies in (a, b, c) longwave cloud radiative effect, (d, e, f) shortwave cloud radiative effect as calculated using APRP, and (g, h, i) the sum of the longwave and shortwave cloud radiative effects.

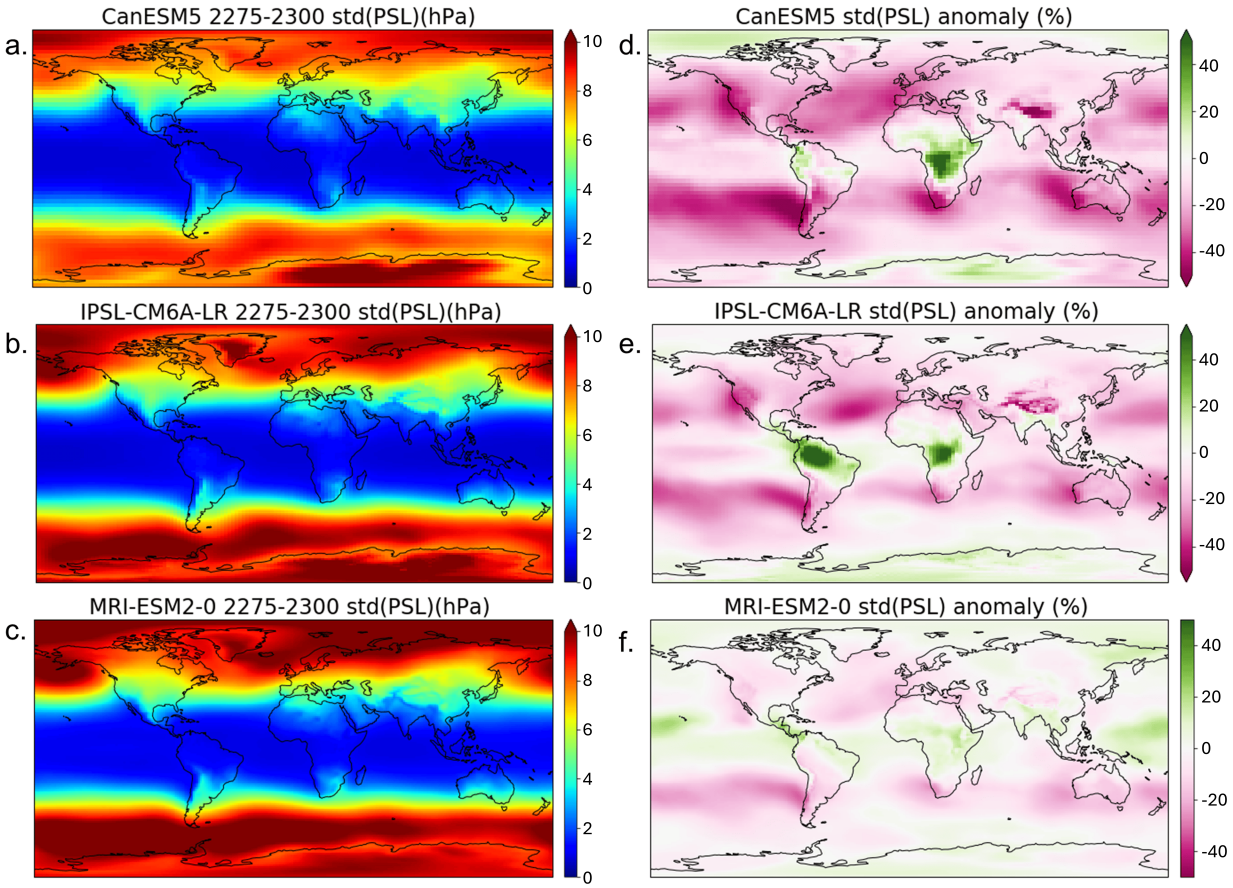

Figure 2.14: Maps of Varibility in Sea Level Pressure. (a, b, c) The standard deviation of daily sea level pressure fields (hPa) in the hot period, and (d, e, f) the percentage change since pre-Industrial.

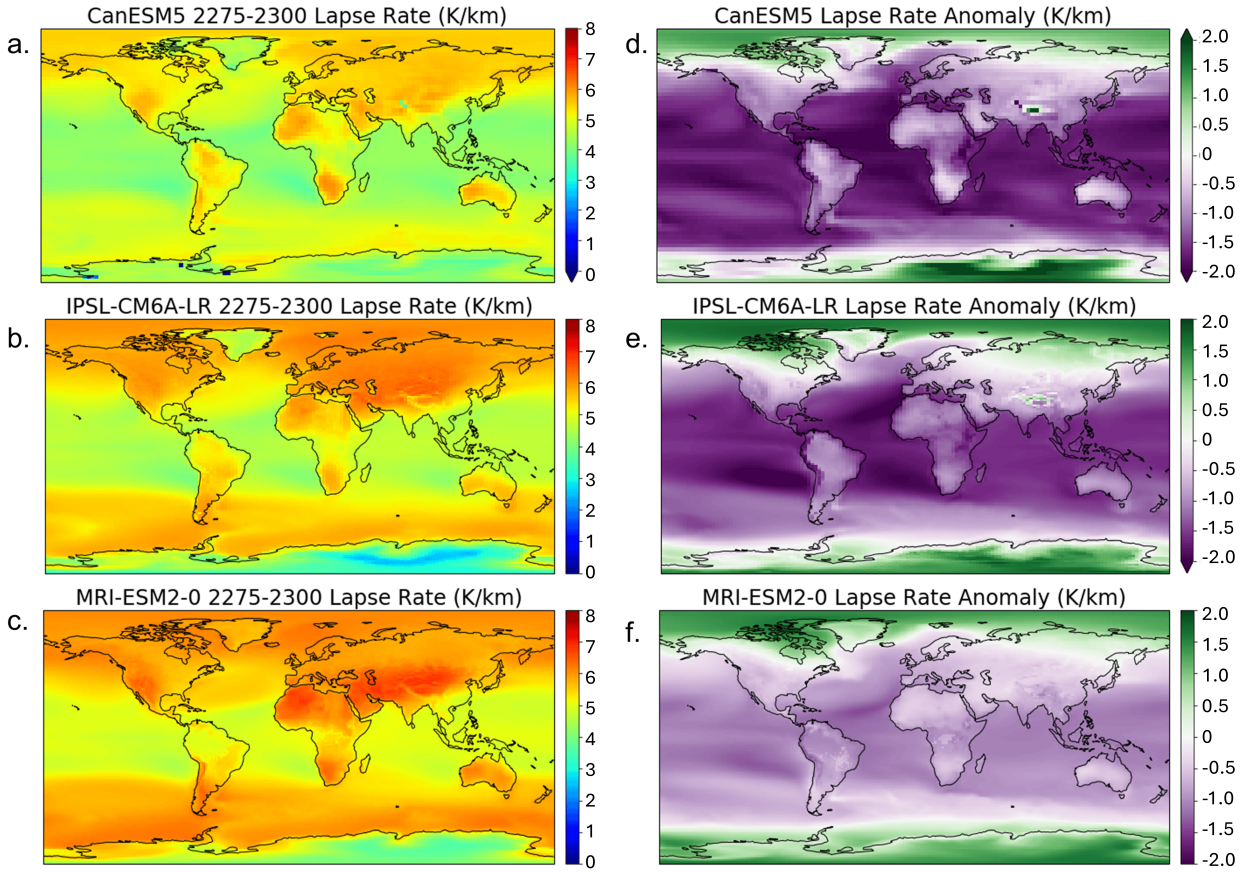

Figure 2.15: Maps of the Lapse Rate. The lapse rate in (a, b, c) the hot period, and (e, e, f) the change since pre-Industrial, calculated as the difference between the temperature at the surface and 300 hPa, divided by the difference in geopotential height at the same levels.

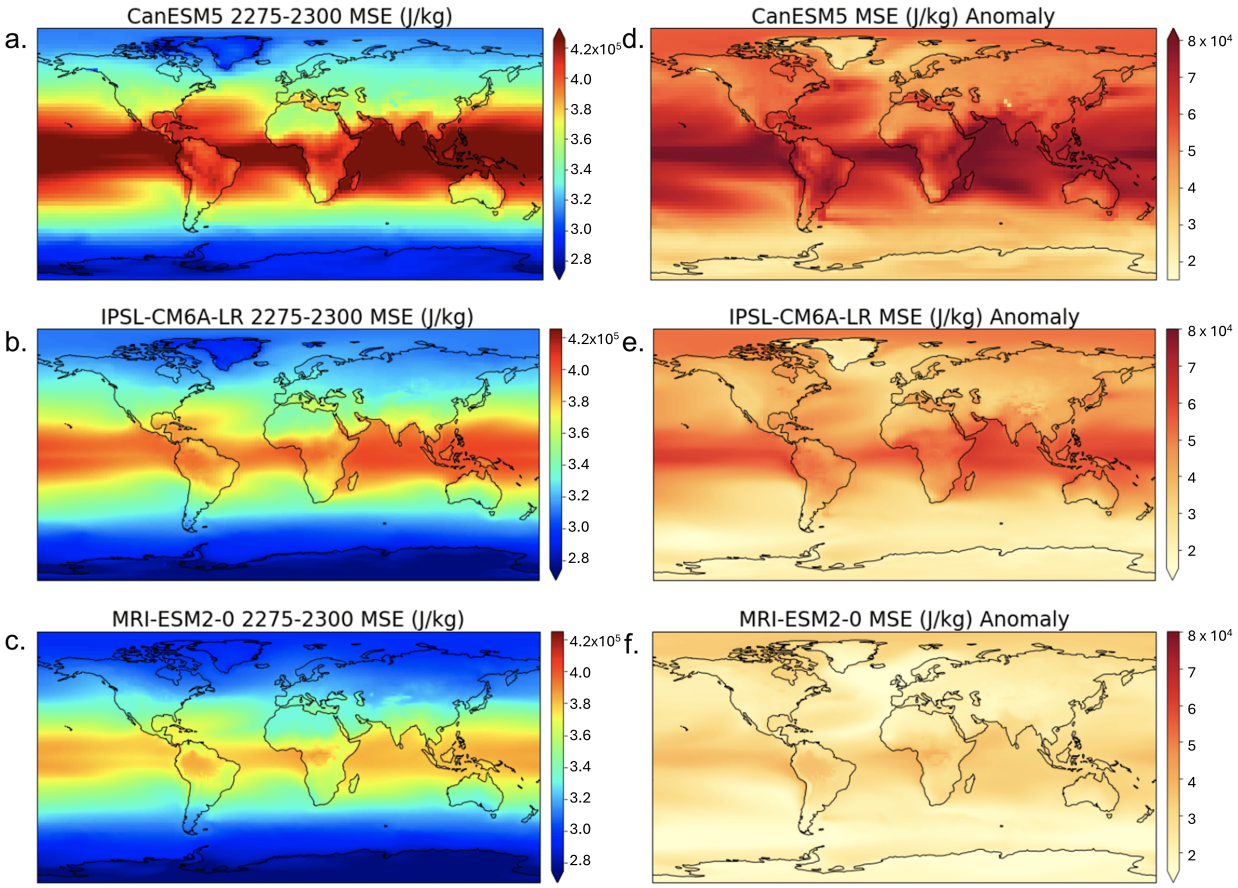

Figure 2.16: Maps of Moist Static Energy. The surface moist static energy (J/kg) in (a, b, c) the hot period, and (d, e, f) the changes since pre-Industrial.

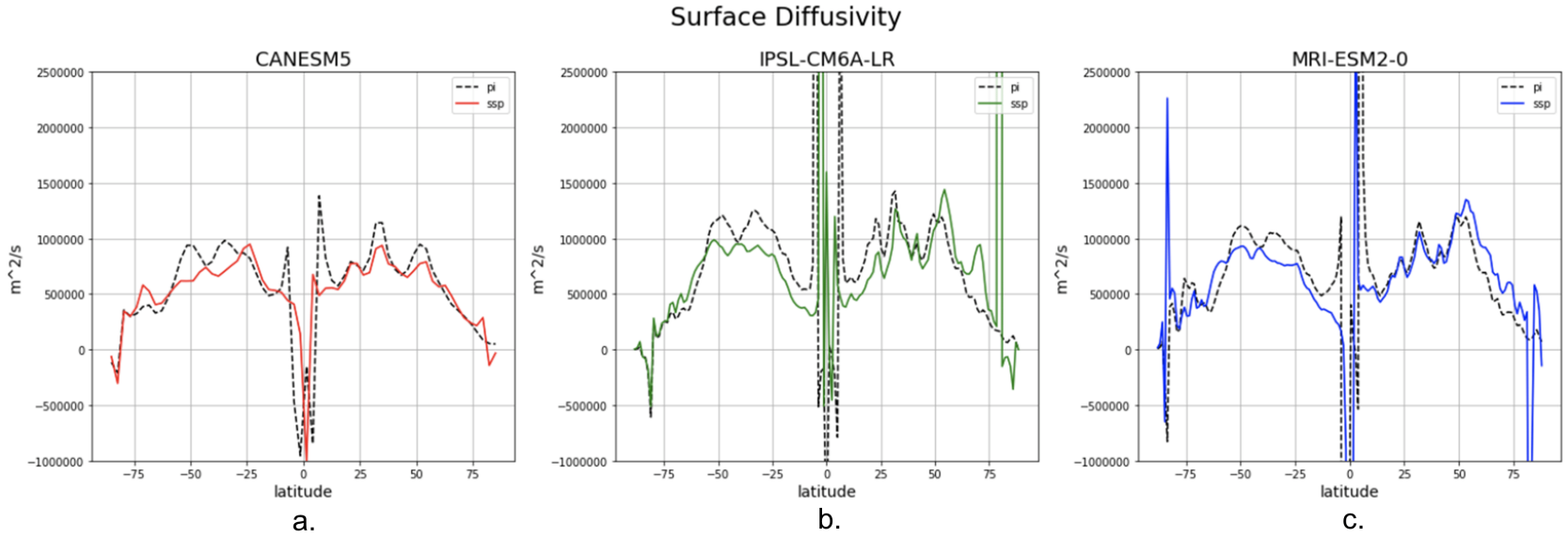

Figure 2.17: The Zonal Diffusivity of Moist Static Energy. The diffusivity of moist static energy (m^2/s), defined as the vertically integrated MSE flux divided by the surface MSE gradient at each latitude for pre-Industrial (dashed) and the hot period (solid) for (a) CanESM5, (b) IPSL-CM6A-LR, and (c) MRI-ESM2-0.

2.4 Discussion & Conclusions

Global warming extension scenarios run for several centuries into the future provide a unique laboratory for analysis of climate dynamics in a much warmer world. Despite the lack of certainty about emissions into the distant future and the unlikeliness of this particular pathway, these simulations provide an interesting opportunity for the study of climate changes of the future. Even if these climates are never realized, the large amplitude changes can help with understanding of smaller perturbations. For instance, many of the climate changes that have been observed in the recent past and are expected in the next 50 years are seen in a more extreme manner in these simulations. These include increases in moisture content and transport, poleward shifts of the storm tracks and Hadley cell boundaries, weakening of tropical surface winds, and reductions in the AMOC strength. Global mean temperature increase for these simulations range from 9.3 K to 17.5K, with moisture content increasing by at least a factor of 1.5 in each model, and with moisture in CanESM5 increasing by more than a factor of 2. While many of the changes we observe are proportional to the global mean temperature, some are not, such as the weakening of the AMOC.

The climate metrics shown can be used together to understand the physical mechanisms responsible for many of the dynamical changes. The massive increases in latent energy transport are balanced by corresponding decreases in DSE transport, although the compensation is imperfect. The increase in moisture flux is so large in some cases (e.g., the Southern Hemisphere in CanESM5) that perfect compensation is impossible if the DSE transport is to remain poleward. In all models, eddy intensity decreases substantially, likely due to the decreases in lapse rate and decreases in meridional temperature gradient. The eddy intensity decrease is associated with a decrease in MSE diffusivity. Ocean heat transports and cloud radiative effects each influence MSE fluxes and can help understand the difference in energy transports among models.

The CanESM5 model has the largest warming, and thus stands out in many of the diagnostics. In terms of energy transports, the difference between CanESM5 and the other two models is most prominent around the equator. The sharp increase in poleward MSE

flux in the tropics of CanESM5, described Section 3a, is likely in part due to a transport of MSE away from the large cloud radiative heating in the deep tropics. The Hadley cell transports away any excess of energy input in order to assure that temperature gradients remain flat, and eddies also increase to seamlessly connect the transports. The fact that the Hadley circulation decreases in strength (Figure 2.7, 2.8) means that this increased transport must be due to some combination of increased gross moist stability (Neelin and Held, 1987; Frierson, 2007) or increased eddy moisture fluxes.

In addition to the cloud radiative terms, another contributor to the increased MSE flux in the CanESM5 model is the oceanic heat transport (Figure 2.12). The CanESM5 model experiences the largest decrease in ocean flux divergence in the deep tropics, indicating a decrease in transport by the subtropical cells. This wind-driven circulation declines due to the decrease in wind speed throughout the tropics. In response to the decreased tropical ocean circulation, the Hadley cell and atmospheric eddy energy transports increase. In all models, AMOC declines lead to a reduced southward energy transport across the equator. This is especially strong in the MRI-ESM2-0 model and leads to a southward shift of tropical precipitation.

There is much opportunity for additional climate model experiments similar to the SSP5-8.5ext simulations. Due to the simulation protocol, many aspects of the Earth system that would certainly be changed under such extreme warming are kept fixed. These include the land ice sheets, vegetation types, and the carbon cycle. It would be interesting to examine an intercomparison of fully coupled models that include these processes.

High radiative forcing is one unique aspect of the ECP8.5 and SSP5-8.5 extension simulations, but the extended run length is also important. A recent model intercomparison project aims to understand the century-to-millenium timescale effects of climate change. LongRunMIP is a collection of model simulations that are all at least one thousand years in length, and they each are forced with a constant increase of CO_2 concentrations (Rugenstein et al., 2019a). Most LongRunMIP simulations have smaller radiative forcing than the ECP8.5 and SSP5-8.5 extension pathways. Studies from LongRunMIP have focused on time-dependent climate sensitivity (Rugenstein et al., 2019b), the spatial structure of feedbacks

(Bloch-Johnson et al., 2020), and estimation of equilibrium climate sensitivity (Dai et al., 2020). On centennial to millennial timescales, midlatitude dynamics including the Atlantic basin, dominate global feedback responses (Rugenstein et al., 2019a).

It would also be useful to have a broader range of simulations of warming past 2100. The SSP protocol recommends extension past 2100 of only the extremely high radiative forcing SSP5-8.5ext scenario analyzed here, and the extremely low radiative forcing SSP5-3.4-OSext and SSP1-2.6ext scenarios. Having a range of scenarios with more realistic emissions pathways that are run past 2100 would allow for better quantitative predictions of lasting climate impacts. If there are rapid changes in radiative forcing, or a more sensitive climate than expected, it may be that SSP5-8.5ext simulations will be useful for the understanding of climate impacts in the 22nd and 23rd centuries. Global climate change will not stop in 2100, so it will become increasingly important to understand climate impacts past that date.

Chapter 3

EQUITABLY ADAPTING TO EXTREME HEAT IN WASHINGTON STATE

Adapted from: Poletti, A. N. & Nabayan, J. (2022) Policy Briefs "Identifying and Supporting Underserved Communities through State Energy Assistance" and "Prioritizing Transparency in the Low-Income Heat and Energy Assistance Program," Aspen Institute Tech Policy Hub Climate Cohort

3.1 Introduction

The Western North American heat wave of June-July 2021 resulted in an estimated 1,400 deaths (White et al., 2023) and the highest temperatures ever measured in Canada and Washington (Philip et al., 2022). Temperatures above 40°C (104°F) were observed, which is 3.6 standard deviations from the mean decadal June temperature (Thompson et al., 2022; Philip et al., 2022). Rapid attribution analysis has suggested that this 1-in-1000-year event was made 150 times more likely because of human-caused climate change (Philip et al., 2022).

Extreme heat events will become even more likely as temperatures continue to increase in the coming decades (Masson-Delmotte et al., 2021). Heat waves are the deadliest of climate extremes, accounting for 2,300 deaths in the United States in 2023 alone (Howard et al., 2024), and mortality will only increase under climate change (Lüthi et al., 2023) even when accounting for a decrease in deaths due to extreme cold (Gasparrini et al., 2017). Mortality and human health risks due to climate change emphasize the need for immediate climate mitigation and adaptation strategies. Climate mitigation pathways will be discussed in Chapter 4. In Washington State, the creation of climate resilient communities relies on equitable access to air conditioning (AC).

However, expanding access to air conditioning comes with several challenges, such as:

financial burdens on low-income households, energy burden on communities of color, and strain on the electricity grid. Seattle, once the metropolitan area with the lowest AC usage, has AC in 53% of homes (Balk, 2018) which is an increase from 44% in 2019. In comparison, 90% of U.S. households had air conditioning in 2020 (Beall and McNary, 2022). Additionally, the American Housing Survey in 2015 found that Seattle homeowners are twice as likely to have AC than renters Balk (2018). Additionally, households making a combined annual income of $100,000 were twice as likely to have AC than households making less than $30,000 (Balk, 2018). Federal energy assistance grants often fall short of what is needed to expand AC access.

In Washington, the Low-Income Heating and Energy Assistance Program (LIHEAP) was expanded to allow funds to cover cooling in October of 2021. WA LIHEAP distributed approximately 1,000 AC units in 2022, primarily to households in King County (Weinberger, 2022). However, LIHEAP is a block grant, meaning WA State receives a fixed amount of funding from the federal government and awards LIHEAP funds to qualifying households on a first-come-first-served basis until the money is depleted. Therefore, qualifying, low-income households may go without LIHEAP funds due to an inability to visit a LIHEAP office in-person during regular business hours; this disproportionately impacts multiple-income households, households which are far from a LIHEAP office, and households who do not speak English as their native language. Additionally, these awards, ranging from $250 to $1,000 are frequently enough to purchase a heating unit, a cooling unit, or pay energy bills, but not all three.

Nationwide, Black, Indigenous, and Hispanic households shoulder a larger energy burden than the average American household (Drehobl et al., 2020). To decrease racial disparities in energy burden, the Washington LIHEAP Office became an early adopter of new reporting guidelines from the United States Department of Health and Human Services (US DHHS) by collecting years of race, ethnicity, and gender data on LIHEAP recipients. However, advocacy groups, community members, and academics do not have access to the LIHEAP demographic data or outreach plans to underserved communities. However, across the world, many heat waves are also associated with blackouts, both inadvertent, when the load exceeds capacity,

and from rolling blackouts, which are implemented involuntarily in some neighborhoods to prevent grid failure. The latter are more likely to occur in communities of color and low-income communities. On days with high forest fire risk, preemptive power outages have taken place in California to prevent the possibility of aging electrical transmission equipment igniting wildfires (Guliasi, 2021).

Energy demand in WA is expected to increase by 30% in 2034 and by 100% by 2050 (PNUCC, 2024). These projections find that the largest contributors to increased electricity demand include the electrification of vehicles, manufacturing, and buildings as well as the expansion of data centers. Additionally, WA's reliance on hydroelectricity will be strained by a changing climate; hydropower production is expected to decrease by 2 to 3.4% annually and 12.1 to 15.4% during the summer by 2040 (Hamlet et al., 2010). Demand for residential cooling is expected to increase to 4.8% to 9.1% of the total electricity demand by 2080 (Hamlet et al., 2010). This creates a unique challenge in warmer months, where hydroelectricity is at a minimum but residential cooling demand peaks. Therefore, utilities fail to meet future electricity demand with renewable energy projects, WA risks imposing blackouts on energy-burdened communities.

Currently, WA is an energy exporter (to Oregon, Montana, and Canada), is the leading state in the production of hydroelectric power (producing 25% of the nation's hydroelectric power), and produces 8% of the nation's total renewable electricity (EIA, 2024). Since WA serves as a critical energy producer nationally and internationally, the state's ability to meet internal electricity demand is of both state-wide and nation-wide importance. Yet, WA utilities have expressed skepticism that they will be able to scale up electricity production quickly enough to meet demand.

Large scale renewable energy projects, such as solar farms and onshore or offshore wind turbines, can take years to plan, build, and connect to the electricity grid. In contrast, small-scale solar projects, such as residential rooftop solar, cooperatively owned solar (or, community solar), and microgrids. Whereas residential rooftop solar is only available to homeowners, solar microgrids provide the option for renters to switch to cleaner and cheaper electricity production. Small-scale solar projects provide energy autonomy, as in, the indi-

vidual has control over the means, the cost, and the availability of their electricity generation (DenHerder-Thomas et al., 2020; Kienbaum et al., 2023). Those with access to small-scale solar microgrids would be unaffected by rolling blackouts while also selling solar power back to the electricity grid, increasing the state's total capacity even during peak summer periods; this increases individual, community, and state-wide climate resiliency.

Critics of solar projects (large or small-scale) cite Washington's cloudy weather. However, two of the leading European countries in solar energy production, Germany and the Netherlands, have lower average solar capacity factor than Washington State (11 to 13% compared to 16%; Global Solar Atlas). Additionally, as Washington's peak electricity demand shifts to hot days, peak electricity demand would coincide with peak solar generation, thus increasing state-wide climate resiliency.

Equitably increasing climate resilience in Washington requires understanding which communities are energy-burdened, are currently underserved, and have the highest climate health risks to properly prioritize federal energy assistance and small-scale solar. The Clean Energy Transition Act (CETA), passed in 2019, requires Washington's electricity production to eliminate fossil fuels by 2045. Additionally, CETA requires that all utilities meet "90% of low income customer's energy assistance need by 2050" (RCW, 2019; Thuraisingham, 2021). One way through which utilities alleviate energy burdens on low-income communities is through the federal Low-Income Heat and Energy Assistant Program (LIHEAP). LIHEAP is a block grant provided to states to disseminate to low-income households. Low-income households can apply for LIHEAP funds through a local LIHEAP office (also called a LIHEAP-subgrantee, where the state is the LIHEAP-grantee). Unlike an entitlement which provides money to all qualified individuals, LIHEAP only provides funds on a first-come-first-served basis until the grant is gone. Utilities often act as LIHEAP-subgrantees, directly providing funds to low-income households, or direct low-income households to where they can apply for funds.

However, only Investor-Owned Utilities (IOUs, privately owned utility providers governed by the Utilities and Transportation Commission) are beholden to reporting requirements under CETA. CETA and the WA Utilities and Transportation Commission (UTC) require

IOUs to develop and implement their plans to transition to 100% renewable energy through filing Clean Energy Implementation Plans (CEIPs) every 4 years (WA UTC 2019) with the help of Equity Advisory Groups. CEIPs include how IOUs plan to equitable tackle the energy burden within their service area, including "reduction of burdens for highly-impacted communities and vulnerable populations" (RCW, 2019; Thuraisingham, 2021). Consumer Owned Utilities (COUs, or publicly owned utility providers such as Seattle City Light, governed by the WA Department of Commerce) are not beholden to these reporting requirements. It is thought that COUs are more directly accountable to their service area due to being publicly owned. However, Seattle City Light has refused to make public their data on alleviating low-income energy burden or how they've reduced the energy burden on highly-impacted communities and vulnerable populations.

During my summer fellowship with the Aspen Institute Tech Policy Hub, I worked with the WA Department of Commerce and the advocacy group Front and Centered to provide recommendations on how WA could better identify underserved communities in need of energy assistance. With limited available data, I identified how current energy assistance programs failed to support communities of color. I urged the WA Department of Commerce to collect more demographic data from consumer-owned utilities (COUs) and publish publicly available data on LIHEAP demographics.

3.1.1 Glossary

Listed here are terms frequently use throughout the recommendations, their abbreviations, and definitions in alphabetical order.

1. Clean Energy Implementation Plan (CEIP): Every four years, Investor Owned Utilities are required to submit a report on how they plan to reach CETA targets.

2. Clean Energy Transition Act of 2019 (CETA): Signed by Gov. Jay Inslee, CETA sets clean energy targets for WA electricity generation, requiring 100% carbon free electricity by 2045, as well as electrification targets for vehicles and manufacturing.

3. Consumer Owned Utility (COU): Publicly owned utility provider governed by the WA Department of Commerce, the ratepayers, and local city council. Examples include Seattle City Light.

4. Electricity Grid: The transmissions lines which transport power from where it is generated to users

5. Highly-Impacted Community: CETA defines highly impacted communities as census tracts at high risk and vulnerability to environmental health disparities using the Washington Environmental Health Disparities Map maintained by the Washington Department of Health.

6. Investor Owned Utility (IOU): Privately owned utility provider governed by the Utilities and Transportation Commission. Examples include Avista.

7. Low Income Heat and Energy Assistant Program (LIHEAP): Created in 1981, LIHEAP is a federal block grant disseminated to states (and other LIHEAP grantees). Originally intended to provide heating to low-income households, LIHEAP can now be used for cooling, weatherization, and upgrading to energy efficient appliances.

8. LIHEAP grantee: An organization (e.g., a state, territorial, or tribal entity) that receives federal funding through the Low Income Home Energy Assistance Program (LIHEAP)

9. LIHEAP subgrantee or LIHEAP Office: An organization (e.g., utility provider or nonprofit) that receives funding from the LIHEAP grantee (the state). Subgrantees directly interface with households applying for LIHEAP funds.

10. LIHEAP Model Plan: A document that details how a LIHEAP grantee will administer LIHEAP funds

11. Seattle City Light (SCL): The electricity provider for the Seattle area. The largest owned publicly owned utility in the nation.

12. Service Area: The households that a utility provider provides services (electricity, water, gas, etc.) to.

13. Utilities and Transportation Commission (UTC): An independent WA state agency that regulates IOUs and transportation companies

3.2 Identifying Underserved Communities of Color

While people of color are more likely to be low income, energy burdened, or renting, people of color are not the most likely recipients of government benefits. A new study out of Princeton University, Measuring Social Equity in Urban Energy Use and Interventions using Fine-Scale Data, found that energy intensity inequities in two cities exist across race even when controlled for income (Tong et al., 2021). However, 2022 Census data shows that white, non-Hispanic men are the most likely recipients of government benefits across the US (King, 2025). Therefore, Washington should expand their demographic reporting beyond economic metrics, such as income and energy burden, toward socioeconomic demographics such as race and ethnicity.

While we lack data for Washington state, Washington is not an exception to nationwide racial disparities. In the Biden–Harris Report Advancing Equity Through the American Rescue Plan, the White House calls for coordinated efforts to ensure that Black, Indigenous, and People of Color (BIPOC) households receive energy assistance, since nationwide Black, Indigenous, and Hispanic households have 43%, 45%, and 20% greater energy burdens, respectively, than the median household. Therefore, Washington State should work to identify and reduce energy burden disparities in communities of color, in line with federal priorities.

While Washington lacks necessary data to target underserved communities of color, potential racial disparities can still be identified in the state. Using available Washington State data comparing the racial demographics of zip codes against arrearages, the Energy Project found that people of color serviced by IOUs still had higher energy burdens after LIHEAP and COVID-19 benefits were disseminated, highlighting an additional need for energy assistance within these communities (Thompson and Kimball, 2022). Figure 3.1 examines the percentage of the population that is impoverished and comprises people of color as well

as their proximity to LIHEAP offices in Washington. Figure 3.1 demonstrates two conclusions: first, there are low-income, predominantly white census tracts where a COU energy assistance program could disproportionately place funds; second, that tribal reservations are significantly less likely to be near a LIHEAP office. Therefore, based on COVID-19 relief funds and geographic demographic information, we can see that solely targeting low-income communities is not sufficient to decrease racial disparities in energy burden.

3.3 Demographic Reporting Requirements for Consumer-Owned Utilities

Current reporting requirements for COUs are not sufficient to target racial disparities in energy assistance needed or energy assistance received. Currently, COUs collect data on whether an energy assistance recipient is low-income, is energy burdened, is renting, has limited English, or is older than 65 years old, which are reported in the biennial Energy Assistance Report required of all utilities and submitted to the Department of Commerce. They do not explicitly collect any data on the race or ethnicity of recipients.

COUs currently are not collecting data on race, ethnicity, or high-impact community status because of disparate reporting requirements in the State's Clean Energy Transformation Act (CETA). CETA allows the Department of Commerce to request "any [. . .] information related to the utility's low-income assistance programs," subject to availability, and requires the utilities to demonstrate progress toward serving any identified underserved community. CETA defines highly impacted communities as census tracts at high risk and vulnerability to environmental health disparities using the Washington Environmental Health Disparities Map maintained by the Washington Department of Health, creating a broad and easy-to-utilize metric (UWEOHS, 2022). While the highly impacted community metric considers income, this broad metric also considers exposure to climate impacts and other socioeconomic factors such as rent burden and increased health risks. Therefore, the highly impacted community metric can identify geographies with risk factors beyond income. Additionally, since the highly impacted community metric includes climate and environmental risk, including this metric in COU reporting will increase climate resilience in Washington.

An energy assistance program can potentially disseminate state and federal funds to

exclusively low-income households and still exclude highly impacted communities, without accountability. For example, PSE, an IOU, found in their geographic equity analysis that 25% of their service area was in highly impacted communities, while residents in highly impacted communities accounted for 35% of low-income energy assistance recipients (Table 3.1). There are two conclusions to draw from this statistic: first, that PSE's energy assistance is geographically equitable, and second, that a substantial portion of low-income residents within their service area reside outside of highly impacted communities. Therefore, economic metrics such as income and energy burden are insufficient to target underserved geographies in need of climate resilience.

Though CETA allows the Department of Commerce to request data from utilities on low-income assistance programs, it does not require utilities to collect these data. Because of this, highly impacted community analysis has only been conducted by privately owned or investor-owned utilities (IOUs) through the state's Utilities and Transportation Committee (UTC).

My recommendations for how the Washington State Department of Commerce State Energy Office can encourage COUs to identify and allocate funds toward underserved racial, ethnic, and/or highly impacted communities are outlined below:

3.3.1 Increasing reporting requirements of COUs for data regarding racial, ethnic, and/or highly impacted communities

In addition to current reporting requirements from CETA, the Department of Commerce should request that COUs report the race and ethnicity of each energy assistance recipient as well as whether the recipient lives in a highly impacted community, subject to availability and in accordance with CETA Section 120(3)(b) in the biennial Energy Assistance Report. Current reporting requirements allow COU energy assistance programs to target predominantly white, low-income communities while remaining in compliance with CETA. Including race, ethnicity, and highly impacted community data will help COUs and the Department of Commerce target high-need communities in line with the energy assistance and environmental justice targets in CETA and the Washington Healthy Environment For All (HEAL)

Act, respectively. The Washington Health Disparities Map is a robust tool for COUs to determine how many energy assistance recipients live in highly impacted communities so long as COUs record the recipient's zip code. Therefore, adding highly impacted community data to the report should not pose a substantial technical burden on COUs since the data is readily available.

To identify whether a specific racial, ethnic, or highly impacted community is underserved, the Department of Commerce should amend the CETA Section 120(3)(b) biennial energy assistance report to include an analysis that compares the percentage of energy assistance recipients within a specific demographic (i.e., race, ethnicity, highly impacted community status) to the percentage of residents in the COU service area or LIHEAP office zip code within that demographic. The Department of Commerce should provide technical assistance – for example, assisting in securely collecting and housing data or purchasing missing data – to COUs that lack the tools to securely collect demographic data through public and public–private partnerships. Providing technical assistance to COUs through these public–private partnerships will increase the availability of demographic data, thus removing a barrier for COUs to comply with these new reporting standards. COUs will also be less likely to claim that race and ethnicity data are not available if the Department of Commerce provides accessible technical assistance to collect these data.

Additionally, COUs will need assistance to collect the newly requested data because it often takes a considerable amount of money and staff time to securely collect demographic information from energy assistance recipients. Some public and private agencies, such as existing LIHEAP offices and IOUs, already collect these data and can serve as a model for COUs collecting these data. Thus, the Department of Commerce should establish partnerships between COUs, LIHEAP offices, and IOUs to help COUs collect these data.

3.3.2 Assisting COUs in identifying underserved racial, ethnic, and/or highly impacted communities, and require them to develop a participation plan for outreach

The Department of Commerce should use the reported data to identify any and all underserved demographics in the COU service area and require the COU to create a participation

plan to engage in outreach in these communities. An underserved community or demographic is one where the percentage of energy assistance recipients within that demographic is less than the percentage of residents within that demographic in the service area. A participation plan should include information about which demographics or communities are underserved and a strategy to increase outreach to those demographics or communities in a way that is culturally informed. This could include plans to create outreach materials in other languages, social media campaigns, or even listening sessions in impacted communities.

Since COUs are not experts in community engagement or data science, the Department of Commerce should take an active role in helping COUs identify underserved demographics. It is important that the Department of Commerce require participation plans, not only to ensure that COUs have a plan to increase energy assistance in underserved communities but also to increase communication between COUs and impacted communities. Essentially, participation plans are a tool that communities and the Department of Commerce can use to hold COUs accountable for future actions.

3.3.3 Approving COU participation plans through a public comment period or public hearing on the participation plans

The Department of Commerce should approve participation plans by first allowing public comment and ensuring that COUs sufficiently reply to public comments. COU participation plans should be subject to either a public hearing or a public comment period such that the community as well as advocacy groups can evaluate how effective and equitable the participation plan is. The COUs should submit updated participation plans in response to public comments. Subsequent energy assistance reports submitted by the COU should indicate whether the participation plan from the previous year was successful. Success would be measured by whether the percentage of that demographic in the service area and the percentage of energy assistance recipients within that demographic are equal to or more than the previous year.

By requiring a public comment period or public hearing on COU participation plans, advocacy and community groups can formally provide their feedback and informally enforce

their standards on COU outreach in communities of color. Advocacy groups such as Front and Centered and the Northwest Energy Coalition have already been a part of the legislative, rulemaking, and participation plan process and will continue to provide substantive feedback on COU participation plans in communities of color. In this way, COUs can be held accountable by both the State Auditor's Office and the community itself.

The public comment process will provide informal oversight over COUs while continuing to engage the community at each step of this process. Seeking feedback from the community itself will greatly improve participation plans to ensure that COUs' outreach efforts are effective.

3.3.4 Enforcing the reporting requirements

The Department of Commerce should collaborate with the State Auditor's Office to enforce these proposed reporting guidelines and requirements for COUs so that they can support underserved racial, ethnic, or highly impacted communities. They should develop a clear metric for determining whether COUs are making progress in assisting highly impacted communities, which will aid the State Auditor's Office in formal oversight. The State Auditor could more easily determine whether a COU is in or out of compliance with CETA when "demonstrating progress" specifically means that the COU is approaching a proportionate distribution of energy assistance funds in underserved communities. Therefore, including race, ethnicity, and highly impacted community data in the CETA Section 120(3)(b) survey would encourage COUs to increase engagement with communities of color.

Enforceability is an insufficient reason to exclude race, ethnicity, and highly impacted community data from the energy assistance report. Through CETA section 120(3)(b), Commerce can compel COUs to provide only demographic data beyond estimated low-income and energy burdened households, subject to availability. However, including race, ethnicity, and highly impacted community data in the CETA Section 120(3)(b) report will encourage COUs to properly report demographic data to the State. In 2022, the Department of Commerce requested that utilities report demographic data (such as age and language skills) in their 2022 energy assistance reports. While some utilities stated these data were not available,

several voluntarily collected and reported these data. Therefore, the "subject to availability" clause is not a sufficient reason for Commerce to avoid requesting race, ethnicity, and highly impacted community data, especially after providing technical assistance and working with the State Auditor's Office. Finally, COUs will be less likely to claim that race and ethnicity data are not available if the Department of Commerce provides accessible technical assistance to collect race, ethnicity, and highly impacted community data, as described above.

3.3.5 Evaluate every 2 years whether these reporting requirements and participation plans have decreased racial disparities in energy burdens

The Department of Commerce should evaluate every 2 years whether these reporting requirements and participation plans have decreased the energy burden in communities of color. An evaluation of the statewide success of increased reporting requests and participation plans in communities of color may require a statewide assessment of energy burden. With all COUs providing sufficient data on their service area and energy assistance recipients, the Department of Commerce should be able to create a statewide assessment. However, a statewide assessment may require additional budgetary resources or full-time staff. Ultimately, these recommendations on how to better serve vulnerable communities of color are hamstrung by a lack of demographic data on energy assistance recipient.

3.4 Publicly Available LIHEAP Data through the WA Department of Commerce

The Washington State Department of Commerce Community Services and Housing Division should increase transparency in demographic data collection and outreach within the Washington LIHEAP Office so that the public can become more involved in how LIHEAP identifies and allocates funds toward underserved racial, ethnic, and/or highly impacted communities. Without access to these documents, potential partners such as advocacy and community groups are unable to aid the Department of Commerce in identifying, engaging, and building trust in historically marginalized communities. Additionally, the Washington LIHEAP Office has gone far beyond federal standards for data collection. Lastly, other states that have not collected these data do not currently have a model for which data to

collect and how to collect them. Five recommendations for how LIHEAP Office can increase transparency are outlined below:

3.4.1 Including data reporting requirements for LIHEAP sub-grantees in public-facing documents such as the LIHEAP Model Plan and/or Sample Vendor Agreement

LIHEAP sub-grantees (also known as local LIHEAP vendors) already collect race and ethnicity data; however, advocacy groups are in the dark on what these data are. Therefore, including the data reporting requirements in public-facing documents will make these requirements more clear to advocacy and community groups and will allow them to request relevant data from LIHEAP sub-grantees, lobby for new data requirements, and advocate for resources to be placed in vulnerable demographics. Increasing transparency in Washington LIHEAP reporting requirements will allow Washington State to serve as a model for other states that are just beginning to implement new 2023 federal reporting requirements.

3.4.2 Including LIHEAP sub-grantee documents on the Washington Open Data website

LIHEAP sub-grantees sign an annual Vendor Agreement to continue operating as a local LIHEAP office. These contracts should be public information so that the communities these LIHEAP sub-grantees serve understand the terms of this partnership. For example, communities should understand how LIHEAP sub-grantees are compensated, how long their contracts are for, and what data they're required to collect. In this way, communities can help to hold LIHEAP sub-grantees accountable for the terms of their public partnerships. Currently, the Department of Commerce has uploaded only Fiscal Year 2015 contracts to the Washington Open Data website. The Community Services and Housing Division should consider uploading LIHEAP sub-grantee contracts to the Washington Open Data website.

3.4.3 Including LIHEAP demographic data on the Washington Geospatial Open Data Portal

Given that LIHEAP demographic data contain confidential and sensitive personal information, the Department of Commerce's LIHEAP Office should aggregate and anonymize LIHEAP demographic data for publication on the Washington Geospatial Open Data Por-

tal. During my initial project on equitability in WA LIHEAP funds, the WA Department of Commerce stated that they were working on a publicly available dataset on LIHEAP demographics. Two years later, the Department of Commerce has a draft website on LIHEAP demographics with no publicly available information, no mention of race or ethnicity, and no availability on the Geospatial Open Data Portal While the LIHEAP demographic data soon will be publicly available on the Department of Commerce website, these data will be preprocessed and unavailable for download, making it difficult for a resident to perform their own analysis. Sharing these data on the Geospatial Open Database website in a geodatabase format will allow advocacy and community organizations to download and analyze the data themselves.

The Washington Geospatial Open Data Portal is the central location for advocacy groups, community members, and academics to download data on Washington State and its residents. These data allow for open analysis of relevant and current statewide statistics. When advocacy groups, among others, advocate for data-based policy, they need access to relevant data. Therefore, the Washington LIHEAP Office would increase its community engagement with potential community partners by uploading aggregated and anonymized data to the Washington Geospatial Data Portal. The Washington LIHEAP Office could consider reaching out to the Washington State Chief Information Officer to better understand the state's Geospatial Open Data Guidelines.

In addition, if the LIHEAP sub-grantee is not a utilities provider, the LIHEAP office should share these demographic data with their local utilities provider. Currently, the Washington LIHEAP Office gathers data from their sub-grantees. Similarly, LIHEAP sub-grantees provide limited information to local utility providers, which is reported in the utility's biennial Clean Energy Transformation Act Section 120(b)(3) energy assistance report. Since Washington utilities are not currently required to report on the races and ethnicities of their energy assistance recipients, LIHEAP sub-grantees also do not do so. Therefore, to increase transparency across Washington energy assistance programs, LIHEAP sub-grantees should consider sharing demographic data with their local utility provider.

3.4.4 Encouraging community listening sessions within LIHEAP sub-grantee outreach plans

LIHEAP sub-grantees should be encouraged to host community listening sessions to better understand the needs of their communities. Community listening sessions are informal public hearings, where community members are invited to voice concerns and grievances. The key to successful community listening sessions is that the LIHEAP sub-grantee meaningfully listens and addresses the concerns. Based on these community listening sessions, sub-grantees should submit an outreach plan to the Washington Department of Commerce in their annual application to provide LIHEAP services.

Currently, LIHEAP sub-grantees outreach plans are internal, which does not allow for other community organizations to provide input. Community organizations often have insightful information on how to engage with local, vulnerable populations. Community listening sessions between LIHEAP offices and community members would enhance outreach plans.The outreach plan should detail how the sub-grantee plans to provide additional support to identified underserved communities. These outreach plans should be publicly available for accountability to the public. Additionally, the Washington LIHEAP Office should evaluate outreach efforts during the following year's desk or on-site audit. In order to implement this recommendation, the Department of Commerce should modify their Model Plan.

3.4.5 Distributing standardized outreach materials to LIHEAP sub-grantees

A common community concern is the lack of a consistent and accessible application process for LIHEAP across district offices. For example, each LIHEAP sub-grantee lists different required documents for the application process, and some of these document lists are erroneous. The Chelan County LIHEAP Office requires 12 months of utility bills and 3 months of proof of income, when only 1 month of each is required by the State. The State standard of 1 month proof of income was implemented during the 2019 COVID pandemic, and some LIHEAP sub-grantees such as the Chelan County LIHEAP Office may have neglected to edit their websites after the requirements changed.

In order to standardize the application process and make it easier for applicants to access

benefits, the Washington LIHEAP Office should provide a collection of standardized LIHEAP materials, including:

1. Guidelines for what documents LIHEAP sub-grantees can and cannot ask of LIHEAP applicants,

2. A list of those documents on the Washington Department of Commerce LIHEAP website, and

3. Outreach materials with consistent application information.

These outreach documents should include a streamlined application 1-pager or flyer with the correct application requirements (Figure 3.2). These outreach documents can be used both non-digitally as a flyer/mailer, or digitally on the local LIHEAP office website or on social media (Figure 3.3).

3.5 Conclusions

Between when these recommendations were written (2022) and today, Washington State has made little progress in ensuring that energy assistance funds are reaching vulnerable and highly impacted communities. 25% of low-income homes remained energy burdened in Washington (DOC, 2023). Currently, there is no publicly available data on where LIHEAP funds are distributed within the state. Additionally, Consumer Owned Utilities have not been held to the same regulatory standard as Investor Owned Utilities. COUs which have expanded energy assistance programs and outreach have done so only on a voluntary, opt-in basis without providing demographic data to the Department of Commerce (DOC, 2023). On the federal level, LIHEAP, along with other essential government assistance programs, are on the chopping block (Powers, 2025). As the world continues to warm, it's integral that climate adaptations both correct past *and* prevent future inequities. That goal depends on the continued funding of energy assistance programs and the transition to clean energy across the State of Washington.

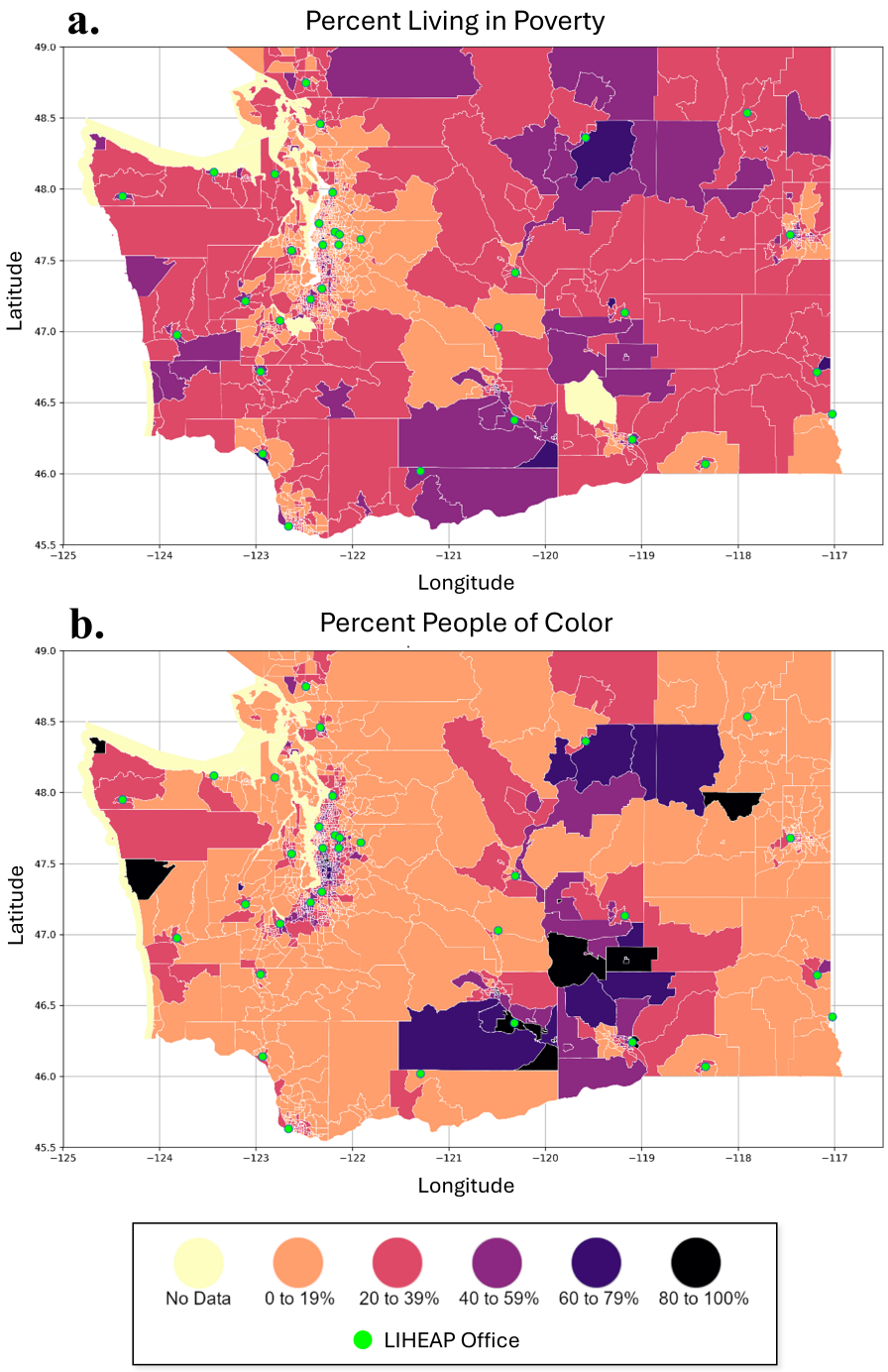

Figure 3.1: Demographics compared to energy assistance access and eligibility (a) The percentage of the population below 200% of the federal poverty level (FPL) per census tract, and (b) the percent of the population that is non-White. The LIHEAP office locations are in green. Data from Washington Geospatial Open Data from February 2022.

Figure 3.2: LIHEAP Application Guide. A sample LIHEAP application guide, including a clear, accessible list of required documents. The guide is customizable, so LIHEAP subgrantees can add their own contact information.

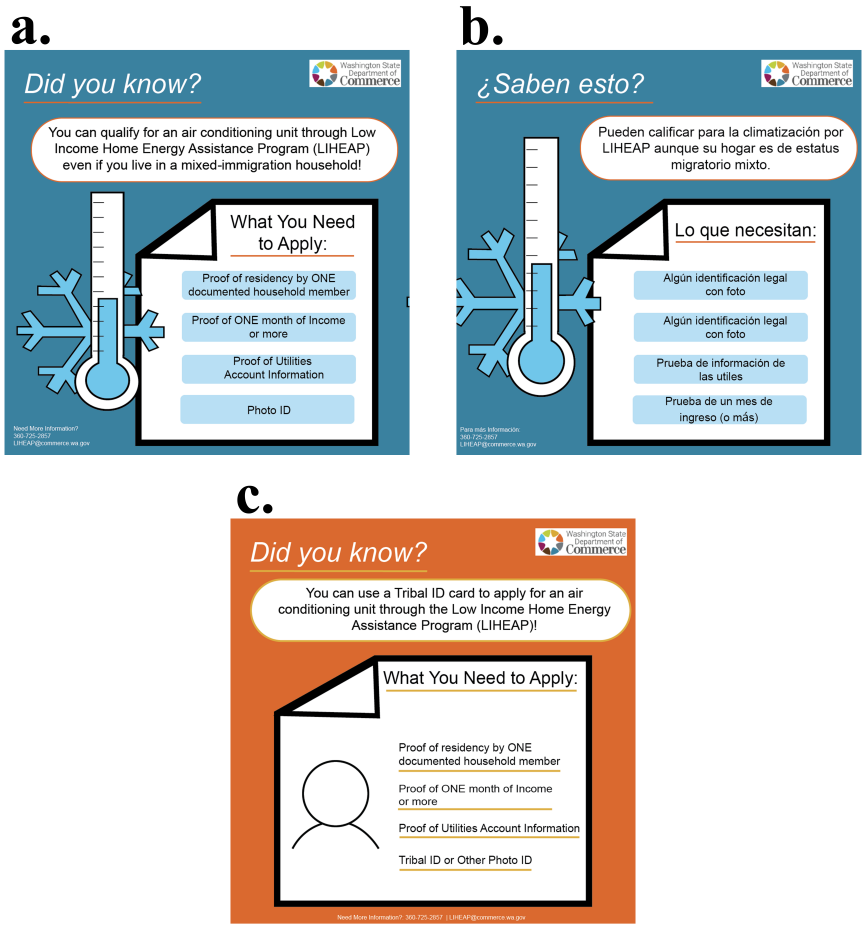

Figure 3.3: LIHEAP Outreach Material. Sample social media posts aimed toward households with (a-b) undocumented members, in English and Spanish, and (c) indigenous households

In Highly Impacted Community	% of Total Contract Accounts	% of Contract Accounts who Received Energy Assistance
No	72.9%	61.1%
Yes	27.1%	38.9%
Total	100%	100%

Table 3.1: Adapted from the PSE 2022 CETA Energy Assistance Report: A comparison of the difference between the percentage of their customer base and the percentage of energy assistance recipients who reside in highly impacted communities in the PSE service area. See the Chapter 3 data availability section to access Washington State Department of Commerce Utility Reports.

Data Availability

Chapter 3 uses the following datasets:

1. Global Solar Atlas. World Bank Group, ESMAP, SolarGIS. https://globalsolaratlas.info/map

2. State of Washington Geospatial Open Data Portal. WaTech Geospatial Program Office. Accessed February 2022. https://geo.wa.gov/

3. Scharff, A. (2022) Washington State Department of Commerce 2022 Utility Reports. Accessed at: https://deptofcommerce.app.box.com/s/6bfjpocil9l9fhjs79akavkzcsym311o

Chapter 4

EVALUATING LOW ENERGY DEMAND SCENARIOS IN FAIR

4.1 Introduction

The path to net-zero carbon emissions is neither simple nor certain. Physical uncertainty stems from uncertainties in the transient climate response to cumulative emissions (TCRE; defined in Section 1.2; Matthews et al. (2009)) and uncertainty in temperature changes which persist after carbon emissions have ceased (defined as the zero emissions commitment or ZEC; (Jones, 2019; Jenkins, S. et al., 2022; Koven et al., 2023)). Scenario uncertainty stems from uncertainties in how zero-emissions are achieved from a socio-economic perspective, which impacts the form and severity of climate consequences onto vulnerable and impoverished communities (Hoegh-Guldberg et al., 2019; Ebi and Hess, 2020; Sadai et al., 2022).

The linearity of TCRE implies that there is path-independence of emissions scenarios, as in, different emissions pathways over time will yield the same final temperature if they reach the same final cumulative CO_2. ZEC, an estimate of additional temperature change after net-zero emissions are reached, is a deviation from the linearity (or path-independence) of TCRE (Jones, 2019; Sanderson et al., 2024). Sanderson et al. (2024) proposes a framework for diagnosing ZEC50 and ZEC100, the temperature change which occurs 50 and 100 years (respectively) after net-zero emissions are reached and maintained, using emissions-driven experiments. Though models agree that ZEC is likely close to zero, the sign remains uncertain with (MacDougall et al., 2020) finding a range of -0.36 to 0.29°C and (Sanderson et al., 2024) finding a range of -0.33 to 0.28 in ESMs fifty years after net-zero. Recent literature finds that ZEC is likely negative over centennial timescales because the uptake of atmospheric CO_2 due too land sinks outweighs warming due to the ocean equilibrating (Tarshish et al., 2023). However, ZEC remains a highly uncertain emergent and transient property without an analytical framework, creating challenges for emissions policy (Jenkins, S. et al., 2022).

Other limits to the path-independence of TCRE include the lagged response of ocean and terrestrial carbon sinks (Winkler et al., 2024) and asymmetry in warming versus cooling due to carbon land sinks (Zickfeld et al., 2021).

CMIP6 attempts to project uncertainties in climate consequences from different climate mitigation and adaptation strategies using the shared socio-economic pathways (SSPs). Despite their wide use, the SSPs have been widely criticized for being inequitable and unrealistic (Hasegawa et al., 2015; Sonja and Harald, 2018; Low and Schafer, 2020). SSPs are designed with a combination of Integrated Assessment Models (IAMs) and Global Climate Models (GCMs). One of the original IAMs balances the marginal cost of climate damage with the cost of climate mitigation (Nordhaus, 1992). The IAMs used in the SSP scenarios model economic interactions between regions under scenario constraints (such as population, gross domestic product, and challenges to mitigation and adaptation) and implement a carbon price to decrease the effective radiative forcing (O'Neill et al., 2016). These emissions pathways can then be simulated in MAGICC (an emissions-to-concentration model) and a concentrations-driven GCM to quantify the physical climate response.

Since increasing productivity (a measure of how efficiently goods and services are produced which depends on the availability of labor and technology) is a necessary constraint in the SSPs (O'Neill et al., 2016; Leimbach et al., 2017; Keyßer and Lenzen, 2021), IPCC recommendations based on SSPs only consider a subset of climate futures which continue current inequities in wealth and energy distribution. For example, Figure 4.1 shows that every SSP scenario has an increasing gross domestic product (GDP). Prioritizing a growing GDP leads SSPs to prioritize economic growth over human wellbeing even though GDP is not (and was not designed to be) a proxy measurement of human wellbeing (Milward-Hopkins et al., 2020; Steinberger and Roberts, 2010). Not only are human wellbeing gains increasingly marginal with increases in GDP in high-GDP nations, but Steinberger and Roberts (2010) finds that the energy and emissions required to satisfy human needs will decrease by 2030.

Even SSP1 which "de-emphasizes economic growth" (O'Neill et al., 2016) maintains energy inequality across the five IAM regions, where the OECD region (countries within the Organization for Economic Cooperation and Development nations such as the United States

and the European Union) consume the most energy per capita and Asia, Latin America, the Middle East, and Africa consume the least energy per capita (Figure 4.2). Additionally, income projections across the SSPs find that none of them reach income equality by 2100 (Cuaresma, 2017; Rao et al., 2019). Emmerling et al. (2024) finds that "across all SSPs, the within-country inequality share rises, whereas, with the exception of SSP4, inequality between countries decreases" but does not disappear by 2100. Andreoni et al. (2024) finds that financing negative emissions technologies (which the SSPs depend on to reach net-zero; Figure 4.3) could double the increase in income inequality. Thus, SSPs put forward futures which proliferate the same wealth and energy inequities they started with.

SSPs and their corresponding IAMs are tasked with contradictory goals: increasing GDP while decreasing emissions. To decouple GDP from emissions, the SSPs don't just need zero-emission energy sources but negative-emission energy sources. These simulations depend on between 100 to 1,000 billion tons of CO_2 removal through negative emissions technologies (NETs), with large land use and air pollution costs (Smith et al., 2016; Heck et al., 2018; Minx and al, 2018; Fuss, 2018). The SSPs use several methods of carbon capture and storage, including direct air capture (DAC), point source carbon capture and storage at fossil fuel plants, and bioenergy carbon capture and storage (BECCS). BECCS burns biofuels as a source of energy while sequestering carbon underground. BECCS captures carbon emitted from burning biofuels and acts as a sink for atmospheric carbon through growing plants.

Turner et al. (2018) estimates that BECCS can take up 0.0173 to 0.0319 $GtCO_2$ per Mha each year. Therefore, 21 $GtCO_2$ of BECCS requires 658 to 1,213 Mha of arable land. Thus the coldest SSPs (e.g., SSP1-1.9) depend on BECCS, and the technology needed to carry out a substantial removal of CO_2 via this approach does not yet exist. In 2022, the Food and Agriculture Organization (FAO) of the UN estimated that there is 4,781 Mha of agricultural land globally, which is one third of the global land area (F.A.O., 2024). 21 $GtCO_2$ per year of BECCS would use 13% to 25% of the Earth's available arable land. Therefore, BECCS at this rate would put unnecessary and undue stress on the population's food supply (Hasegawa et al., 2015).

Additionally, prioritizing NETs over the cessation of fossil fuel usage delays the energy

transition, producing marginal benefit to wealthy populations in exchange for the health and land sovereignty of people of color (Anderson and Peters, 2016; Rao and Min, 2018; Milward-Hopkins et al., 2020; Vogel et al., 2021; Hickel and Slamersak, 2022; Andreoni et al., 2024). Thus, this chapter evaluates climate futures that are more equitable by design.

In this chapter, I evaluate climate futures using an IAM which is not constrained by indefinitely increasing GDP but instead by energy demand and the 1.5°C 2018 carbon budget of 580 $GtCO_2$. In the Methods section, I describe the Keyßer and Lenzen (2021) IAM (henceforth called KLIAM; section 4.2.1), its 17 scenarios, and the choice of the 580 $GtCO_2$ constraint. These scenarios differ from one another by the projected energy demand, the speed of renewables growth, and the quantity of negative emissions technology (e.g., aforestation, reforestation, point-source coal and oil CCS, and BECCS). Keyßer and Lenzen (2021) tune the fuel growth rates (the rate at which renewables grow and traditional fuels are phased out) such that each scenario hits the 580 $GtCO_2$ budget.

With this model, I would like to answer the following questions:

1. How does the socioeconomic pathway to 580 $GtCO_2$ impact 2100 temperature?

2. To what extent can negative emissions technologies reverse warming?

4.2 Methods & Model

4.2.1 Keyßer and Lenzen IAM

The IAMs used in the SSPs (SSP-IAMs) use a production function which projects GDP under certain parameters, such as: capital produced through labor, technical progress, and under the assumption that GDP increases every year (Leimbach et al., 2017). Thus, SSP-IAMs output the fossil fuels emitted to achieve a certain level of production, regardless of whether that production is demanded. SSP-IAMs are therefore "supply-side," answering the question: how much energy, goods, and services could the planet produce with the projected labor force, technological innovation, and international cooperation? In contrast, KLIAM takes energy demand as a constraint, which is "demand-side" (Keyßer and Lenzen, 2021).

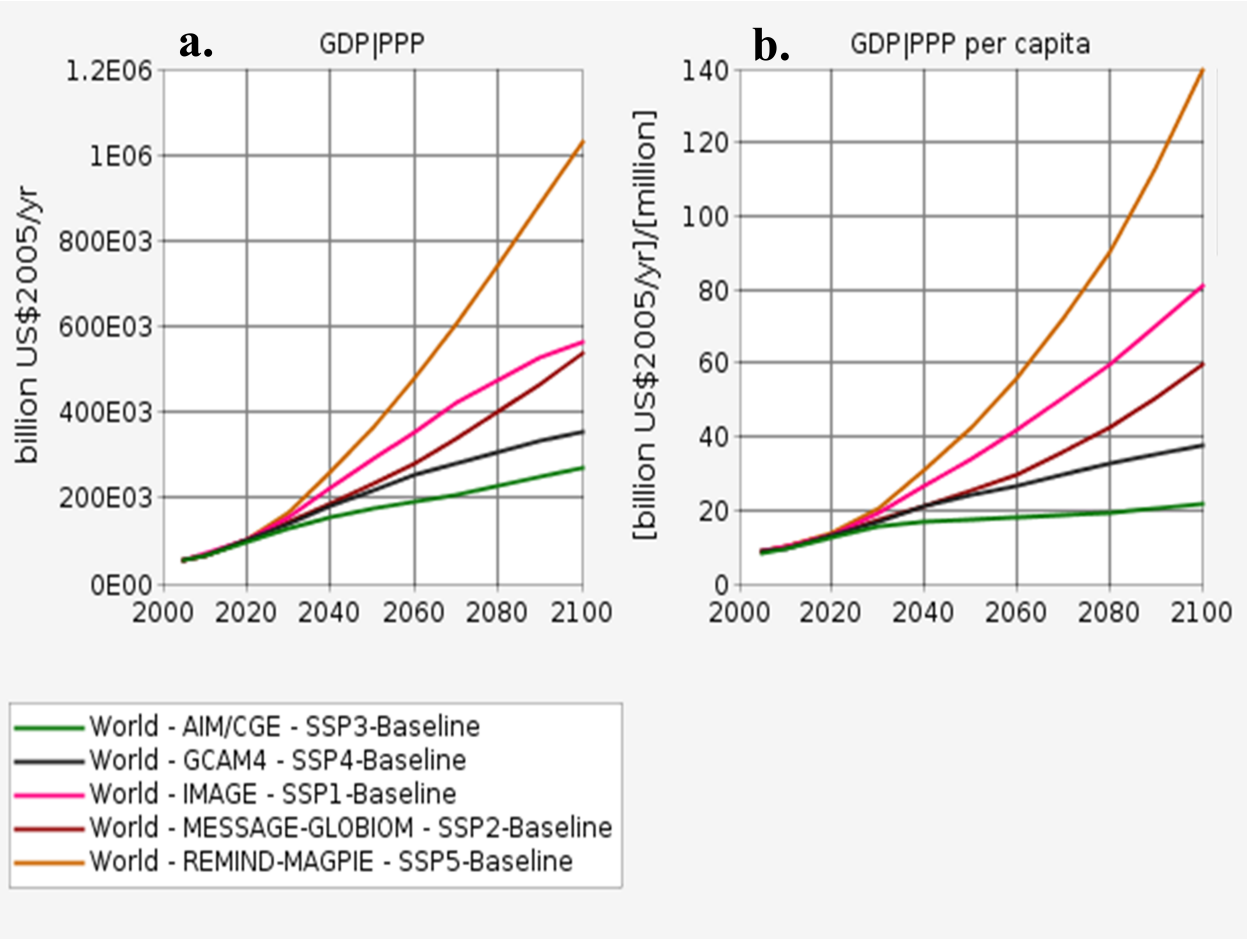

Figure 4.1: SSP GDP Projections. (a) The GDP and (b) GDP per capita of the SSP 1 through 5 baselines (as in, no carbon price) in units of billions of 2005 US dollars per year. Generated from SSP Public Database Version 2.

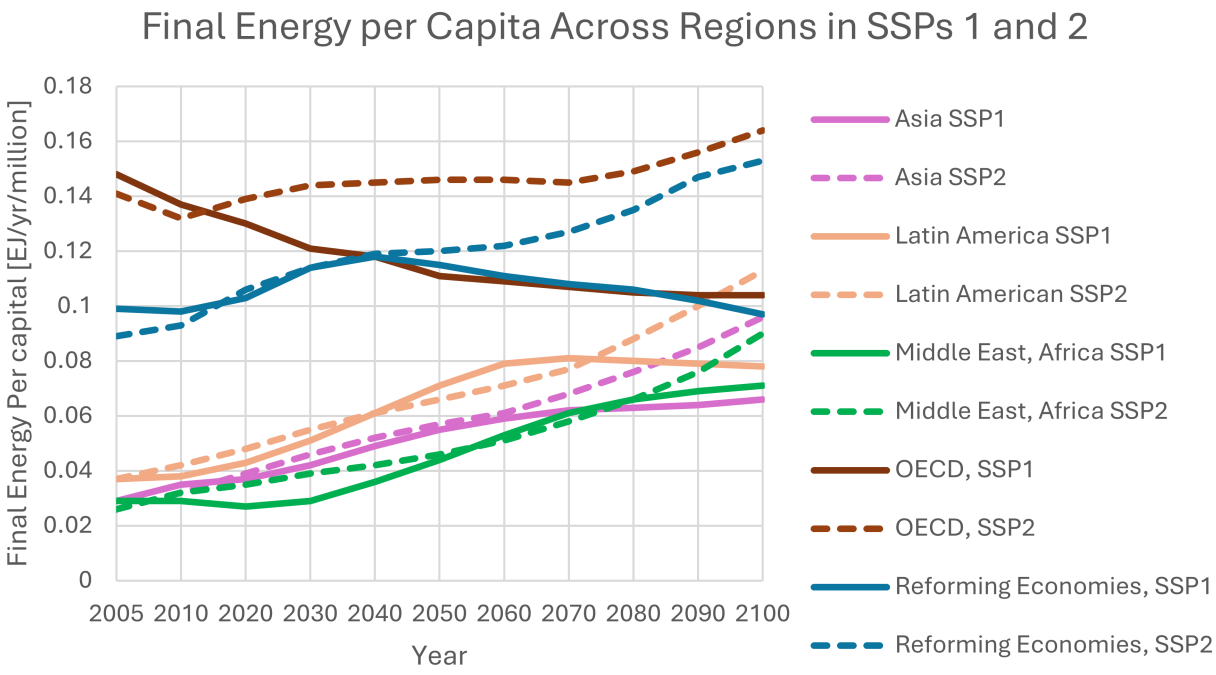

Figure 4.2: SSP Per Capita Energy Projections. The final energy per capita across Asia (purple), Latin America (orange), the Middle East and Africa (green), OECD (dark red), and Reforming Economies (blue) for SSP1 (solid lines) and SSP2 (dotted line) in units of millions of EJ per year. Data from the SSP Public Database Version 2. Damerau et al. (2016) shows the population projections for each region to 2050. The regions with the largest to smallest populations are Asia, the Middle East and Africa, OECD, Latin America, and finally the Reforming Economies. Asia has a population approximately 3.6 times as large as OECD, while the Middle East and Africa have the largest rate of population increase.

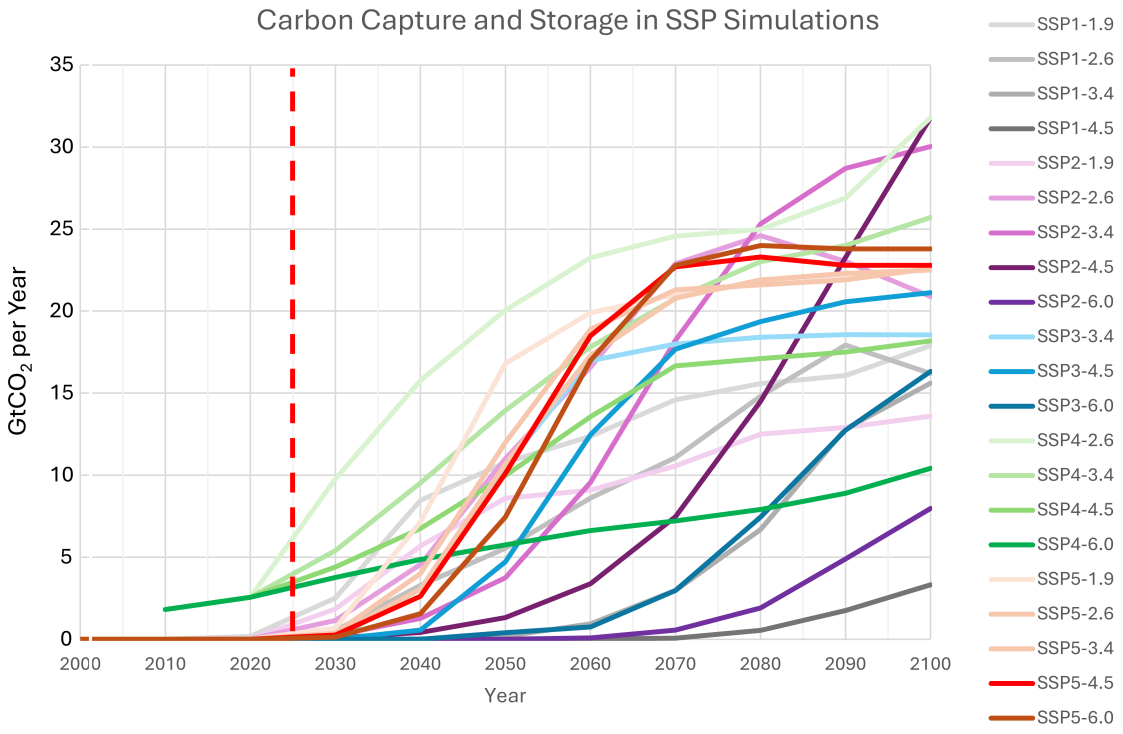

Figure 4.3: SSP Carbon Capture Projections. The carbon capture and storage in SSPs 1 through 5, in units of $GtCO_2$ per year. The dashed line represents 2025. Data from the SSP Public Database Version 2.

KLIAM answers the question: what energy mix satisfies projected energy demand? In this way, KLIAM finds the minimum production needed for a population whereas SSP-IAMs find the maximum supply produced by a population. In this section, I will describe the inputs, functions, outputs, and assumptions within KLIAM.

First, KLIAM models eight energy sources to satisfy energy demand. All fuel types, from renewable (solar, wind, and other) to traditional (coal, oil, natural gas, nuclear, and biofuels) are prescribed a growth rate. The energy produced by each fuel type is calculated as:

$$e_c(t) = e_c(t-1)(1+\gamma_c(t)) = e_c(t-1)[1+(\gamma_c(t-1)+\delta_c)] \quad (4.1)$$

where e represents energy, c represents the fuel type (0: Natural Gas, 1: Coal, 2: Crude Oil, 3: Nuclear Energy, 4: Biofuels, 5: Hydroelectricity, 6: Solar Photovoltaic, 7: Wind, 8: Other Renewables), γ is the annual growth rate, and δ is the annual change in the growth rate. For renewables, the growth rate γ eventually plateaus but it never declines. Therefore:

$$\gamma_c(t) \geq 0 \text{ for c in } [6,7,8] \quad (4.2)$$

The total energy supplied is therefore:

$$e_{supply}(t) = \sum_{c=0}^{8} e_c(t) \quad (4.3)$$

Note that for fossil and biofuels, the primary energy calculated here must be converted to final energy, where final energy is the energy after accounting for loss due to heat in combustion reactions. For most scenarios, energy demand is calculated in the same manner as e_c:

$$e_{demand}(t) = e_{demand}(t-1)(1+\gamma_{demand}(t)) = e_{demand}(t-1)[1+(\gamma_{demand}(t-1)+\delta_{demand})] \quad (4.4)$$

therefore energy demand growth will eventually decline as it does for all conventional fuels (as in, natural gas, coal, and crude oil).

Keyßer and Lenzen (2021) created 18 scenarios of which I include 17 (one of the scenarios titled "Climate Analytics" is largely excluded from the results in the original paper; Table 4.1).

The low energy demand scenarios include Degrowth and DLE (Decent Living Energy). The medium energy demand scenarios include Dec-moderate, Dec-strong, and Dec-extreme (where dec-moderate has the slowest renewable growth and dec-extreme has the fastest renewable growth). The high energy demand scenarios include Moderate, Strong, Extreme and Utopian (where Moderate has the slowest renewable growth and Utopian has the fastest renewable growth). IPCC is a high energy demand scenario meant to represent decoupling of GDP from energy usage (i.e. indefinitely growing GDP but energy use eventually stagnating). This chapter will not go into detail on GDP-energy decoupling, but more details on GDP-energy decoupling can be found in Keyßer and Lenzen (2021). Additionally, there are alternative scenarios of Degrowth, Dec-Extreme, Moderate, and IPCC which include carbon capture and storage ("FullNET") and no negative emissions even from reforestation ("NoNNE").

K&L chose the 2018 carbon budget because this was the relevant budget when the model and scenarios were developed. Future work with KLIAM could create new scenarios tuned to a more recent carbon budget (such as 250 $GtCO_2$ for a 50% change of avoiding 1.5°C warming in 2023; Lamboll et al. (2023)) or a 2°C warming target. However, that is outside of the scope of this chapter.

These scenarios are then evaluated on feasibility of the necessary annual growth of renewable energy, scalability of negative emissions technology, and the rate of GDP-energy decoupling. The energy consumption per fuel source and GDP are shown in Figures 4.4 and 4.5 for each scenario. The total energy consumption, emissions, and cumulative emissions are shown in Figure 4.6 for each scenario.

In Keyßer and Lenzen (2021), "FullNETs" scenarios allow for the maximum amount of afforestation, point source carbon capture and storage (CCS) of coal and oil, and bioenergy carbon capture and sequestration (BECCS). Since each scenario is tuned to reach the same carbon budget, Full NET scenarios can phase out fossil fuels later in the simulation while reaching the same budget as a scenario with limited or no NETs. Both afforestation and point source CCS are self-limiting. The maximum CO_2 sequestered by afforestation is 3.6 $GtCO_2$ per year (Harper et al., 2018).

Additionally, point source CCS of coal and oil is phased out when coal and oil are phased out. BECCS is a process by which biofuels (e.g., corn and ethanol) are burned, their emissions are sequestered, and atmospheric carbon is sequestered by additional plant growth. BECCS sequesters the most CO_2 and does not depend on fossil fuels; therefore, BECCS is never phased out. KLIAM limits the yearly uptake of CO_2 from BECCS, as it does afforestation, anywhere from 0 (No NET scenarios) to 20.4 $GtCO_2$ (the "Full-NET" scenarios), wherein the maximum land use sink is 24 $GtCO_2$ (which in consistent with SSPs and economic modeling; Fajardy et al. (2021), Griscom et al. (2017)).

KLIAM does not take population as an input. Several of the energy demand scenarios are based on the final energy demand in SSP2 or SSP5, providing an implicit population projection. In the scenario DLE, the final energy demand is based on the per capita energy use to achieve the decent living standard defined in Rao and Min (2018), but because that energy demand is constant for several decades, that scenario either assumes a constant population or decreasing energy demand per capita. Future work could consider implementing population as an input in KLIAM.

4.2.2 Methane Pathways

CH_4 is the second most important greenhouse gas, with a global warming potential (GWP) 28 times that of CO_2 (on a 100-year timescale; Forster et al. (2021)) but a significantly shorter lifetime (approximately 10 years). The contribution of CH_4 to current warming and the cumulative CO_{2e} budget is significant (Jenkins et al., 2021; Rogelj and Lamboll, 2024). Therefore, to properly project future warming and partition this model, I constructed a methane pathway.

Methane emissions come from several sources: natural sources (such as wetlands), anthropogenic non-energy sources (e.g., landfills), and fossil energy sources (coal, oil, natural gas). I maintain a constant value in time and across scenarios for natural sources. For anthropogenic non-energy sources, I assume a gradual decrease over time (constant over all scenarios). I perform a linear regression on the last 50 years of SSP1-1.9 CH_4 emissions for the following linearization:

Scenario		Maximum Cumulative CO_2 [$GtCO_2e$ / $GtCO_2$]	Final Cumulative CO_2 [$GtCO_2e$ / $GtCO_2$]	Year of Net Zero [Y]	Final Temperature [K]
Name	*Description*				
Degrowth	Low energy demand scenarios based on the concept of "Degrowth" described in Hickle (2021) as "a planned reduction of energy and resource use designed to bring the economy back into balance with the living world."	196 / 54	61 / -77	2056	1.32 ± 0.27
Degrowth-FullNETs		433 / 244	97 / -86	2060	1.36 ± 0.28
Degrowth-NoNNE		23 / -101	23 / -101	2055	1.30 ± 0.26
Degrowth-PeakCO2		*433 / 244*	*433 / 244*	-	*1.49 ± 0.30*
Moderate	High energy demand scenarios based on SSP5-1.9 with moderate renewables growth and a delayed phase out of fossil fuels.	369 / 215	-25 / -166	2058	1.33 ± 0.27
Moderate-FullNETs		512 / 350	-6 / -164	2062	1.49 ± 0.31
Moderate-NoNNE		*23 / -120*	*23 / -120*	*2046*	*1.30 ± 0.26*
Moderate-PeakCO2		*512 / 350*	*512 / 350*	-	*1.83 ± 0.38*
Strong	High energy demand scenario based on SSP5-1.9 with faster renewables growth than "Moderate." Utopian has the fastest rate of renewables growth, followed by Extreme and lastly, Strong.	222 / 86	-67 / -194	2052	1.29 ± 0.26
Extreme		158 / -5	-72 / -183	2052	1.28 ± 0.26
Utopian		113 / 32	-71 / -190	2053	1.28 ± 0.26
IPCC	A high energy demand scenario based on SSP2-1.9 where energy demand eventually decouples from GDP. As in, GDP continues to increase year-to-year, but energy demand eventually flattens.	74 / -36	-45 / -150	2060	1.29 ± 0.26
IPCC-FullNETs		357 / 217	40 / -87	2059	1.35 ± 0.28
IPCC-NoNNE		-41 / -152	-41 / -152	2045	1.28 ± 0.25
IPCC-PeakCO2		*357 / 217*	*357 / 217*	-	*1.47 ± 0.30*
Dec-Moderate	Medium energy demand scenarios, where "Dec-Moderate" has the same renewable growth rate as "Moderate" and "Dec-Strong" has the same renewable growth rate as "Strong."	373 / 220	42 / -100	2058	1.35 ± 0.28
Dec-Strong		182 / 54	0 / -121	2057	1.31 ± 0.26
DLE	A low energy demand scenario where everyone has access to the energy usages for a decent life, based on the energy usages described in the decent living standard DLS (Rao & Min 2018, Milward-Hopkins et al.)	94 / -48	94 / -48	2097	1.33 ± 0.26
Dec-Extreme	Medium energy demand scenarios with fast renewables growth (as in "Extreme").	89 / -26	-10 / -121	2061	1.29 ± 0.26
Dec-Extreme-FullNETs		331 / 207	32 / -81	2059	1.35 ± 0.28
Dec-Extreme-NoNNE		-39 / -145	-39 / -145	2058	1.28 ± 0.26
Dec-Extreme-PeakCO2		*331 / 207*	*331 / 207*	-	*1.45 ± 0.29*
	Range *(Excluding Peak-CO2, and Moderate-NoNNE)*	-41 to 512 / -152 to 350	-45 to 97 / -190 to -48	2052 to 2097	1.28 to 1.49

Table 4.1: Summary of Scenarios. The names and description of each scenario, the maximum cumulative CO_2 and final cumulative CO_2 above the 580 $GtCO_2$ budget (with and without non-CO_2 gases), the year of net-zero emissions, and the the final temperature (averaged over the last five years) with 1 σ variability from the 6,729-member FaIR ensemble. Scenarios ending in "FullNETs" include point source carbon capture and storage as well as bioenergy carbon capture and storage. Scenarios ending in "NoNNE" includes neither negative emissions technologies nor reforestation. Scenarios ending in "peakCO2" are described in Section 4.3.2 and are not constrained to a 580 $GtCO_2$ budget. All other scenarios have reforestation but no other negative emissions technology. New experiments (as in, those not from K&L) are italicized and not included in Figures 4.4-4.5 or in the range of values stated in the final row.

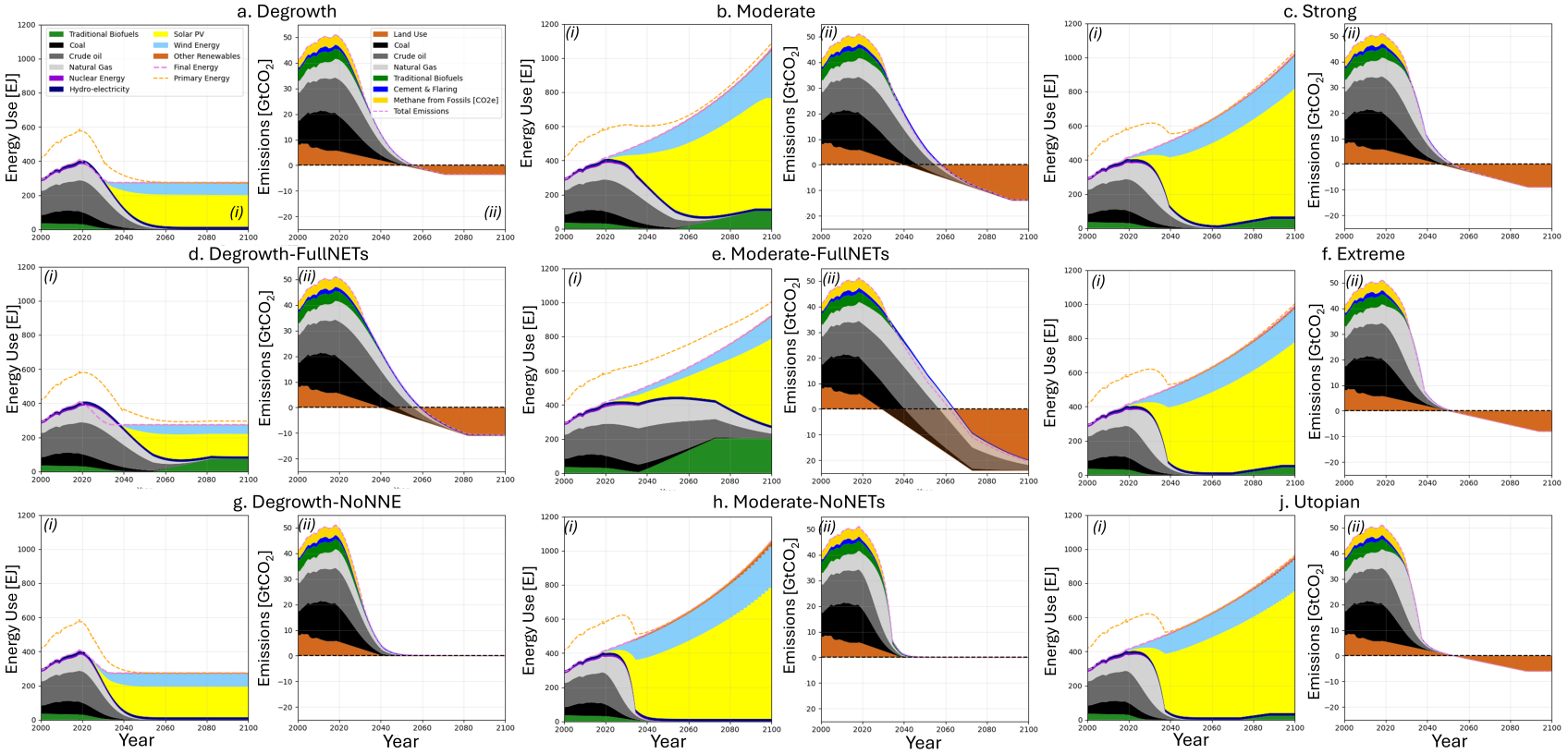

Figure 4.4: The Energy Usage and Emissions Across Scenarios. (*i*, left panel) The final (light purple, dashed) and primary (orange, dashed) energy per year, how much is satisfied by each fuel source: biofuels (green), coal (black), crude oil (dark gray), natural gas (light gray), nuclear (purple), hydroelectricity (blue), solar photovoltaic (yellow), wind (light blue), and other renewables (orange). (*ii*, right panel) The total emissions (light purple, dashed) from each source: land use (orange), coal (black), oil (dark gray) natural gas (light gray), biofuel (green), cement and flaring (blue), methane (yellow). This figure includes the following scenarios: (a) Degrowth, (d) Degrowth-fullNETs, (g) Degrowth-NoNNE, (b) Moderate, (e) Moderate-FullNETs, (f) Moderate-NoNNE, (c) Strong, (f) Extreme, and (j) Utopian.

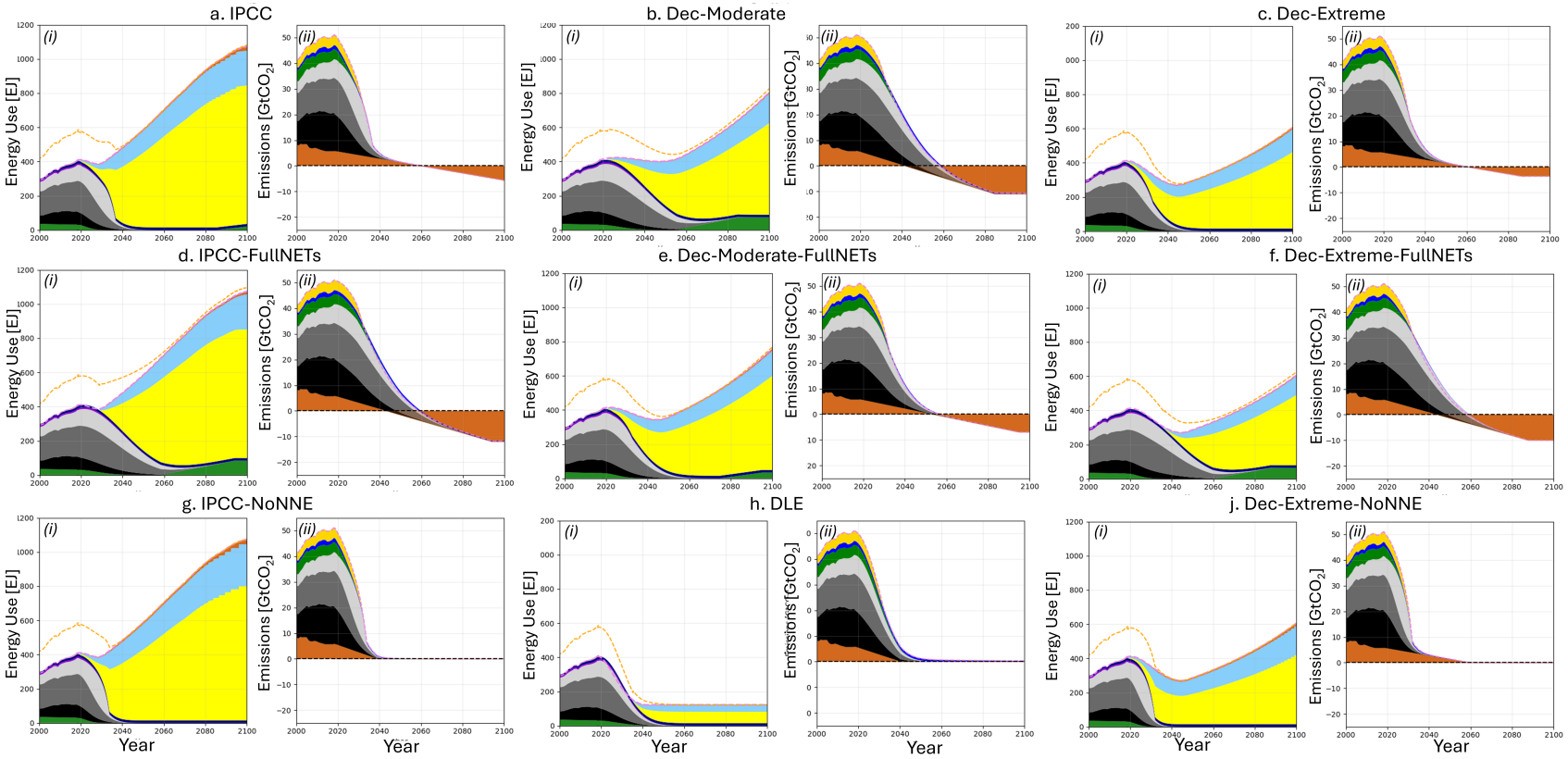

Figure 4.5: The Energy Usage and Emissions Across Scenarios, *continued*. As Figure 4.4 for the following scenarios: (a) IPCC, (d) IPCC-FullNETs, (g) IPCC-NoNNE, (b) Dec-Moderate, (e) Dec-Strong, (h) DLE, (c) Dec-Extreme, (f) Dec-Extreme-FullNETs, and (j) Dec-Extreme-NoNNEs.

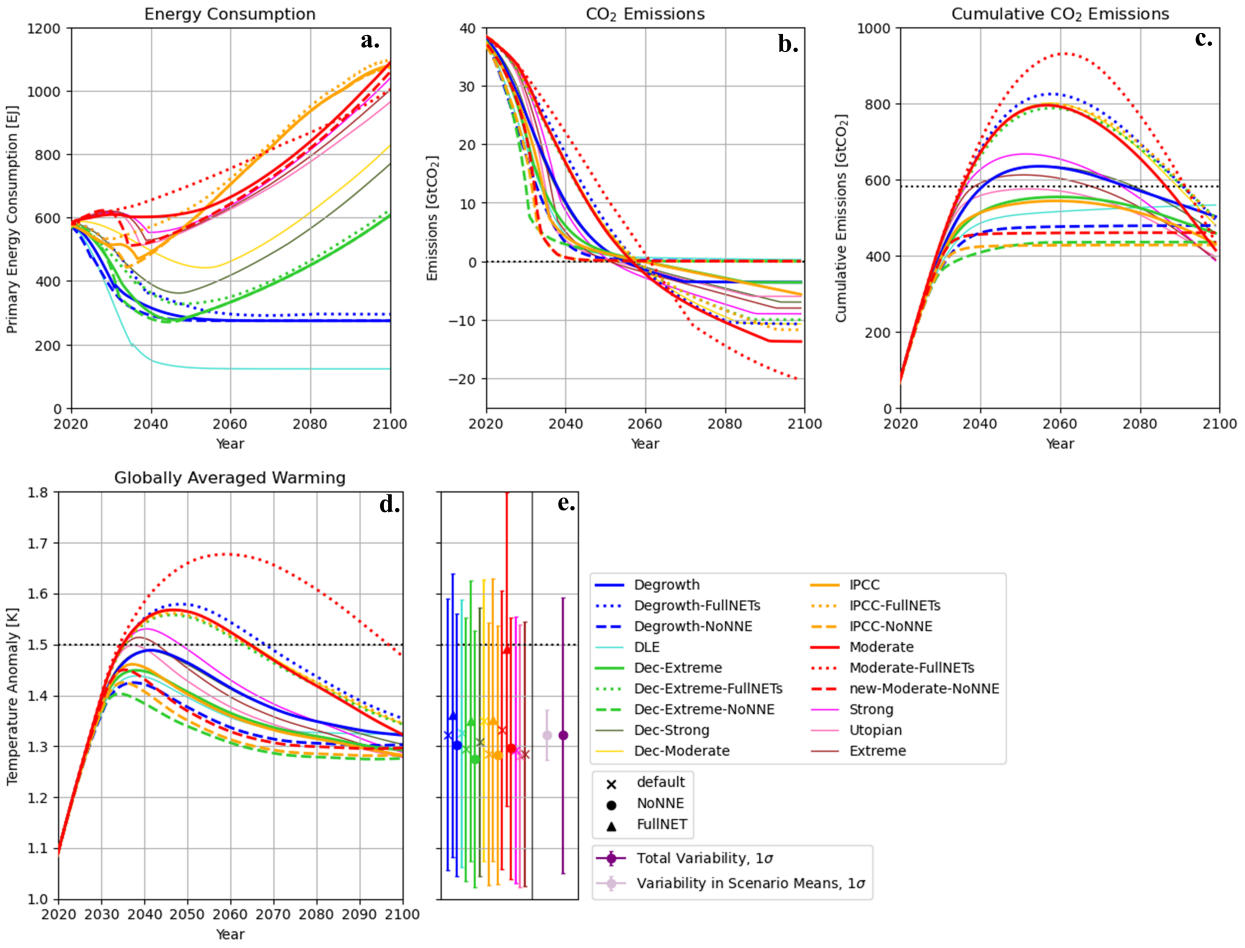

Figure 4.6: The Total Energy, Emissions, and Cumulative Emissions across Scenarios. Energy, emissions, cumulative emissions and temperature time series for the original K&L scenarios with a methane pathway. (a) The final energy production in EJ, (b) the emissions in $GtCO_2$ (c) the cumulative CO_2 emissions in $GtCO_2$ and (d) the near-surface temperature anomaly in K for (a-d) each scenario from 2020 to 2100. (e) The 1 σ physical variability of the final temperature (5-year average) each scenario from the FaiR ensemble (in color), the 1 σ variability of the scenario mean final temperatures (gray), and the total variability across scenario and ensemble space (black).

$$E_{CH_4}(t)_{non-energy} = (At + B)E_{CH_4}(2019)_{non-energy} \quad (4.5)$$

where A = -0.0069 $MtCH_4yr$ and B = 0.877 $MtCH_4$. Note that this linearization eventually reaches negative CH_4 emissions, but not until after the model runtime.

Finally, for fossil energy sources, I model the CH_4 emissions by the amount of natural gas, oil, and coal burned every year. The burning of fossil fuels is not itself a major source of CH_4. Instead, methane is released during the mining, processing, and transportation of fossil fuels, as in, natural gas leaks or methane released from coal mines. Using International Energy Agency (IEA) estimates of methane released by coal, oil, and natural gas divided by historical emissions of CO_2 from each fossil source, I estimate the rate that each fossil source releases methane (IEA 2023):

$$E_{CH_4,i} = \alpha \frac{E_{CO_2,i}}{GWP_{CH_4}} \quad (4.6)$$

where i refers to which fossil fuel (coal, oil, natural gas) and α is the unitless ratio (0.090, 0.099, and 0.160, respectively) calculated using global 2018 emissions from the IEA Methane Tracker. Figure 4.7 shows the methane pathway in two representative KLIAM scenarios (Degrowth and Moderate) compared to SSP1-1.9 and SSP2-2.6.

4.2.3 Coupling to the Finite-amplitude Impulse Response Model (FaIR)

I couple KLIAM to the Finite-amplitude Impulse Response Model (FaIR) to generate temperature projections for each scenario. FaIR models 30 different gases, including a carbon cycle where CO_2 has four timescales and interacts with CH_4 and N_2O emissions. In this analysis, I have chosen to model CO_2 and CH_4 using KLIAM but not the other gases FaIR takes into account. This is for two reasons: firstly, CO_2 and CH_4 are the two most important greenhouse gases. In Figure 4.8, I see that CO_2 and CH_4 have the largest contribution to the total radiative forcing. The short-lived pollutant with the largest impact on the radiative balance in FaIR are Sulfur compounds, contributing -0.23 W/m^2 (2022 median effective radiative forcing). Future work could consider modeling the impact of fossil fuel burning on aerosol concentration.

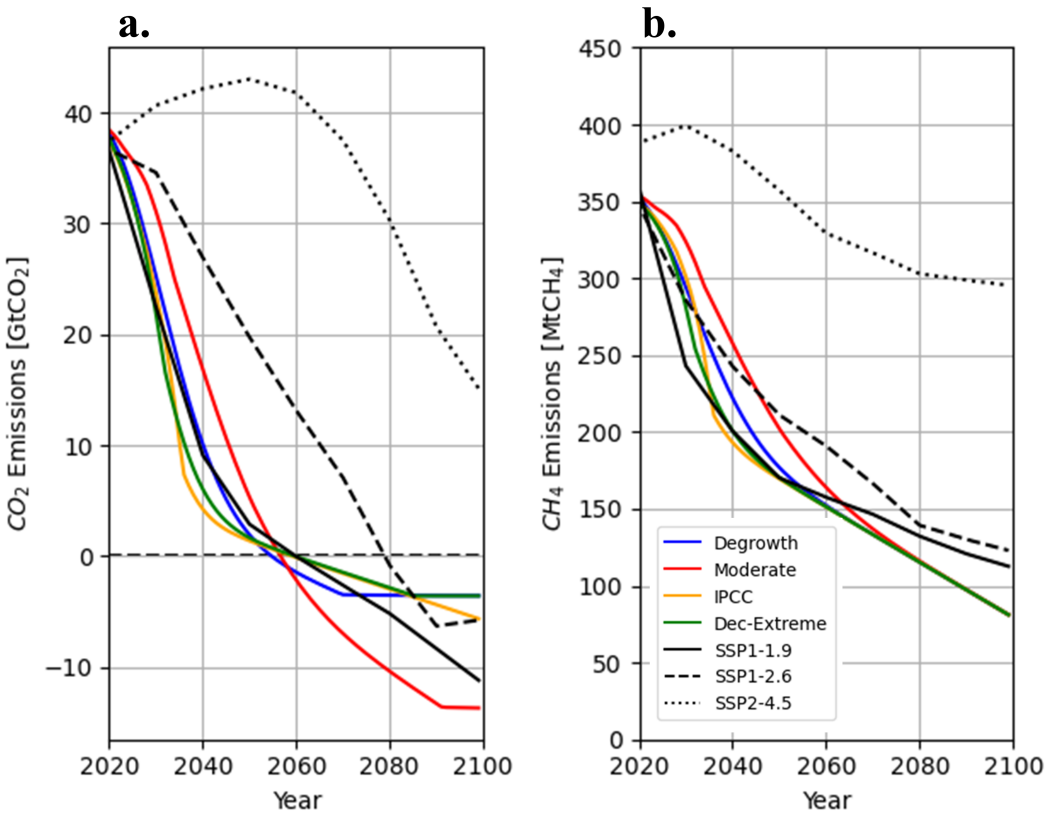

Figure 4.7: A Comparison of CO_2 and CH_4 Pathways to SSPs 1 and 2. The (a) fossil CO_2 and (b) CH_4 emissions for Degrowth (blue), Dec-Extreme (green), IPCC (yellow), Moderate (red), SSP1-1.9 (black, solid), and SSP1-2.6 (black, dashed), and SSP2-4.5 (black, dotted).

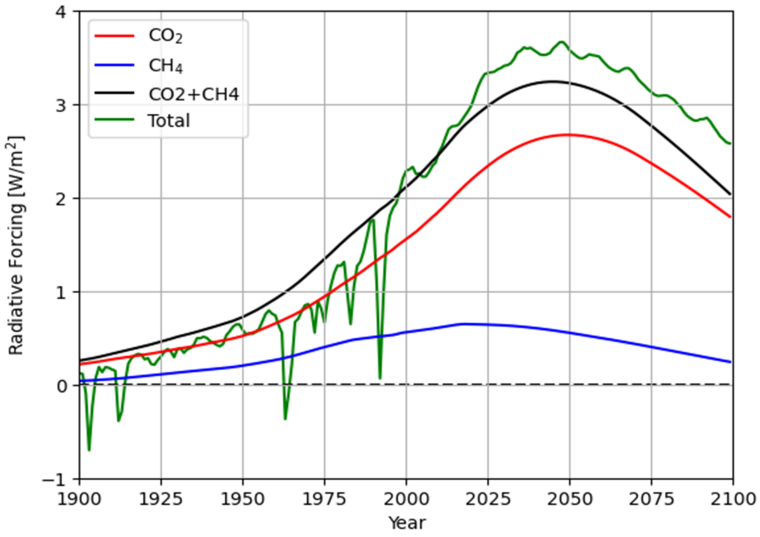

Figure 4.8: Total, CO_2, and CH_4 Radiative Forcings. Timeseries of radiative forcing [W/m^2] of CO_2, CH_4, the sum of CO_2 and CH_4, and the total radiative forcing from all 30 of the modeled gasses in FaIR for Moderate-FullNETs.

Secondly, KLIAM only models emissions from energy sources, whereas some CH_4 and most N_2O emissions arise from agriculture. When coupling KLIAM to FaIR, I use values from the Reduced Complexity Model Intercomparison Project (RCMIP) for all other gases. The RCMIP emissions data provides the emissions for every input gas for every SSP scenario. For this analysis, I use SSP1-1.9 RCMIP emissions data. I use FaIR with a two-layer ocean and a more than 6,729-member ensemble from Dvorak et al. (2022). Additionally, the runtime of FaIR is short enough to allow large ensembles without large computing power. The possible ensemble size, range of climate and carbon cycle parameters, and inclusion of non-CO_2 gases makes FaIR a natural choice for this work. However, simple models such as FaIR fail to model certain interactions in the carbon cycle such as carbon-ocean heat feedbacks (Séférian et al., 2024) which may impact our results. I discuss caveats of our climate model choice in the conclusions of this chapter. The temperature time series from this ensemble is shown in Figure 4.6d and the uncertainty is included in Table 4.1 and Figure 4.6e.

4.2.4 Evaluating Fossil Fuel Pathways for 2023

In this section, I will evaluate how well KLIAM projected fossil fuel pathways from 2018 to 2023 by comparing projections to recent historical data. Additionally, I will present a set of updated fuel growth parameters for fossil fuels for projections beginning in 2023. Future work should consider evaluating and updating parameters for renewable energy (solar, wind, and others) as well as traditional biofuels, hydroelectric, and nuclear.

In this section, we don't focus on traditional biofuels, hydroelectric power, or nuclear power because they present a small and decreasing portion of the energy mix. However, nuclear power is a form of clean (if not renewable) power which could be a part of decarbonization pathways; analyses from this perspective may want to update nuclear energy pathways in this IAM. This section also does not focus on renewable energy. The 2023 growth rate for global solar is estimated between 25 and 30% (IEA 2024, Graham and Fulghum (2024)). Renewable energy growth in KLIAM is determined both by its fuel growth parameters (γ and δ) but also on whether the model over or under supplies energy demand (which depends on the growth rate of energy demand as well as each other fuel source). Properly projecting renewable growth over time in KLIAM requires not only updating its growth parameters but also evaluating whether reducing renewable energy in cases of overshot demand is realistic. Thus, this section evaluates the five-year period 2018 to 2024 of fossil fuel phase out (or lack thereof) in comparison to KLIAM projections. Additionally, changing the fuel parameters and model start year removes the 580 $GtCO_2$ constraint. Therefore, the analysis in Section 4.3.2 will use the original 2018 KLIAM parameters.

I first updated the initial conditions using the IEA World Energy Balances Dataset. KLIAM models growth in each fuel recursively; therefore, the initial demand for each fuel source impacts the growth of that fuel over the model runtime. Table 4.2 shows how the initial value of each fossil fuel for 2018 compared to 2023. Natural Gas, Coal, and total final energy increased from K&L 2018 values to 2023. Contrastingly, Oil decreased in demand by 7 EJ.

Secondly, I updated the fossil fuel growth parameters. While K&L begins its model run in 2018, its analysis uses IEA data from 2015 to 2017, thus assuming that the growth parameters

for 2015 would be consistent into 2018. I update these growth parameters using IEA World Energy Balances, which contains historical data of fossil and renewable fuel consumption up to 2023.

For each fossil fuel type, I consider the percent change each year, defined as:

$$\gamma_c'(t) = \frac{E_c(t) - E_c(t-1)}{E_c(t-1)} \times 100\% \quad (4.7.1)$$

over historical data. I use the average percent change (eqn 4.7.1) from 2020 to 2023 to estimate γ in 2023:

$$\gamma(2023) = \frac{\gamma'(2020) + \gamma'(2021) + \gamma'(2022) + \gamma'(2023)}{4} \quad (4.7.2)$$

To update the δ parameter, I selected two periods of time: one of fast fossil fuel growth (2000 to 2005) and one of slow fossil fuel growth (2010 to 2015). I then defined δ as the average yearly change in γ between those time periods. The updated fossil fuel parameters are in table 4.3.

How well do the K&L parameters project fossil fuel consumption between 2018 and 2023? Figure 4.9 shows that K&L overestimated oil and natural gas production and underestimated coal production between 2018 and 2023. The shaded regions in Figure 4.9 show the lowest and highest demand K&L fossil fuel projections, which I will refer to as the K&L range. Beyond 2023, my updated oil projection sits within the K&L range and is phased out after 2090. My updated coal projection is significantly higher than the K&L range, as the 2018 K&L parameters assumed that coal consumption had peaked prior to 2020. My coal projection phases out by 2080. Finally, My updated natural gas projection is above the K&L range, especially after 2070 and never phases out. In conclusion, the world is not on track to phase out fossil fuels by 2050, or even by 2100.

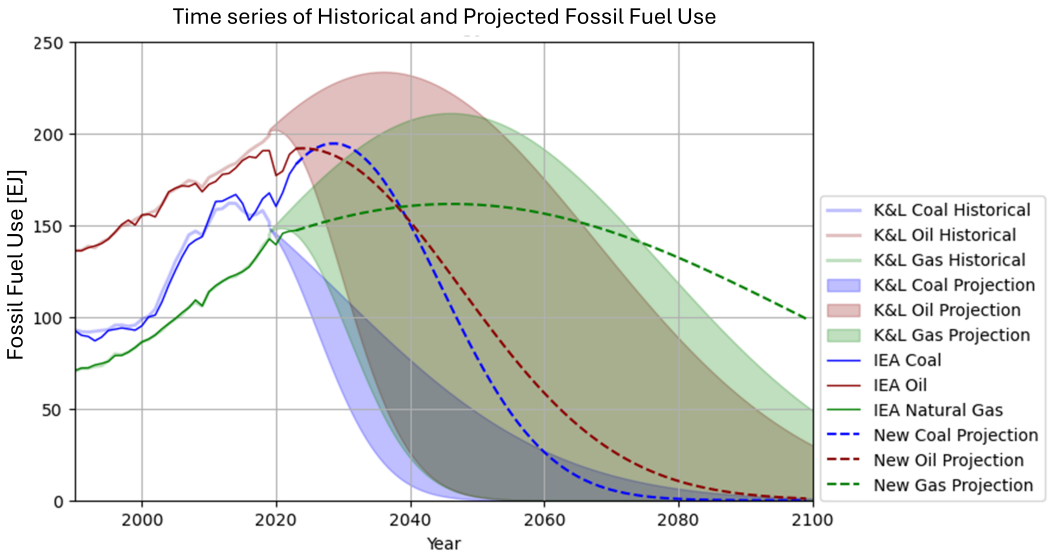

Figure 4.9: Historical and Projected Fossil Fuel Use. Time series of fossil fuel usage from 1990 to 2100 for K&L 2018 parameters (historical until 2018, projections after 2018; shaded), the IEA historical data (up to 2023; solid), and projections using updated initial conditions (Table 4.2) and growth parameters (Table 4.3) from 2023 forward (dashed).

Initial Conditions [EJ]			
Fuel	K&L (2018)	ANP (2023)	Difference (ANP - K&L)
Natural Gas	93	95	2
Coal	75	90	15
Oil	181	174	-7
Total Final Energy	414	431	17

Table 4.2: Fossil Fuel Initial Conditions. The initial demand in each fossil fuel source and total final energy for K&L and ANP. The K&L model begins in 2018, therefore the initial energy demand stems from 2018. The initial conditions for ANP are for 2023. The change in initial fuel demand (difference between ANP and K&L) is in the third column.

	γ			δ		
Fuel Source	K&L	ANP	K&L - ANP	K&L	ANP	K&L - ANP
Natural Gas	2.8	0.83	1.97	-1.7 to -0.3	-0.3	-1.67 to -0.27
Coal	-2	2.35	-4.35	-1.7 to -0.3	-0.39	-1.31 to 0.09
Crude Oil	1.8	0.25	1.35	-1.7 to -0.3	-0.18	-1.52 to -0.12

Table 4.3: Fossil Fuel Growth Parameters. The γ (%/year) and δ (%/%/year) parameters from K&L and updated fossil fuel parameters (labeled ANP) from 2023 IEA data (See the Data Availability section below).

4.3 Results & Discussion

4.3.1 Temperature & Changes of Avoiding 1.5°C Warming

K&L assumes that any scenario which hits 580 $GtCO_2$ by 2100 will reach the same final warming. In Figure 4.6c, the cumulative CO_2 in many scenarios reaches a value below 580 $GtCO_2$. K&L tuned their scenarios to reach a 580 $GtCO_{2e}$ budget; however, non-CO_2 emissions don't cumulatively add to warming in the same way as CO_2. When non-CO_2 gases are not included in cumulative CO_2 calculations, the result is Figure 4.6c. Note, that in Table 4.1, the cumulative emissions calculation including CH_4 is closer to 580 $GtCO_2$ than the cumulative emissions calculation without non-CO_2 gases.

I find that when implementing the 6,729-member FaIR ensemble with the 17 K&L scenarios, the 68% confidence interval of the final temperatures is 1.05 to 1.60 K (Table 4.1, Figure 4.6). The ensemble-mean final temperatures have a standard deviation of 0.05K across scenarios. The coldest scenarios are Extreme, Utopian, and Dec-Extreme-NoNNE at 1.28 ± 0.26K, closely followed by IPCC-NoNNE (1.28 ± 0.25) and Strong, Dec-Extreme, and IPCC (1.29 ± 0.26K). Thus, the coldest scenarios are those with the fastest rate of renewables growth and minimal (or zero) negative emissions technologies. In contrast, the hottest scenario is Moderate-FullNETs at 1.49 ± 0.31K, a scenario with slow renewables growth and high rates of negative emissions technologies. Furthermore, FullNET scenarios are always

hotter than their default or NoNNE counterparts by 0.06 ± 5x10^{-3}K (Degrowth-FullNETs – Degrowth-NoNNE) to 0.19 ± 0.1K (Moderate-FullNETs – Moderate-NoNNE) and are less likely to avoid 1.5°C warming by 6.9% to 23.3%, respectively (Table 4.1). Therefore, despite hitting the same carbon budget, dependence on negative emissions technologies is correlated with higher temperatures. Hotter final temperatures due to negative emissions technologies likely arise from a delay in phasing out fossil fuels.

However, the 17 K&L scenarios don't reach the same final CO_2 budget; their final cumulative CO_2 budgets range from 385 to 532 $GtCO_2$. Therefore, if the variability in final temperature across scenarios is due to variability in final carbon budget, then the final temperatures would correlate with final cumulative CO_2. However, I find that the final temperatures are more correlated with the maximum cumulative CO_2 ($r^2 = 0.14$) than the final cumulative CO_2 ($r^2 = 0.80$; Figure 4.10). This implies that overshoot scenarios (scenarios which exceed and return to 580$GtCO_2$) are not equivalent to scenarios which never exceed 580$GtCO_2$.

In Section 4.2.4, I found that natural gas and coal use between 2018 and 2023 was larger than projected by KLIAM. Given the result that scenarios which delay phasing out fossil fuels (the FullNET scenarios) result in larger 2100 temperatures and lower chances of avoiding 1.5°C warming, I hypothesize that running KLIAM on 2023 values (which would involve updating the initial conditions and growth parameters for 2023 as well as tuning the scenario delta parameters to the 2023 carbon budget) will result in warmer temperature projections.

4.3.2 Reversibility of Negative Emissions Technologies

The linearity of temperature anomaly with cumulative carbon emissions is a necessary construction for estimating transient climate response to emissions and the remaining carbon budget to avoid a given warming target. If this linearity is independent of the scenario (the emissions or cumulative emissions pathway), then I expect that overshoot scenarios (where emissions exceed the carbon budget and then return to that budget using negative emissions) to reach the same final temperature as a scenario which hits but never exceeds the carbon

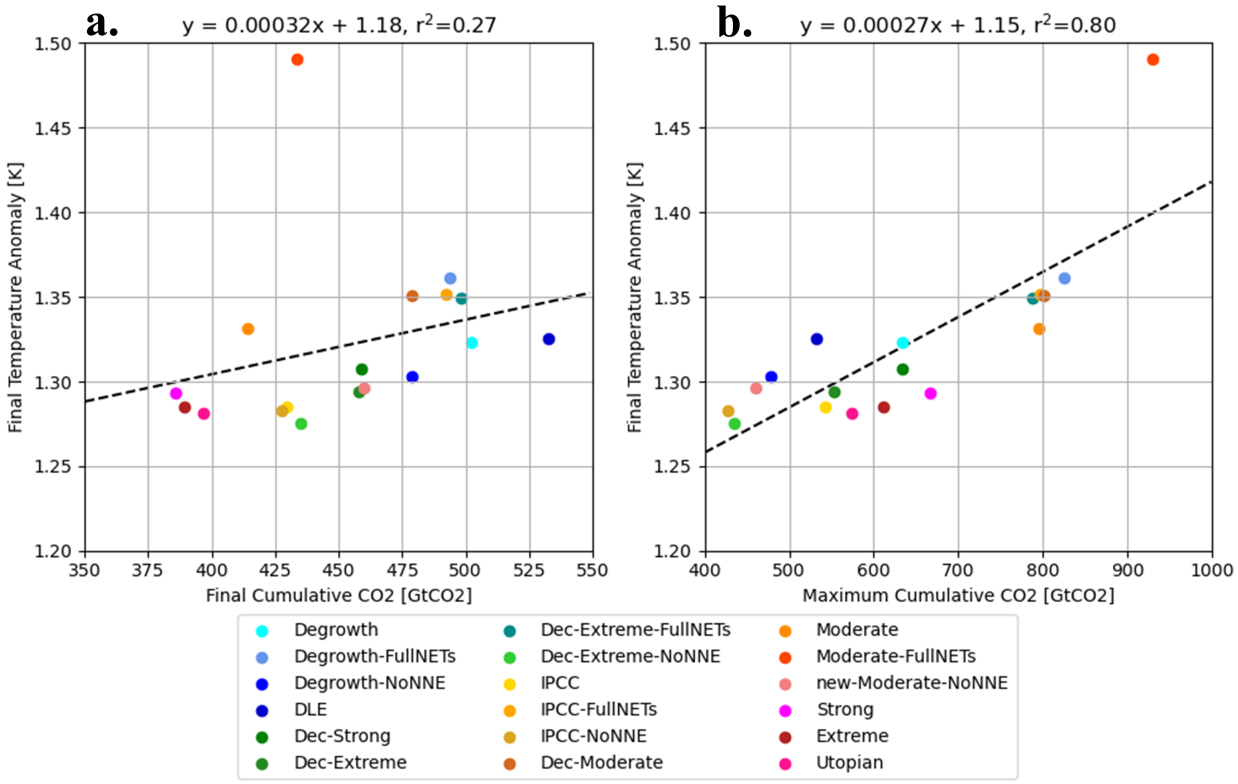

Figure 4.10: Correlation Between Final Temperature and Cumulative Emissions. A linear regression of the 17 K&L scenario final temperatures against (a) final and (b) maximum cumulative CO_2.

budget. However, in both the new and old parameter sets, I find that the "FullNET" ("overshoot") scenarios are always warmer (due to delaying fossil fuel phase out) and have a lower chance of avoiding 1.5°C warming than their analogous "NoNNE" ("low cumulative" emissions, henceforth referred to as "low") scenarios.

This suggests that there are limits to the linearity of temperature anomaly to cumulative CO_2 emissions. These limits could be due to time lag (i.e., eventually an overshoot scenario will reach the temperature of a low emissions scenario, but on longer timescales than present day to 2100), the zero emissions commitment (i.e., the Earth system may warm or cool after reaching net-zero emissions), non-CO_2 emissions (i.e., non-CO_2 emissions warm the Earth system but their relationship with the carbon budget is uncertain), or that TCRE has some dependence on the scenario (i.e., the Earth system cools on a different slope than it warms).

To understand the extent to which negative emissions can cool the Earth system after exceeding a given carbon budget, I consider four groups of scenarios, Degrowth, Dec-Extreme, IPCC, and Moderate, which have both FullNET and NoNNE scenarios (henceforth, called "overshoot" and "low") already available. I created new scenarios called "high cumulative emissions" or "high" which reach the same maximum cumulative CO_2 as the overshoot scenario but maintain that cumulative CO_2 until 2100 (rather than capturing and sequestering it, as in the overshoot scenario). As above, the "low cumulative emissions" or "low" scenario is the NoNNE scenario. The emissions, cumulative emissions, and temperature timeseries for the three emissions pathways across four scenarios (12 total) are plotted in Figure 4.11. Using these three emissions pathways, I define the efficiency of negative emissions (E) as:

$$E_1(t) = \frac{T_{High}(t) - T_{Overshoot}(t)}{T_{High}(t) - T_{Low}(t)} \times 100\% \quad (4.8)$$

where T is the timeseries of temperature for the high emissions, overshoot, and low emissions pathways. We can conceptualize the denominator as the warming caused by exceeding the carbon budget. In contrast, we can conceptualize the numerator as the cooling caused by negative emissions. Thus, for E = 100%, T_{Low} would have to equal $T_{overshoot}$. E_1 is plotted against time in Figure 4.12a and the frequency of E_1 values at 2100 is plotted in Figure 4.12d. This efficiency metric, E, is a measure of reversibility; in this subsection, the terms

efficiency of negative emissions and reversibility will be used interchangeably.

At 2100, the mean reversibility across all four scenarios is 64% with a 68% CI of 58% to 70%. Degrowth is the most reversible scenario, with an ensemble mean efficiency of 70%, whereas Dec-Extreme is the least reversible at 60%. None of the 6729 ensemble members reach 100% reversibility by 2100. Not only do negative emissions technologies not fully reverse warming done by exceeding the carbon budget by 2100, but there is also significant scenario variability. As in, the scenario to 580 $GtCO_2$ (when negative emissions are introduced, the rate of negative emissions, and how much is cumulatively taken up by negative emissions) may play a role in how well negative emissions technologies reverse warming on these timescales (approaching 2100). In Table 4.4, I extrapolate the ensemble mean efficiency to find the year when 100% efficiency is reached. I use a least squares linear regression over the last 40 years of data. There are caveats to this method because efficiency may asymptote approaching 100% and I only use the ensemble means. I find that the scenarios reach 100% efficiency between 2115 (Degrowth) and 2127 (Dec-Extreme), or approximately 15 to 27 years after our climate target of 2100. However, because these scenarios don't all reach net-zero at the same time (for example, Degrowth and Dec-Extreme reach net-zero before Moderate). Therefore, next I will consider efficiency over time since net-zero.

Equation 4.8 can become,

$$E_2(t') = \frac{T_{High}(t') - T_{Overshoot}(t')}{T_{High}(t') - T_{Low}(t')} \times 100\% \quad (4.9.1)$$

where t' is the time after net-zero. Note that each experiment (high, low, and overshoot) could hit net-zero at different times as well. In fact, high and overshoot reach net-zero at the same time in all scenarios, but low reaches net zero 2 to 18 years earlier.

$$E_2(t') = \frac{T_{High}(t'_2) - T_{Overshoot}(t'_2)}{T_{High}(t'_2) - T_{Low}(t'_1)} \times 100\% \quad (4.9.2)$$

where

$$t'_1 \leq t'_2$$

.

Equation 4.9 has the added benefit of accounting for ZEC. Once each scenario reaches net-zero, there is some temperature change (for this FaIR ensemble it is slightly negative: -0.02 K $\pm$ 0.07 K 40 years after net-zero) unrelated to the negative emissions (or lack thereof). Therefore, our overshoot scenarios could be cooling both due to negative emissions and due to ZEC. Since the low experiment reaches net-zero earlier (and because ZEC is a time dependent value), the temperature change due to ZEC at 2100 will be different than in the high and overshoot experiments. By normalizing for time after net-zero, this effect is removed.

ZEC can be estimated through a flat10 experiment where 10 PgC is emitted per year for 100 years (1000 Pg cumulative carbon) and then stops (Sanderson et al., 2024); ZEC is the temperature t' years after emissions cease. It is unknown whether or not ZEC has a dependence on the amount of cumulative emissions. The experiment used to calculate ZEC reaches a cumulative CO_2 which is much greater than the scenarios in this chapter. Future work could estimate ZEC across a variety of cumulative emissions scenarios to better remove it from the efficiency calculations.

E_2 is plotted against time since net-zero in Figure 4.12b and the frequency of E_2 values is plotted in 4.12e. At 2100 (which is 38 to 41 years after net-zero), the mean reversibility across all four scenarios is 65% with a 68% CI of 56% to 74%. Degrowth remains the most reversible scenario, with an ensemble mean efficiency of 68%. The variability in reversibility increases for E_2 (when compared to E_1), approximately doubling in IPCC. Dec-extreme saw the smallest increase in variability because the time of net-zero for the high and low experiments only differs by 2 years. Additionally, the ensemble mean efficiency decreased across all scenarios. In contrast to E_1, some ensemble members do reach 100% by 2100: 47 ensemble members (0.7%) in IPCC reach 100% efficiency. When I extrapolate toward 100% efficiency, I find that it takes 56 to 68 years after net-zero to reach 100% efficiency. As in, reversing warming due to exceeding the carbon budget occurs on decadal time scales. Thus, these results are consistent with E_1: 99.8% of ensemble members do not fully reverse warming by 2100, and there exists variability in reversibility across scenarios. Additionally, accounting for ZEC introduces new uncertainty.

Though these scenarios are meant to be constrained by the 2018 580 $GtCO_2$ carbon budget, not every overshoot experiment returns to 580 $GtCO_2$ by 2100. Therefore, some scenarios may have a lower efficiency due to having high cumulative emissions at 2100 in the overshoot experiment in comparison to the low experiment. Figure 4.12c shows:

$$E_{Cumulative\ CO2} = \frac{I_{High} - I_{Overshoot}}{I_{High} - I_{Low}} \times 100\% \quad (4.10)$$

where I is cumulative CO_2. Equation 4.10 reaches 100% when the overshoot experiment has the same cumulative CO_2 as the low experiment. A value of less than 100% at 2100 shows that the overshoot experiment did not return to 580 $GtCO_2$ during the model runtime. Future work could extend the model runtime until the overshoot scenarios have reached 580 $GtCO_2$ or until 100% efficiency if reached. Additionally, the table in Figure 4.12f shows how much CO_2 was cumulatively removed and the maximum rate of carbon removal. Future work could explore how the rate of negative emissions and cumulative negative emissions impacts reversibility.

To better understand why reversibility is not 100% in the scenarios, the ensemble mean TCRE for each of the four scenarios is plotted in Figure 4.13. For Degrowth, the overshoot scenario nearly reaches the same cumulative emissions as the low scenario, but at a higher temperature. For Moderate, the scenario cools at a distinctly shallower slope while cooling, indicating that more emissions need to be removed than were emitted to achieve the same magnitude of cooling as warming. IPCC and Dec-Extreme are further from reaching the same final cumulative emissions, but similar to Degrowth, these scenarios are approaching a warmer temperature at the same cumulative emissions as the low scenario. In each case, additional CO_2 may need to be removed to reach 100% reversibility. Additionally, the ZEC observed in each scenario (the temperature change occurring without a change in cumulative emissions, as in, where the plotted line is vertical) is not the same. Notable, ZEC appears to be positive in the Moderate high scenario (while ZEC is negative in all other scenarios). This may indicate that ZEC has some scenario dependence.

In summary, it is unlikely that any of the modeled decarbonization pathways will reach 100% efficiency (fully reversing warming due to exceeding the carbon budget) before 2100.

Under mean physical parameters, without adjusting for ZEC, and under a low-energy demand decarbonization pathway, one can expect to reach 100% reversibility from negative emissions technology by 2115, 15 years after our climate target. When normalizing for ZEC and under a high-energy demand decarbonization pathway, one can expect to reach 100% reversibility through negative emissions technologies by 68 years after net-zero emissions are reached. Under the high-energy demand scenario (Moderate), 518 $GtCO_2$ are taken up over less than 40 years to achieve 0.34 K cooling (2100 temperature difference between the high cumulative emissions and overshoot experiments). In contrast, the low-energy demand scenario (Degrowth) has the highest reversibility and the shortest time to fully reverse warming due to exceeding the carbon budget. Reaching 100% efficiency depends on globally scalable carbon capture technologies which may stress planetary boundaries, food and water systems, and worsen existing colonial and wealth inequalities (Heck et al., 2018; Hasegawa et al., 2015; Hickel and Slamersak, 2022; Anderson and Peters, 2016; Andreoni et al., 2024).

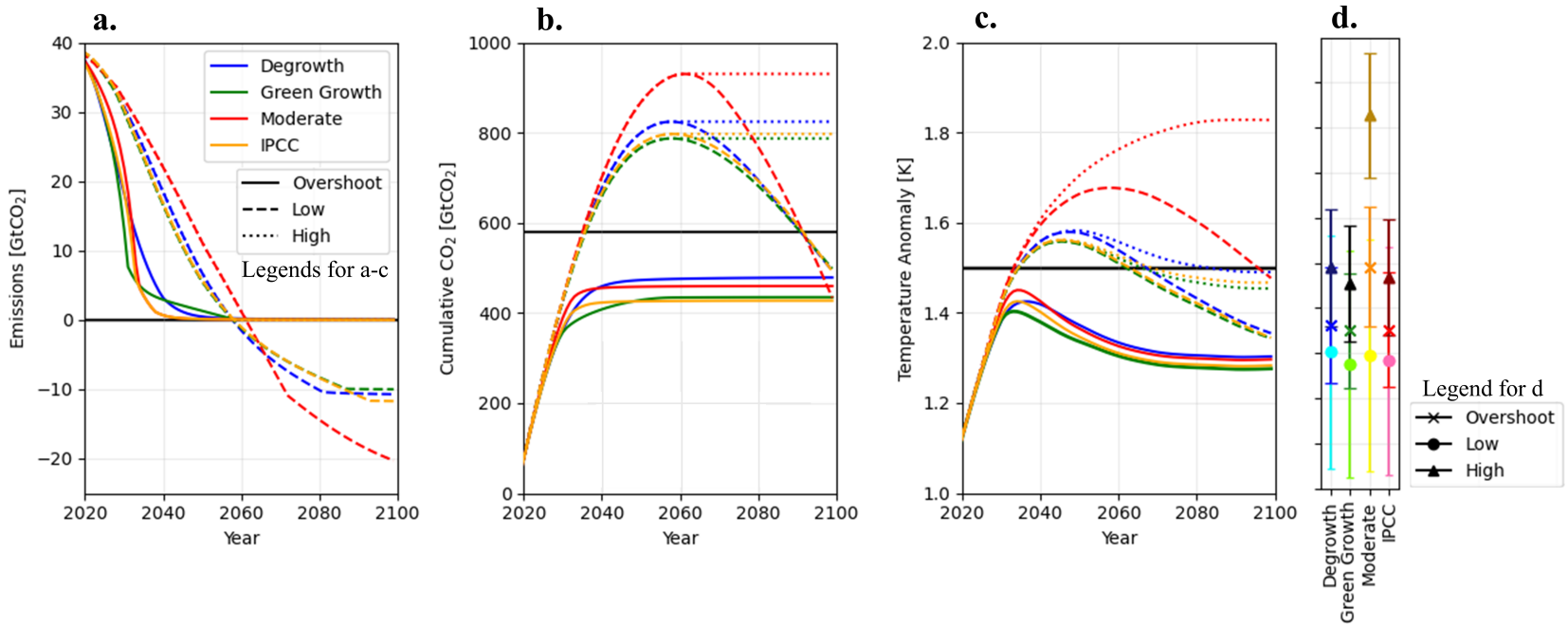

Figure 4.11: The High, Low, and Overshoot Scenarios. (a-c) The (a) emissions, (b) cumulative emissions, and (c) temperature of the High (dotted), Low (dashed), and Overshoot (solid) experiments for Degrowth (blue), Dec-Extreme (green), IPCC (yellow), and Moderate (red). (d) The temperature variability across the ensemble members for the High (ˆ), Low (o), and Overshoot (x) experiments and all four scenarios.

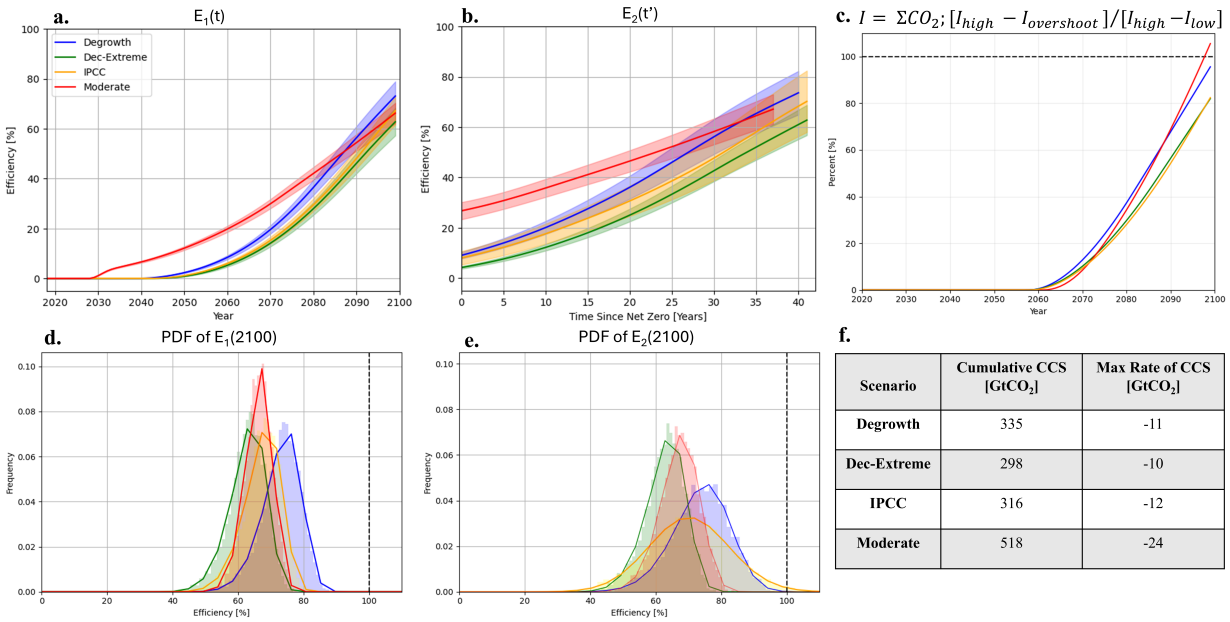

f.

Scenario	Cumulative CCS [$GtCO_2$]	Max Rate of CCS [$GtCO_2$]
Degrowth	335	-11
Dec-Extreme	298	-10
IPCC	316	-12
Moderate	518	-24

Figure 4.12: Timeseries and Frequency of Negative Emissions Technology Efficiency. E_1, as defined by equation 4.8, plotted against absolutely time (2020 to 2100). (b) E_2, as defined by equation 4.9, plotted against time since net zero. The shaded regions represent 1 σ from the ensemble mean (solid). (c) Equation 4.10 plotted against absolute time. The probability distribution function of (d) E_1 and (e) E_2 at 2100. (f) A table of the cumulative carbon capture and storage and the maximum rate of CCS for the four scenarios: Degrowth, Dec-Extreme, IPCC, and Moderate. The gray dashed lines indicate the 1.5°warming target and the 580 $GtCO_2$ carbon budget.

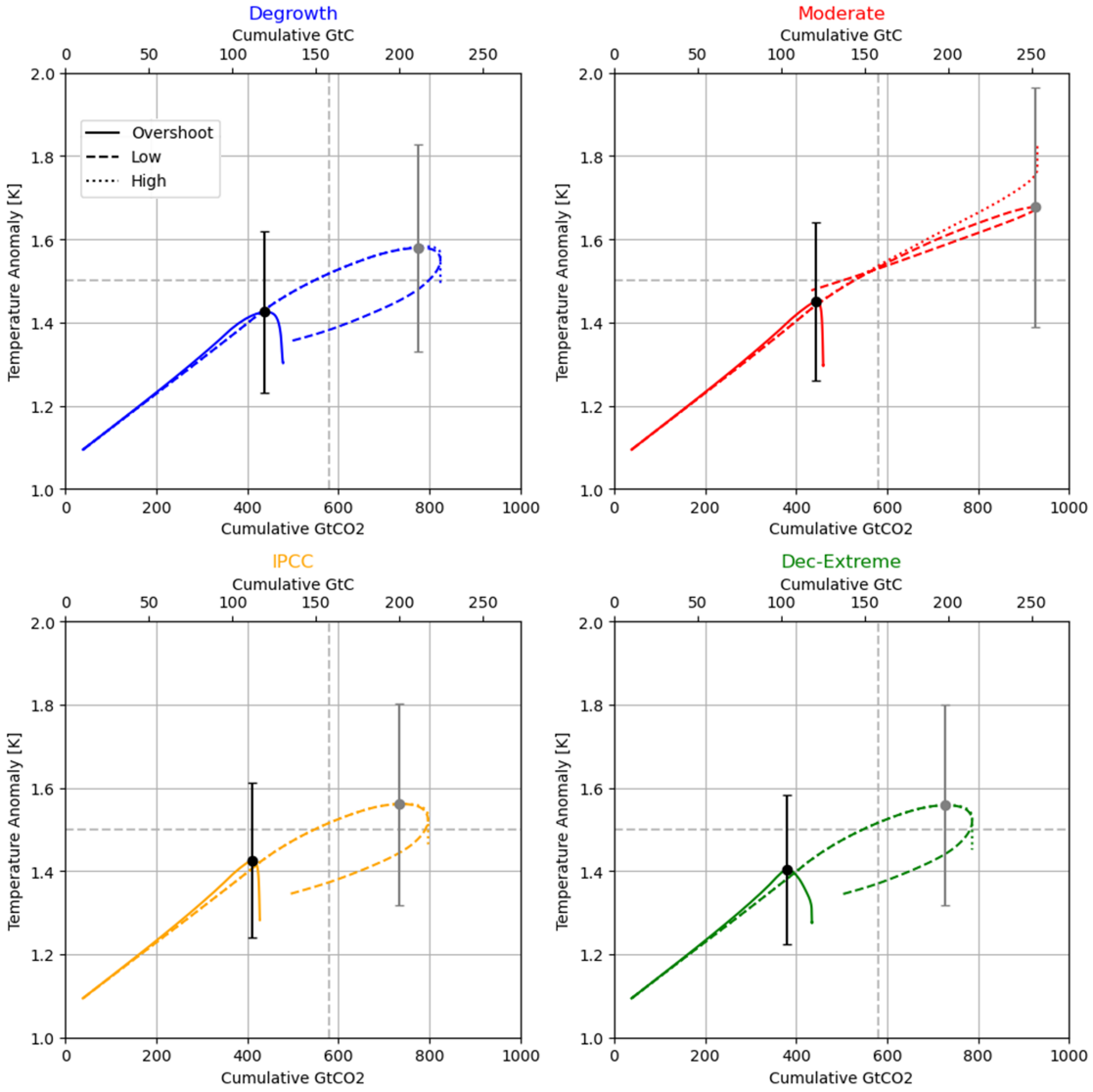

Figure 4.13: The Transient Climate Response to Emissions. The temperature anomaly [K] plotted against cumulative CO_2 emissions in GtC (upper axis) and $GtCO_2$ (lower axis) for Degrowth (blue, upper left), Moderate (red, upper right), IPCC (yellow, lower left), and Dec-Extreme (green, lower right). The low cumulative emissions (solid), overshoot (dashed), and high cumulative emissions (dotted) are plotted for each scenario. The maximum temperature and 1 σ variability are marked for low (black) and overshoot (gray).

4.4 Conclusions

As of 2024, the remaining carbon budget is only 235 $GtCO_2$ for a 50% chance of limiting warming to 1.5°C (Friedlingstein et al., 2025). As the remaining carbon budget decreases, it is essential to understand how the pathways to net-zero impact temperature. This chapter investigates whether scenarios reaching the same carbon budget would produce the same temperature results. I found that when the 17 K&L scenarios (run from 2018 to 2100) reach 580 $GtCO_2$ final temperature exhibits variability. In particular, scenarios which depended on negative emissions technologies were always hotter (with a lower chance of avoiding 1.5°C) than similar scenarios. This suggests a potential breakdown in the linearity of the transient climate response to emissions, the relationship between temperature anomaly and cumulative carbon emissions.

I introduced a reversibility metric called the negative emissions technology efficiency and find a time lag wherein negative emissions technologies cannot cool all excess warming due to exceedance by 2100 within most (if not all) FaIR ensemble members. Uncertainty in the efficiency of negative emissions technologies comes from variability in the scenarios as well as variability in the transient climate response to emissions and the zero-emissions commitment (ZEC). Calculating the efficiency of negative emissions technologies as a function of time since net-zero accounts for temperature change due to ZEC but also increases uncertainty, particularly for the high energy demand scenarios: IPCC and Moderate. A better understanding of how the zero emissions commitment impacts temperature in negative emission simulations is crucial to reducing uncertainty in the reversibility of warming. Scenario variability in reversibility suggests that the timing of emissions, the amount of cumulative emissions, or magnitude of warming overshoot may impact reversibility of said warming. Future work could explore which climate and scenario parameters most impact the reversibility of warming. Reversibility of warming due to exceedance may be reversible, but on decadal time scales with between 200 and 520 $GtCO_2$ of cumulatively stored emissions. Thus, overshoot scenarios trade human well-being during decades of warming beyond our climate target for the disproportionately high energy demand per capita in wealthy nations - warming which can only be reversed by heretofore fictional technologies operating on the 100 $GtCO_2$ scale.

Ultimately, I found that not only is 100% efficiency unlikely among most scenarios and ensemble members, but the uncertainty in reversibility is large enough that responsible climate policy cannot and should not depend upon it.

These results are consistent with overshoot literature which finds that the Earth system does not behave identically during periods of warming and CO_2 emissions compared to periods of cooling and negative emissions, especially in high overshoot scenarios (300 GtC or 1,100 $GtCO_2$ over the carbon budget; (Tokarska et al., 2019; Zickfeld et al., 2021). Notably, this work finds that overshoot scenarios between 298 and 518 $GtCO_2$ (81 to 141 GtC) also exhibit asymmetry in cooling versus warming. Additionally, the climate impacts of CO_2 removal may have spatial variability due to changes in ocean circulation, particularly the Atlantic Meridional Overturning Circulation (Schwinger et al., 2022). In conclusion, my results agree with Zickfeld et al. (2023) that decreasing emissions, rather than depending on negative emissions technologies, is the best pathway to avoiding 1.5°C warming.

Across all scenarios, low energy demand scenarios with high rates of renewable growth are the most likely to avoid 1.5°C (or 2°C) warming. Scenarios which maintain increasing energy demand year-to-year with high chances of avoiding 1.5°C warming depend on a high rate of renewable energy growth or rapid development of negative emissions technologies. If renewable energy sources fail to grow at those rates, low-energy demand scenarios such as Degrowth successfully limit warming with the highest rate of warming reversibility. However, low-energy demand scenarios were not included in the CMIP6 SSP framework. The next phase of CMIP must consider low-energy demand scenarios as viable decarbonization pathways in order to prioritize equity, feasibility, and human well-being.

Data Availability

Listed below are all of the datasets used in Chapter 4.

1. EI Statistical Review of World Energy. (2024). Energy institute statistical review of world energy 2023. *Energy Institute*.

2. Emissions Database for Global Atmospheric Research (EDGAR): Crippa, M., Guizzardi, D., Pagani, F., et al. (2023) GHG emissions of all world countries, *Publications Office of the European Union, Luxembourg,* doi:10.2760/953322, JRC134504.

3. IEA, World Energy Balances, IEA, Paris https://www.iea.org/data-and-statistics/data-product/world-energy-balances, Licence: Terms of Use for Non-CC Material. *Accessed June 2025*

4. IEA, Renewables 2024 Dataset, IEA, Paris https://www.iea.org/data-and-statistics/data-product/renewables-2024-dataset, Licence: Terms of Use for Non-CC Material

5. International Energy Agency (2023), Methane Tracker Database, IEA, Paris. License: Creative Commons Attribution CC BY 4.0.

6. SSP Public Database Version 2.0: Riahi, K., Van Vuuren, D. P., Kriegler, E., et al. The Shared Socioeconomic Pathways and their energy, land use, and greenhouse gas emissions implications: An overview, Global Environmental Change, Volume 42, Pages 153-168, 2017, ISSN 0959-3780, DOI:110.1016/j.gloenvcha.2016.05.009. Accessed at https://tntcat.iiasa.ac.at/SspDb/dsd

				2100	30-35 Years after Net Zero	Absolute Time	Time Since Net-Zero
Scenario	**Final Temperature [K]**	**Year of Net Zero**	**Magnitude of Overshoot [$GtCO_2$]**	$E_1(t)$	$E_2(t')$	**t**	**t'**
Degrowth-FullNETs	1.36 ± 0.28	2060	433	**69.5% ± 5.6%**	**67.2% ± 8.0%**	**2115**	**56 years**
Degrowth-NoNNE	1.30 ± 0.26						
Degrowth-PeakCO2	*1.49 ± 0.30*						
Dec-Extreme-FullNETs	1.35 ± 0.28	2059	331	59.2% ± 5.2%	53.9% ± 5.2%	2127	67 years
Dec-Extreme-NoNNE	1.28 ± 0.26						
Dec-Extreme-PeakCO2	*1.45 ± 0.29*						
IPCC-FullNETs	1.35 ± 0.28	2059	357	63.0% ± 5.3%	60.2% ± 10.8%	2121	62 years
IPCC-NoNNE	1.28 ± 0.25						
IPCC-PeakCO2	*1.47 ± 0.30*						
Moderate-FullNETs	1.49 ± 0.31	2062	512	63.6% ± 3.9%	65.8% ± 5.7%	2125	68 years
Moderate-NoNNE	*1.30 ± 0.26*						
Moderate-PeakCO2	*1.83 ± 0.38*						
			68% CI	57.6 to 70.1%	56.0% to 74.3%	2115 to 2127*	56 to 68 years*

Table 4.4: Comparison of Efficiency at 2100 and 30-35 years after net-zero. The final temperature, the year of net-zero (in the overshoot run), magnitude of overshoot (or the maximum cumulative CO_2 in the overshoot and high emissions runs), the efficiency parameter with ZEC and TCRE corrections for 2100 or 30-35 years after Net Zero, and the time to reach 100% efficiency in absolute time and time since net-zero. New experiments are italicized. The highest efficiency and earliest time of 100% efficiency are bolded. (*) Denotes the range of values across scenarios rather than the confidence interval.

Chapter 5
CONCLUSIONS

A World Meteorological Organization Report estimates that 2025 warming could reach 1.55 ± 0.13°C. Therefore, 2025 could become the first year to exceed 1.5°C warming. Thus far, scientists' warnings on the human cost of climate change have gone unheeded as nations repeatedly miss deadlines to submit updated Nationally Defined Commitments to reduce CO_2 emissions (Weikmans et al., 2021; Dunne, 2025), commitments which were already insufficient to limit warming to "well below 2°C" (den Elzen et al., 2022; Liu and Raftery, 2021; UNFCCC, 2015). Affluence – wealth, income, and energy inequality – is a leading driver of climate change (Wiedmann et al., 2020), one few scientists and policymakers are poised to challenge. SSP5, fossil fueled development, reveals the climatological consequences of warming beyond the Paris Agreement, as seen in Chapter 2. Present day warming has already worsened existing inequalities, such as access to clean, affordable, and safe energy to power climate control appliances, as described in Chapter 3. In refusing to constrain affluence in climate modeling, our climate models depend on fictitious emission-negative energy sources, which may not even reverse warming, as described in Chapter 4. The dependence of negative emissions technologies in the SSP storylines in CMIP6, the largest modeling intercomparison project, reveals that we aim to limit warming at the cost of worsening wealth and colonial inequalities (Hickel and Slamersak, 2022). It is not and will never be scientific to model only climate futures that refuse to reduce the main driver of warming: indefinite consumption by those most wealthy.

Future work in this field must consider growth agnostic scenarios, removing GDP growth as a necessary constraint. Milward-Hopkins et al. (2020) finds that global energy demand can be greatly reduced while providing a materially generous and sufficient living for all people. Yet, the Keysser & Lenzen integrated assessment model is one of few IAMs without GDP growth as a constraint, but the model is limited compared to those used in the SSP

scenarios. More sophisticated IAMs which model across several regions and the emissions pathways of gases beyond CO_2 and CH_4 (such as N_2O or short-lived pollutants) are required to better understand the climate under a just transition to renewable energy. Additionally, my analysis could be repeated with the newest version of FaIR (v2.0) (Leach et al., 2020) and its constrained ensemble to produce more accurate and precise temperature projections. Ultimately, FaIR, while an accessible climate model, does not properly model the interactions between the ocean, land and atmospheric carbon, which limits our understanding of how the Zero Emissions Commitment impacts warming reversibility (Leach et al., 2020; Séférian et al., 2024; Shum, 2024).

Future analysis should model overshoot scenarios with more sophisticated, emissions-driven models. Importantly, overshoot scenarios should not be studied in isolation of socio-economic pathways. In Chapter 4, I found that scenarios with different pathways toward warming overshoot exhibit variability in warming reversibility. Thus, I urge the next era of model intercomparison to include degrowth scenarios, overshoot scenarios, and emissions-driven models within the shared socio-economic pathway experiments. As we approach 2°C warming, the results from Chapter 4 remain true: the pathway to limiting warming requires rapid cessation of fossil fuel use and a decrease in energy demand in wealthy regions, to provide sufficient living and a habitable climate for all.

ACKNOWLEDGMENTS

I am incredibly thankful to everyone who helped bring this dissertation to fruition. First, I'd like to thank my advisor, Professor Dargan Frierson, whose knowledge of atmospheric dynamics and passion for environmental justice provided me with an unparalleled education. Next, I'd like to acknowledge my committee: Professors Abby Swann, Robert Wood, Dennis Hartmann, and Bethany Gordon. Abby and Rob provided me with, not just an interdisciplinary knowledge base, but also professional and emotional support as I completed my doctoral education. Dennis taught the first class I took in the UW Atmospheric and Climate Science Department with such dedication that I proceeded to take every one of the courses he offered. Now at this final stage, I am so honored to have had him along the entire journey. Next, I'd like to thank Bethany who joined my committee as my Graduate Student Representative and who went above and beyond her role to support me this past year. Outside of my doctoral committee, I'd also like to thank Professor Kyle Armour who served on my master's committee and provided invaluable to my master's project. Finally, I'd like to thank Professor Kat Huybers. I worked as a teaching assistance under Kat in my last quarter as a graduate student. Nearly everyday on our walk to lecture, she would make sure to check in on me and my progress toward graduating. I learned so much working under her that made a world of difference.

Without the support of my family and friends, this dissertation would not be here. I'd like to thank my graduate cohort who created such an accepting community in my first several years as a graduate student. In particular, Travis Aerenson, Molly Wieringa, and William Henshaw who are co-authors on Chapter 2 (Poletti et al., 2024a). As well as Ursula Jongebloed, Pedro Angulo-Umana, Aodhan Sweeney, and Kaitlyn Confer who were close friends to me in and outside of the office. I'd like to thank my family: my mom, my brother, and my twin who provided me with unconditional love and support. Finally, I'd like to thank my spouse, Jake. I've known Jake since I started college in 2015, and I can't imagine

a better partner. I couldn't have completed this journey without Jake, our cat Frank, and our dog Bao. I am so honored to have taken this journey with so many kind, intelligent, and wonderful people.

This work was funded through several grants and fellowships including: The National Science Foundation (Grant AGS-1665247), The UW Provost Fellowship, The UW Future Rivers Fellowship, and The UW Program on Climate Change Graubard Fellowship.

BIBLIOGRAPHY

Aerenson, T., Marchand, R., Chepfer, H., and Medeiros, B. (2022). When will MISR detect rising high clouds? *Journal of Geophysical Research: Atmospheres*, 127:2021 035865.

Anderson, K. and Peters, G. (2016). The trouble with negative emissions. *Science*, 354:182–183.

Andreoni, P., Emmerling, J., and Tavoni, M. (2024). Inequality repercussions of financing negative emissions. *Nature Climate Change*, 14:48–54.

Archer, D. (2016). *The Long Thaw: How Humans Are Changing the next 100,000 Years of Earth's Climate*. Princeton University Press.

Armour, K. C., Siler, N., Donohoe, A., and Roe, G. H. (2019). Meridional Atmospheric Heat Transport Constrained by Energetics and Mediated by Large-Scale Diffusion. *Journal of Climate*, 32(12):3655–80.

Baker, H., Millar, R., Karoly, D., and Beyerle, U. (2018). Higher CO2 Concentrations Increase Extreme Event Risk in a 1.5 °C World. *Nature Climate Change*, 8:604–608.

Balk, G. (2018). Seattle is least air-conditioned metro area in the U.S. So how do locals keep cool? *Seattle Times*.

Barnes, E. and Hartmann, D. (2012). Detection of Rossby wave breaking and its response to shifts of the midlatitude jet with climate change. *Journal of Geophysical Research Atmospheres*, page 117 9.

Bartusek, S., Kornhuber, K., and Ting, M. (2021). North American Heatwave Amplified by Climate Change-Driven Nonlinear Interactions. *Nature Climate Change*, 12:1143–1150.

Bathiany, S., Notz, D., Mauritsen, T., Raedel, G., and Brovkin, V. (2016). On the Potential for Abrupt Arctic Winter Sea Ice Loss. *Journal of Climate*, 29(7):2703–2719 10 1175 – –15–0466 1.

Beall, R. and McNary, B. (2022). Nearly 90% of U.S. households used air conditioning in 2020 - U.S. Energy Information Administration (EIA). https://www.eia.gov/todayinenergy/detail.php?id=52558.

Bloch-Johnson, J., M., R., and DS, A. (2020). Spatial Radiative Feedbacks from Internal Variability Using Multiple Regression. *Journal of Climate*, 33(10):4121–4140.

Bloch-Johnson, J., Rugenstein, M., Stolpe, M., Rohrschneider, T., Zheng, Y., and Gregory, J. (2021). Climate sensitivity increases under higher CO2 levels due to feedback temperature dependence. *Geophysical Research Letters*, 48:2020 089074.

Bodas-Salcedo, A., Webb, M., Bony, S., Chepfer, H., Dufresne, J., and Klein, S. (2011). COSP: Satellite simulation software for model assessment. *Bulletin of the American Meteorological Society*, 92:1023–1043.

Boucher, O., Servonnat, J., Albright, A., Aumont, O., Balkanski, Y., and Bastrikov, V. (2020). Presentation and Evaluation of the IPSL-CM6A-LR Climate Model. *Journal of Advances in Modeling Earth Systems*, 12(7):2019 002010.

Byrne, B. and Goldblatt, C. (2013). Radiative forcing at high concentrations of well-mixed greenhouse gases. *Geophysical Research Letters*, 41(1):152–160.

Byrne, M. P. and O'Gorman, P. A. (2016). Understanding Decreases in Land Relative Humidity with Global Warming: Conceptual Model and GCM Simulations. *Journal of Climate*, 29(24):9045–9061.

Byrne, M. P. and O'Gorman, P. A. (2018). Trends in Continental Temperature and Humidity Directly Linked to Ocean Warming. *PNAS*, 11(19):4863–4868.

Chemke, R., Polvani, L. M., and Deser, C. (2019). The Effect of Arctic Sea Ice Loss on the Hadley Circulation. *Geophysical Research. Letters*, 46(2):963–972.

Clark, P. U., Shakun, J., Marcott, S., Mix, A., Eby, M., and Kulp, S. (2016). Consequences of twenty-first-century policy for multi-millennial climate and sea-level change. *Nature Climate Change*, 6:360–369.

Clarke, B., Otto, F., Stuart-Smith, R., and Harrington, L. (2022). Extreme Weather Impacts of Climate Change: An Attribution Perspective. *Environmental Research: Climate*, 1(1).

Collins, M., Knutti, R., Arblaster, J., Dufresne, J. L., Fichefet, T., and Friedlingstein, P. (2013). Long-term Climate Change: Projections, Commitments and Irreversibility. In *Climate Change 2013: The Physical Science Basis. Contribution of Working Group I to the Fifth Assessment Report of the Intergovernmental Panel on Climate Change*. Cambridge University Press.

Cuaresma, J. C. (2017). Income projections for climate change research: A framework based on human capital dynamics. *Global Environmental Change*, 42:226–236.

Dai, A., Huang, D., Rose, B. E. J., Zhu, J., and Tian, X. (2020). Improved methods for estimating equilibrium climate sensitivity from transient warming simulations. *Climate Dynamics*, 54:4515–4543.

Damerau, K., Patt, A. G., and van Vliet, O. P. R. (2016). Water saving potentials and possible trade-offs for future food and energy supply. *Global Environmental Change*, 39:15–25.

den Elzen, M. G. J., Dafnomilis, I., Forsell, N., Fragkos, P., Fragkiadakis, K., Höhne, N., Kuramochi, T., Nascimento, L., Roelfsema, M., van Soest, H., and Sperling, F. (2022). Updated nationally determined contributions collectively raise ambition levels but need strengthening further to keep Paris goals within reach. *Mitigation and Adaptation Strategies for Global Change*, 27(5):33.

DenHerder-Thomas, T., Welle, J., Farrell, J., and McCoy, M. (2020). Equitable Community Solar: Policy and Program Guidance for Community Solar Programs that Promote Racial and Economic Equity. Technical report, Institution for Local Self-Reliance.

DOC, W. (2023). Low-Income Energy Assistance 2023 Legislative Report. Technical report, Washington State Department of Commerce.

Drehobl, A., Ross, L., and Ayala, R. (2020). How High are Household Energy Burdens? An Assessment of National and Metropolitan Energy Burden across the United States. Technical report, American Council for an Energy Efficient Economy (ACEEE).

Drijfhout, S., Bathiany, S., Beaulieu, C., and Swingedouw, D. (2015). Catalogue of abrupt shifts in Intergovernmental Panel on Climate Change climate models. *PNAS*, 112(42):5777–5786.

Dufresne, J. and Bony, S. (2008). An Assessment of the Primary Sources of Spread of Global Warming Estimates from Coupled Atmosphere-Ocean Models. *Journal of Climate*, 21(19):5135–44.

Dunne, D. (2025). Analysis: 95% of countries miss UN deadline to submit 2035 climate pledges.

Dvorak, M., Armour, K., Frierson, D., Proistosescu, C., Baker, M., and Smith, C. (2022). Estimating the timing of geophysical commitment to 1.5 and 2.0 C of global warming. *Nature Climate Change*, 12:547–552.

Ebi, K. and Hess, J. (2020). Health Risks Due To Climate Change: Inequity In Causes And Consequences. *Health Affairs Climate & Health*, 39(12).

EIA (2024). Washington State Profile and Energy Estimates. https://www.eia.gov/state/analysis.php?sid=WA.

Emanuel, K., Fantini, M., and Thorpe, A. (1987). Baroclinic instability in an environment of small instability to slantwise moist convection. Part I: Two-dimensional models. *Journal of Atmospheric Sciences*, 44:1559–1573.

Emmerling, J., Andreoni, P., and Tavoni, M. (2024). Global inequality consequences of climate policies when accounting for avoided climate impacts. *Cell Reports Sustainability*, 1(1).

Etminan, M., Myhre, G., and Highwood, E. J. (2016). Radiative forcing of carbon dioxide, methane, and nitrous oxide: A significant revision of the methane radiative forcing. *Geophysical Research Letters*, 43(24).

Eyring, V., Bony, S., and Meehl, G. (2016). Overview of the Coupled Model Intercomparison Project Phase 6 (CMIP6) experimental design and organization. *Geosci. Model Dev*, 9(5).

Fajardy, M., Morris, J., and Gurgel, A. (2021). The economics of bioenergy with carbon capture and storage (BECCS) deployment in a 1.5 °C or 2 °C world. *Global Environmental Change*, 68(102262).

Fan, X., Duan, Q., Shen, C., Wu, Y., and Xing, C. (2020). Global Surface Air Temperatures in CMIP6: Historical Performance and Future Changes. *Environmental Research Letters*, page 15.

F.A.O. (2024). Land statistics 2001–2022 – Global, regional and country trends. *FAOSTAT Analytical Briefs*, (88).

Flannery, B. (1984). Energy Balance Models Incorporating Transport of Thermal and Latent Energy. *Journal of the Atmospheric Sciences*, 41(3):414–21.

Forster, P., Smith, C., and Walsh, T. (2024). Indicators of Global Climate Change 2023: Annual update of key indicators of the state of the climate system and human influence. *Earth System Science Data*, 16(6).

Forster, P., Storelvmo, T., and Armour, K. (2021). The Earth's Energy Budget, Climate Feedbacks, and Climate Sensitivity. In *Climate Change 2021: The Physical Science Basis. Contribution of Working Group I to the Sixth Assessment Report of the Intergovernmental Panel on Climate Change*, pages 923–1054. Cambridge University Press.

Fox-Kemper, B., Hewitt, H., Xiao, C., Aalgeirsdóttir, G., and Drijfhout, S. (2021). Ocean, Cryosphere and Sea Level Change. In *Climate Change 2021: The Physical Science Basis. Contribution of Working Group I to the Sixth Assessment Report of the Intergovernmental Panel on Climate Change*, pages 1211–1362. Cambridge University Press.

Friedlingstein, P., Cox, P., and Betts, R. (2006). Climate–Carbon Cycle Feedback Analysis: Results from the C4MIP Model Intercomparison. *Journal of Climate*, 19(14):3337–3353.

Friedlingstein, P., O'Sullivan, M., and Jones, M. (2022). Global Carbon Budget 2022. *Earth Syst. Sci. Data*, 14:4811–4900.

Friedlingstein, P., O'Sullivan, M., Jones, M. W., Andrew, R. M., Hauck, J., Landschützer, P., Le Quéré, C., Li, H., Luijkx, I. T., Olsen, A., Peters, G. P., Peters, W., Pongratz, J., Schwingshackl, C., Sitch, S., Canadell, J. G., Ciais, P., Jackson, R. B., Alin, S. R., Arneth, A., Arora, V., Bates, N. R., Becker, M., Bellouin, N., Berghoff, C. F., Bittig, H. C., Bopp, L., Cadule, P., Campbell, K., Chamberlain, M. A., Chandra, N., Chevallier, F., Chini, L. P., Colligan, T., Decayeux, J., Djeutchouang, L. M., Dou, X., Duran Rojas, C., Enyo, K., Evans, W., Fay, A. R., Feely, R. A., Ford, D. J., Foster, A., Gasser, T., Gehlen, M., Gkritzalis, T., Grassi, G., Gregor, L., Gruber, N., Gürses, Ö., Harris, I., Hefner, M., Heinke, J., Hurtt, G. C., Iida, Y., Ilyina, T., Jacobson, A. R., Jain, A. K., Jarníková, T., Jersild, A., Jiang, F., Jin, Z., Kato, E., Keeling, R. F., Klein Goldewijk, K., Knauer, J., Korsbakken, J. I., Lan, X., Lauvset, S. K., Lefèvre, N., Liu, Z., Liu, J., Ma, L., Maksyutov, S., Marland, G., Mayot, N., McGuire, P. C., Metzl, N., Monacci, N. M., Morgan, E. J., Nakaoka, S.-I., Neill, C., Niwa, Y., Nützel, T., Olivier, L., Ono, T., Palmer, P. I., Pierrot, D., Qin, Z., Resplandy, L., Roobaert, A., Rosan, T. M., Rödenbeck, C., Schwinger, J., Smallman, T. L., Smith, S. M., Sospedra-Alfonso, R., Steinhoff, T., Sun, Q., Sutton, A. J., Séférian, R., Takao, S., Tatebe, H., Tian, H., Tilbrook, B., Torres, O., Tourigny, E., Tsujino, H., Tubiello, F., van der Werf, G., Wanninkhof, R., Wang, X., Yang, D., Yang, X., Yu, Z., Yuan, W., Yue, X., Zaehle, S., Zeng, N., and Zeng, J. (2025). Global carbon budget 2024. *Earth System Science Data*, 17(3):965–1039.

Frierson, D. (2006). Robust increases in midlatitude static stability in simulations of global warming. *Geophysical Research Letters*, 33:24816,.

Frierson, D. (2007). The Dynamics of Idealized Convection Schemes and Their Effect on the Zonally Averaged Tropical Circulation. *Journal of the Atmospheric Sciences*, 64:1959–1976.

Fuss, S. (2018). Negative emissions—Part 2: Costs, potentials and side effects. *Environmental Research Letters*, 13(6).

Gasparrini, A., Guo, Y., Sera, F., Vicedo-Cabrera, A. M., Huber, V., Tong, S., de Sousa Zanotti Stagliorio Coelho, M., Nascimento Saldiva, P. H., Lavigne, E., Matus Correa, P., Valdes Ortega, N., Kan, H., Osorio, S., Kyselý, J., Urban, A., Jaakkola, J. J. K., Ryti, N. R. I., Pascal, M., Goodman, P. G., Zeka, A., Michelozzi, P., Scortichini, M., Hashizume, M., Honda, Y., Hurtado-Diaz, M., Cesar Cruz, J., Seposo, X., Kim, H., Tobias, A., Iñiguez, C., Forsberg, B., Åström, D. O., Ragettli, M. S., Guo, Y. L., Wu, C.-f., Zanobetti, A., Schwartz, J., Bell, M. L., Dang, T. N., Van, D. D., Heaviside, C., Vardoulakis, S., Hajat, S., Haines, A., and Armstrong, B. (2017). Projections of temperature-related excess mortality under climate change scenarios. *The Lancet Planetary Health*, 1(9):e360–e367.

Giannini, A., Lyon, B., Seager, S., and Vigaud, N. (2018). Dynamical and thermodynamic elements of modeled climate change at the east African margin of convection. *Geophysical Research Letters*, 45:992–1000.

Good, P., Lowe, J. A., and Andrews, T. (2015). Nonlinear regional warming with increasing CO2 concentrations. *Nature Climate Change*, 5:138–142.

Graham, E. and Fulghum, N. (2024). Solar Power Continues to Surge in 2024. Technical report, Ember.

Gregory, J., Andrews, T., and Good, P. (2015). The inconstancy of the transient climate response parameter under increasing CO2. *Royal Society*.

Gregory, J. M., Ingram, W., Palmer, M., Jones, J., PA, S., and RB, T. (2004). A New Method for Diagnosing Radiative Forcing and Climate Sensitivity. *Geophysical Research Letters*, 31(3).

Griscom, B., Adams, J., and Ellis, P. (2017). Natural Climate Solutions. *PNAS Earth, Atmospheric, and Planetary Sciences*, 114(44):11645–11650.

Grise, K. M., Davis, S. M., Simpson, I. R., Waugh, D. W., Fu, Q., and Allen, R. J. (2019). Recent tropical expansion: Natural variability or forced response? *Journal of Climate*, 32:1551–1571.

Grose, M. R., Gregory, J., Colman, R., and Andrews, T. (2018). What climate sensitivity index is most useful for projections? *Geophysical Research Letters*, 45:1559–.

Guliasi, L. (2021). Toward a political economy of public safety power shutoff: Politics, ideology, and the limits of regulatory choice in California. *Energy Research & Social Science*, 71:101842.

Haile, G. G., Tang, Q., Hosseini-Moghari, S.-M., and Liu, X. (2020). Projected Impacts of Climate Change on Drought Patterns Over East Africa. *Earth's Future*, 8(7).

Hamlet, A. F., Lee, S.-Y., Mickelson, K. E. B., and Elsner, M. M. (2010). Effects of projected climate change on energy supply and demand in the Pacific Northwest and Washington State. *Climatic Change*, 102(1):103–128.

Hankel, C. and Tziperman, E. (2001). The Role of Atmospheric Feedbacks in Abrupt Winter Arctic Sea Ice Loss in Future Warming Scenarios. *Journal of Climate*, 34(11):4435–4447.

Harper, A. B., Powell, T., and Cox, P. M. (2018). Land-use emissions play a critical role in land-based mitigation for Paris climate targets. *Nature Communications*, 9:2938.

Hartmann, D. and Larson, K. (2002). An Important Constraint on Tropical Cloud - Climate Feedback. *Geophysical Research Letters*, 29(20):12–1–12–14.

Hasegawa, T., Fujimori, S., and Shin, Y. (2015). Consequences of Climate Mitigation on the Risk of Hunger. *Environ. Sci. Technol*, 49(12):7245–7253.

Hausfather, Z. and Peters, G. P. (2020). Emissions – the 'business as usual' story is misleading. *Nature*, 577:618–620.

Heck, V., Gerten, D., and Lucht, W. (2018). Biomass-based negative emissions difficult to reconcile with planetary boundaries. *Nature Climate Change*, 8:151–155.

Held, I. M. and Soden, B. J. (2006). Robust Responses of the Hydrological Cycle to Global Warming. *Journal of Climate*, 19(21):5686–99.

Hezel, J. P., Fichefet, I., and Massonnet, F. (2014). Modeled Arctic Sea Ice Evolution through 2300 in CMIP5 Extended RCPs. *Cryosphere*, 8(4):1195–1204.

Hickel, J. and Slamersak, A. (2022). Existing climate mitigation scenarios perpetuate colonial inequalities. *Lancet Planet Health*, 6:628–31.

Hoegh-Guldberg, O., Jacob, D., and Taylor, M. (2019). The human imperative of stabilizing global climate change at 1.5°C. *Science*, 365(6459).

Holland, M. and Bitz, C. (2003). Polar amplification of climate change in coupled models. *Climate Dynamics*, 21:221–232.

Howard, J. T., Androne, N., Alcover, K. C., and Santos-Lozada, A. R. (2024). Trends of Heat-Related Deaths in the US, 1999-2023. *JAMA*, 332(14):1203–1204.

Hu, S. and Vallis, G. (2019). Meridional structure and future changes of tropopause height and temperature. *Quarterly Journal of the Royal Meteorological Society*, 145(723):2698–717.

Hu, Y., Huang, H., and Zhou, C. (2018). Widening and Weakening of the Hadley Circulation under Global Warming. *Science Bulletin*, 63(10):640–44.

Hwang, Y. and Frierson, D. (2010). Increasing Atmospheric Poleward Energy Transport with Global Warming. *Geophysical Research Letters*, 37(24).

Hwang, Y., Frierson, D., and Kay, J. (2011). Coupling between Arctic feedbacks and changes in poleward energy transport. *Geophysical Research Letters*, 38:17704,.

Jackson, L., Kahana, R., Graham, T., Ringer, M., Woollings, T., and Meckinget, J. (2015). Global and European climate impacts of a slowdown of the AMOC in a high resolution GCM. *Climate Dynamics*, 45:3299–3316.

Jahn, A. and Holland, M. (2013). Implications of Arctic Sea Ice Changes for North Atlantic Deep Convection and the Meridional Overturning Circulation in CCSM4-CMIP5 Simulations. *Geophysical Research Letters*, 40(6):1206–11.

Jenkins, S., Cain, M., and Friedlingstein, P. (2021). Quantifying non-CO2 contributions to remaining carbon budgets. *npj Clim Atmos Sci*, 4(47).

Jenkins, S., Sanderson, B. M., Peters, G., Frolicherm, T. L., Friedlingstein, P., and Allen, M. (2022). The Multi-Decadal Response to Net Zero CO2 Emissions and Implications for Emissions Policy. *Geophysical Research Letters*, 49(23):e2022GL101047.

Jones, C. (2019). The zero emissions commitment model intercomparison project (ZECMIP) contribution to C4MIP: Quantifying committed climate changes following zero carbon emissions Geosci. *Geosci. Model Dev.*, 12:4375–85.

Kang, S., Seager, R., Frierson, D., and Revisited, L. X. (2015). Why is the northern hemisphere warmer than the southern hemisphere? *Climate Dynamics*, 44:1457–1472.

Karmalkar, A. V. and Bradley, R. S. (2017). Consequences of Global Warming of 1.5 °C and 2 °C for Regional Temperature and Precipitation Changes in the Contiguous United States. *PLOS One*.

Keyßer, L. T. and Lenzen, M. (2021). 1.5 °C degrowth scenarios suggest the need for new mitigation pathways. *Nature Communications*, 12(2676).

Kienbaum, K., Farrell, J., and Grimley, M. (2023). Advantage Local: Why Local Energy Ownership Matters. Technical report, Institution for Local Self-Reliance.

King, M. D. (2025). New Interactive Data Tool Shows Characteristics of Those Who Receive Assistance From Government Programs. *US Census Bureau*.

Kostov, Y., Johnson, H. L., and Marshall, D. P. (2019). AMOC sensitivity to surface buoyancy fluxes: The role of air-sea feedback mechanisms. *Climate Dynamics*, 53:4521–4537.

Koven, C. D., Sanderson, B. M., and Swann, A. L. S. (2023). Much of Zero Emissions Commitment Occurs Before Reaching Net Zero Emissions. *Environmental Research Letters*, 18(1).

Lamboll, R. D., Nicholls, Z. R. J., and Smith, C. J. (2023). Assessing the size and uncertainty of remaining carbon budgets. *Nature Climate Change*, 13:1360–1367.

Leach, N., Jenkins, S., and Nicholls, Z. (2020). FaIRv2.0.0: a generalized impulse response model for climate uncertainty and future scenario exploration. *Geosci. Model Dev*, 14.

Lee, J.-Y., Marotzke, J., Bala, G., and Cao, L. (2023). Future Global Climate: Scenario-based Projections and Near-term Information. In *Climate Change 2021: The Physical Science Basis. Contribution of Working Group 1 to the Sixth Assessment of the Intergovernmental Panel on Climate Change*. Cambridge University Press.

Leimbach, M., Kriegler, E., and Roming, N. (2017). Future growth patterns of world regions – A GDP scenario approach. *Global Environmental Change*, 42:215–225.

Li, H., Fedorov, A., and Liu, W. (2021). AMOC Stability and Diverging Response to Arctic Sea Ice Decline in Two Climate Models. *Journal of Climate*, 34(13):5443–5460.

Lin, Y., Hwang, Y., Ceppi, P., and Gregory, J. (2019). Uncertainty in the Evolution of Climate Feedback Traced to the Strength of the Atlantic Meridional Overturning Circulation. *Geophysical Research Letters*, 46:12331–12339.

Liu, P. R. and Raftery, A. E. (2021). Country-based rate of emissions reductions should increase by 80% beyond nationally determined contributions to meet the 2 °C target. *Communications Earth & Environment*, 2(1):29.

Low, S. and Schafer, S. (2020). Is bio-energy carbon capture and storage (BECCS) feasible? The contested authority of integrated assessment modeling. *Energy Research & Social Science*, 60(101326).

Lu, J., Vecchi, G., and Reichler, T. (2007). Expansion of the Hadley cell under global warming. *Geophysical Research Letters*, 34(6).

Lüthi, S., Fairless, C., Fischer, E. M., Scovronick, N., Ben Armstrong, Coelho, M. D. S. Z. S., Guo, Y. L., Guo, Y., Honda, Y., Huber, V., Kyselý, J., Lavigne, E., Royé, D., Ryti, N., Silva, S., Urban, A., Gasparrini, A., Bresch, D. N., and Vicedo-Cabrera, A. M. (2023). Rapid increase in the risk of heat-related mortality. *Nature Communications*, 14(1):4894.

Lynch, D. (1996). Cirrus clouds: Their role in climate and global change. *Acta Astronautica*, 38(11):859–863.

Lyon, C., Saupe, E., Smith, C., Hill, D., Beckerman, A., and LC, S. (2021). Climate change research and action must look beyond 2100. *Global Change Biology*, 28(2):1–13.

MacDougall, A. H., Frölicher, T. L., Jones, C. D., Rogelj, J., Matthews, H. D., Zickfeld, K., Arora, V. K., Barrett, N. J., Brovkin, V., Burger, F. A., Eby, M., Eliseev, A. V., Hajima, T., Holden, P. B., Jeltsch-Thömmes, A., Koven, C., Mengis, N., Menviel, L., Michou, M., Mokhov, I. I., Oka, A., Schwinger, J., Séférian, R., Shaffer, G., Sokolov, A., Tachiiri, K., Tjiputra, J., Wiltshire, A., and Ziehn, T. (2020). Is there warming in the pipeline? A multi-model analysis of the Zero Emissions Commitment from CO_2. *Biogeosciences (Online)*, 17(11):2987–3016.

Masson-Delmotte, V., Zhai, P., Pirani, A., Connors, S. L., Pean, C., Berger, S., Caud, N., and Chen, L. (2021). Climate Change 2021: The Physical Science Basis. Contribution of Working Group I to the Sixth Assessment Report of the Intergovernmental Panel on Climate Change. In *IPCC Summary for Policymakers*. Cmabride Univ. Press.

Matthews, H., Gillett, N., and Stott, P. (2009). The proportionality of global warming to cumulative carbon emissions. *Nature*, 459:829–832.

Meehl, G. A., Senior, C. A., Eyring, V., Flato, G., Lamarque, J. F., and Stouffer, R. J. (2020). Context for Interpreting Equilibrium Climate Sensitivity and Transient Climate Response from the CMIP6 Earth System Models. *Science Advances*, 6(26).

Meehl, G. A., Washington, W. M., Arblaster, J. M., Hu, A., Teng, H., and Tebaldi, C. (2012). Climate System Response to External Forcings and Climate Change Projections in CCSM4. *Journal of Climate*, 25(11):3661–83.

Meinshausen, M., Smith, S., Calvin, K., Daniel, J., Kainuma, M., and JF, L. (2011). The RCP greenhouse gas concentrations and their extensions from 1765 to 2300. *Climatic Change*, 109:213.

Mengis, N., Partanen, A., and Jalbert, J. (2018). 1.5 °C carbon budget dependent on carbon cycle uncertainty and future non-CO2 forcing. *Sci Rep*, 8:5831.

Meraner, K., Mauritsen, T., and Aiko, V. (2013). Robust increase in equilibrium climate sensitivity under global warming. *Geophysical Research Letters*, 40(22).

Milward-Hopkins, J., Steinburger, J., and Rao, N. (2020). Providing decent living with minimum energy: A global scenario. *Global Environmental Change*, 65(102168).

Minx, J. and al (2018). Negative emissions—Part 1: Research landscape and synthesis. *Environmental Research Letters*, 13(6).

Mitevski, I., Orbe, C., and Chemke, R. (2021). Non-Monotonic Response of the Climate System to Abrupt CO2 Forcing. *GRL*, 48(6).

Mitevski, I., Polvani, L., and Orbe, C. (2022). Asymmetric warming/cooling response to CO2 increase/decrease mainly due to non-logarithmic forcing, not feedbacks. *Geophysical Research Letters*, 49.

Narsey, S., Brown, JR, D., F, B., G, G., M, C., and al R, e. (2022). Storylines of South Pacific Convergence Zone Changes in a Warmer World. *Journal of Climate*, 35(20):2949–2967.

Neelin, J. and Held, I. (1987). Modeling Tropical Convergence Based on the Moist Static Energy Budget. *Monthly Weather Review*, 115:3–12.

Nordhaus, W. (1992). The 'DICE' Model: Background and Structure of a Dynamic Integrated Climate-Economy Model of the Economics of Global Warming. *The American Economic Review*.

O'Neill, B., Tebaldi, C., Vuuren, D., Eyring, V., Friedlingstein, P., and Hurtt, G. (2016). The Scenario Model Intercomparison Project (ScenarioMIP) for CMIP6. *Geoscientific Model Development*, 9(9):3461–82.

Ono, J., Watanabe, M., Komuro, Y., Tatebe, H., and Abe, M. (2022). Enhanced Arctic warming amplification revealed in a low-emission scenario. *Communications Earth & Environment*, 3:27.

Philip, S. Y., Kew, S. F., van Oldenborgh, G. J., Anslow, F. S., Seneviratne, S. I., Vautard, R., Coumou, D., Ebi, K. L., Arrighi, J., Singh, R., van Aalst, M., Pereira Marghidan, C., Wehner, M., Yang, W., Li, S., Schumacher, D. L., Hauser, M., Bonnet, R., Luu, L. N., Lehner, F., Gillett, N., Tradowsky, J. S., Vecchi, G. A., Rodell, C., Stull, R. B., Howard, R., and Otto, F. E. L. (2022). Rapid attribution analysis of the extraordinary heat wave on the Pacific coast of the US and Canada in June 2021. *Earth System Dynamics*, 13(4):1689–1713.

Pierrehumbert, R. (2002). The hydrologic cycle in deep time climate problems. *Nature*, 419:191–198.

Pithan, F. and Mauritsen, T. (2014). Arctic amplification dominated by temperature feedbacks in contemporary climate models. *Nature Geoscience*, 7:181–184.

PNUCC (2024). Northwest Regional Forecast of Power Loads and Resources, August 2024 through July 2034. Technical report, Pacific Northwest Utilities Conference Committee.

Poletti, A., Frierson, D., Aerenson, T., Nikumbh, A., Carroll, R., Henshaw, W., and Scheff, J. (2024a). Atmosphere and Ocean Energy Transport in Extreme Warming Scenarios. *PLOS Climate*.

Poletti, A., Frierson, D., and Armour, K. (2024b). Why do CO2 Quadrupling Simulations Warm More than Twice as Much as CO2 Doubling Simulations in CMIP6? *GRL*, 51(10).

Powers, M. (2025). DOGE cuts and Trump's plans leave a heating assistance program in limbo. *The Washington Post*.

Putrasahan, D., Lohmann, K., Storch, J., Jungclaus, J., Gutjahr, O., and Haak, H. (2019). Surface flux drivers for the slowdown of the Atlantic meridional overturning circulation in

a high-resolution global coupled climate model. *Journal of Advances in Modeling Earth Systems*, 11(5):1349–63.

Rao, N. and Min, J. (2018). Decent Living Standards: Material Prerequisites for Human Wellbeing. *Soc Indic Res*, 138:225–244.

Rao, N., Sauer, P., and Gidden, M. (2019). Income inequality projections for the Shared Socioeconomic Pathways (SSPs. *Futures*, 105:27–39.

RCW (2019). Revised code of washington 19.405 washington Clean Energy Transformation Act.

Roe, G., Feldl, N., Armour, K., Hwang, Y., and Frierson, D. (2015). The Remote Impacts of Climate Feedbacks on Regional Climate Predictability. *Nature Geoscience*, 8(2):135–39.

Rogelj, J. and Lamboll, R. (2024). Substantial reductions in non-CO2 greenhouse gas emissions reductions implied by IPCC estimates of the remaining carbon budget. *Commun Earth Environ*, 5:35.

Rogelj, J., Shindell, D., and Jiang, K. (2018). Mitigation Pathways Compatible with 1.5°C in the Context of Sustainable Development. In *Global Warming of 1.5°C. An IPCC Special Report on the Impacts of Global Warming of 1.5°C above Pre-Industrial Levels and Related Global Greenhouse Gas Emission Pathways, in the Context of Strengthening the Global Response to the Threat of Climate Change, Sustainable Development, and Efforts to Eradicate Poverty*. Cambridge University Press, Cambridge.

Rugenstein, M., Bloch-Johnson, J., Abe-Ouchi, A., Andrews, T., Beyerle, U., and Li, C. (2019a). LongRunMIP: Motivation and Design for a Large Collection of Millennial-Length AOGCM Simulations. *Bulletin of the American Meteorological Society*, 100:2551–2570.

Rugenstein, M., Bloch-Johnson, J., Gregory, J., Andrews, T., Mauritsen, T., and Li, C. (2019b). Equilibrium Climate Sensitivity Estimated by Equilibrating Climate Models. *Geophysical Research Letters*, 47(4).

Sadai, S., Spector, R., DeConto, R., and Gomez, N. (2022). The Paris Agreement and climate justice: Inequitable impacts of sea level rise associated with temperature targets. *Earth's Future*, 10(e2022EF002940).

Sanderson, B. M., Brovkin, V., Fisher, R., Hohn, D., Ilyina, T., Jones, C., Koenigk, T., Koven, C., Li, H., Lawrence, D., Lawrence, P., Liddicoat, S., Macdougall, A., Mengis, N., Nicholls, Z., O'Rourke, E., Romanou, A., Sandstad, M., Schwinger, J., Seferian, R., Sentman, L., Simpson, I., Smith, C., Steinert, N., Swann, A., Tjiputra, J., and Ziehn, T. (2024). flat10MIP: An emissions-driven experiment to diagnose the climate response to positive, zero, and negative CO2 emissions. *EGUsphere*, pages 1–39.

Schwinger, J., Asaadi, A., Goris, N., and Lee, H. (2022). Possibility for strong northern hemisphere high-latitude cooling under negative emissions. *Nature Communications*, 13(1):1095.

Séférian, R., Bossy, T., Gasser, T., Nichols, Z., Dorheim, K., Su, X., Tsutsui, J., and Santana-Falcón, Y. (2024). Physical inconsistencies in the representation of the ocean heat-carbon nexus in simple climate models. *Communications Earth & Environment*, 5(1):291.

Seidel, D., Fu, Q., Randel, W., and Reichler, T. (2008). Widening of the tropical belt in a changing climate. *Nature geoscience*, 1(1):21–4.

Serreze, M., Barrett, A., Stroeve, J., Kindig, D., and Holland, M. (2009). The Emergence of Surface-Based Arctic Amplification. *The Cryosphere*, 3:11–19.

Sherwood, S. and Fu, Q. (2014). A Drier Future? *Science Climate Change*, 343(6172):737–739.

Sherwood, S., Webb, M., Annan, J., Armour, K., Forster, P., and Hargreaves, J. (2020). An Assessment of Earth's Climate Sensitivity Using Multiple Lines of Evidence. *Reviews of Geophysics*, page 58.

Shum, G. E. M. (2024). *Biogeophysical and Biogeochemical Processes at the Surface Determine Habitability in Two Extreme Climates*. PhD thesis, University of Washington.

Siler, N., Roe, G., and Armour, K. (2018). Insights into the Zonal-Mean Response of the Hydrologic Cycle to Global Warming from a Diffusive Energy Balance Model. *Journal of Climate*, 31(18):7481–93.

Smith, P., Davis, S., and Creutzig, F. (2016). Biophysical and economic limits to negative CO2 emissions. *Nature Clim Change*, 6:42–50.

Sonja, K. and Harald, W. (2018). Building Equity In: Strategies for Integrating Equity into Modelling for a 1.5oC World. *Philos Trans A Math Phys Eng Sci*.

Staten, P. and Reichler, T. (2014). On the Ratio between Shifts in the Eddy-Driven Jet and the Hadley Cell Edge. *Climate Dynamics*, 42(5–6):1229–42.

Steinberger, J. K. and Roberts, J. T. (2010). From constraint to sufficiency: The decoupling of energy and carbon from human needs, 1975–2005. *Ecological Economics*, 70(2):425–433.

Swart, N., Cole, J., Kharin, VV, L., M, S., JF, G., and N.P. (2019). The Canadian Earth System Model version 5 (CanESM5.0.3. *Geoscientific Model Development*, 12(11):4823–4873.

Tarshish, N., Jeevanjee, N., and Fung, I. (2023). Emissions cessation yields multi-century cooling.

Taylor, K., Crucifix, M., Braconnot, P., Hewitt, C., Doutriaux, C., and Broccoli, A. (2007). Estimating Shortwave Radiative Forcing and Response in Climate Models. *Journal of Climate*, 20(11):2530–43.

Tebaldi, C., Debeire, K., Eyring, V., Fischer, E., Fyfe, J., and Friedlingstein, P. (2020). Climate model projections from the Scenario Model Intercomparison Project (ScenarioMIP) of CMIP6. *Earth System Dynamics Discuss*.

Thompson, C. and Kimball, M. (2022). Summary of the Effects of COVID-19 on Washington's Investor-Owned Utility Residential Customers (Docket U-200281). Technical report, The Energy Project.

Thompson, V., Kennedy-Asser, A. T., Vosper, E., Lo, Y. T. E., Huntingford, C., Andrews, O., Collins, M., Hegerl, G. C., and Mitchell, D. (2022). The 2021 western North America heat wave among the most extreme events ever recorded globally. *Science Advances*, 8(18):eabm6860.

Thuraisingham, M. (2021). An Equitable Transition to 100% Clean Energy in Washington.

Tokarska, K. B., Zickfeld, K., and Rogelj, J. (2019). Path Independence of Carbon Budgets When Meeting a Stringent Global Mean Temperature Target After an Overshoot. *Earth's Future*, 7(12):1283–1295.

Tong, K., Ramaswami, A., Xu, C. K., Feiock, R., Schmitz, P., and Ohlsen, M. (2021). Measuring social equity in urban energy use and interventions using fine-scale data. *Proceedings of the National Academy of Sciences*, 118(24):e2023554118.

Tripathy, K., Mukherjee, S., Mishra, A., and Williams, A. (2023). Climate Change Will Accelerate the High-end Risk of Compound Drought and Heatwave Events. *PNAS*, 120(28).

Tripati, A., Roberts, C., and Eagle, R. (2009). Coupling of CO2 and Ice Sheet Stability Over Major Climate Transitions of the Last 20 Million Years. *Science*, 326(5958):1394–1397.

Turner, P., Field, C., and Lobell, D. (2018). Unprecedented rates of land-use transformation in modelled climate change mitigation pathways. *Nat Sustain*, 1:240–245.

UNFCCC (2015). Paris Agreement to the United Nations Framework Convention on Climate Change.

UWEOHS (2022). Washington Environmental Health Disparities Map: Cumulative Impacts of Environmental Health Risk Factors Across Communities of Washington State: Technical Report Version 2.0. Technical report, University of Washington (UW) Department of Environmental & Occupational Health Sciences and Washington State Department of Health.

Vecchi, G. A. and Soden, B. J. (2007). Global warming and the weakening of the tropical circulation. *Journal of Climate*, 20:4316–4340.

Virgin, J., Fletcher, C., Cole, J., Salzen, K., and Mitovski, T. (2021). Cloud Feedbacks from CanESM2 to CanESM5.0 and their influence on climate sensitivity. *Geoscientific Model Development*, 14(9).

Vogel, J., Steinburger, J., and al (2021). Socio-economic conditions for satisfying human needs at low energy use: An international analysis of social provisioning. *Global Environmental Change*.

Vuuren, D. P., Edmonds, J., Kainuma, M., Riahi, K., Thomson, A., and Hibbard, K. (2011). The representative concentration pathways: An overview. *Climatic Change*, 109:5.

Washington, W. M. and Meehl, G. A. (1996). High-Latitude Climate Change in a Global Coupled Ocean atmosphere-Sea Ice Model with Increased Atmospheric CO2. *Journal of Geophysical Research Atmospheres*, 101(D8):12795–801.

Watt-Meyer, O., Frierson, D. M. W., and Fu, Q. (2019). Hemispheric Asymmetry of Tropical Expansion Under CO2 Forcing. *Geophysical Research Letters*, 46(15):9231–9240.

Weaver, A. J., Sedláček, J., Eby, M., Alexander, K., Crespin, E., Fichefet, T., and al (2012). Stability of the Atlantic meridional overturning circulation: A model intercomparison. *Geophysical Research Letters*, 39:20709.

Weijer, W., Maltrud, M. E., Hecht, M. W., Dijkstra, H. A., and Kliphuis, M. A. (2012). Response of the Atlantic Ocean circulation to Greenland ice sheet melting in a strongly eddying ocean model.Geophysical Research Letters. *Geophysical Research Letters*, 39(9).

Weikmans, R., van Asselt, H., and Roberts, J. T. (2021). Transparency requirements under the Paris Agreement and their (un)likely impact on strengthening the ambition of Nationally Determined Contributions (NDCs). In *Making Climate Action More Effective*. Routledge.

Weinberger, H. (2022). New WA program gives low-income renters access to A/C. *Cascade PBS*.

Wetherald, R. T. and Manabe, S. (1988). Cloud Feedback Processes in a General Circulation Model. *Journal of the Atmospheric Sciences*, 45(8):1397–1415.

White, R. H., Anderson, S., Booth, J. F., Braich, G., Draeger, C., Fei, C., Harley, C. D. G., Henderson, S. B., Jakob, M., Lau, C.-A., Mareshet Admasu, L., Narinesingh, V., Rodell, C., Roocroft, E., Weinberger, K. R., and West, G. (2023). The unprecedented Pacific Northwest heatwave of June 2021. *Nature Communications*, 14(1):727.

Wiedmann, T., Lenzen, M., Keyßer, L. T., and Steinberger, J. K. (2020). Scientists' warning on affluence. *Nature Communications*, 11(1):3107.

Williams, G. R., Ceppi, P., and Katavouta, A. (2020). Controls of the Transient Climate Response to Emissions by Physical Feedbacks, Heat Uptake, and Carbon Cycling. *Environmental Research Letters*, 15(9).

Winkler, A. J., Myneni, R., and Reimers, C. (2024). Carbon System State Determines Warming Potential of Emissions. *PLOS One*.

Yang, W., Seager, R., Cane, M. A., and Lyon, B. (2014). The east African long rains in observations and models. *Journal of Climate*, 27:7185–7202.

Yu, S. and Pritchard, M. S. (2019). A Strong Role for the AMOC in Partitioning Global Energy Transport and Shifting ITCZ Position in Response to Latitudinally Discrete Solar Forcing in CESM1.2. *Journal of Climate*, 32(8):2207–2226.

Yukimoto, S., Kawai, H., Koshiro, T., Oshima, N., Yoshida, K., and Urakawa, S. (2019). The meteorological research institute Earth system model version 2.0, MRI-ESM2.0: Description and basic evaluation of the physical component. *Journal of the Meteorological Society of Japan*, 97(5):931–965.

Yuval, J. and Kaspi, Y. (2020). Eddy Activity Response to Global Warming–Like Temperature Changes. *Journal of Climate*, 33:1381–1404.

Zelinka, M. D., Andrews, T., Forster, P. M., and Taylor, K. E. (2014). Quantifying Components of Aerosol-Cloud-Radiation Interactions in Climate Models. *Journal of Geophysical Research: Atmospheres*, 119(12):7599–7615.

Zelinka, M. D. and Hartmann, D. L. (2010). Why Is Longwave Cloud Feedback Positive? *Journal of Geophysical Research Atmospheres*, 115(16).

Zelinka, M. D., Myers, T. A., McCoy, D. T., Po-Chedley, S., Caldwell, P. M., Ceppi, P., Zhang, R., and Delworth, T. L. (2020). Causes of Higher Climate Sensitivity in CMIP6 Models. *Geophysical Research Letters*, 47(1):1853–1860.

Zhang, R. and Delworth, T. L. (2005). Simulated Tropical Response to a Substantial Weakening of the Atlantic Thermohaline Circulation. *Journal of Climate*, 18(12):1853–1860.

Zhang, R., Kang, S. M., and Held, I. M. (2010). Sensitivity of Climate Change Induced by the Weakening of the Atlantic Meridional Overturning Circulation to Cloud Feedback. *Journal of Climate*, 23(2):378–389.

Zhou, W., Xie, S. P., and Yang, D. (2019). Enhanced equatorial warming causes deep-tropical contraction and subtropical monsoon shift. *Nature Climate Change*, 9:834–839.

Zickfeld, K., Arora, V. K., and Gillett, N. P. (2012). Is the climate response to CO2 emissions path dependent? *Geophysical Research Letters*, 39, L05703.

Zickfeld, K., Azevedo, D., Mathesius, S., and Matthews, H. D. (2021). Asymmetry in the climate–carbon cycle response to positive and negative CO2 emissions. *Nature Climate Change*, 11(7):613–617.

Zickfeld, K., Eby, M., Weaver, A., Alexander, K., Crespin, E., and Edwards, N. R. (2013). Long-Term Climate Change Commitment and Reversibility: An EMIC Intercomparison. *Journal of Climate*, 26(16):5782–5809.

Zickfeld, K., MacIsaac, A. J., Canadell, J. G., Fuss, S., Jackson, R. B., Jones, C. D., Lohila, A., Matthews, H. D., Peters, G. P., Rogelj, J., and Zaehle, S. (2023). Net-zero approaches

must consider Earth system impacts to achieve climate goals. *Nature Climate Change*, 13(12):1298–1305.

Zurita-Gotor, P. (2006). Updraft/Downdraft Constraints for Moist Baroclinic Modes and Their Implications for the Short-Wave Cutoff and Maximum Growth Rate. *Journal of the Atmospheric Sciences*, 62(12):4450–4458.